FLUX-WEAKENING CONTROL FOR INTERIOR PERMANENT MAGNET MOTORS

ADVANCED FLUX-WEAKENING CONTROL METHODS FOR INTERIOR PERMANENT MAGNET SYNCHRONOUS MOTORS WITH TORQUE PERFORMANCE IMPROVEMENT

BY

YIHUI LI, B.Eng.

A THESIS

SUBMITTED TO THE DEPARTMENT OF ELECTRICAL & COMPUTER ENGINEERING

AND THE SCHOOL OF GRADUATE STUDIES

OF MCMASTER UNIVERSITY

IN PARTIAL FULFILMENT OF THE REQUIREMENTS

FOR THE DEGREE OF

MASTER OF APPLIED SCIENCE

Master of Applied Science (2020) McMaster University

(Electrical & Computer Engineering) Hamilton, Ontario, Canada

TITLE: Advanced Flux-Weakening Control Methods for Interior Permanent Magnet Synchronous Motors with Torque Performance Improvement

AUTHOR: Yihui Li

B.Eng. (Electrical Engineering)

Northwestern Polytechnical University, Xi'an, China

SUPERVISOR: Dr. Ali Emadi

NUMBER OF PAGES: xviii, 122

To my parents

Abstract

The flux-weakening control (FWC) methods for interior permanent magnet synchronous motors (IPMSMs) with torque performance improvement are studied in this thesis.

A FWC strategy with constant parameters is proposed, which achieves the extended dc-link voltage utilization and improves the tracking performance. The voltage trajectory is extended to the overmodulation region to increase the dc-link voltage utilization rate and torque. Moreover, a current predictive controller is implemented to improve tracking performance.

A FWC method considering the resistive voltage drop and magnetic saturation is proposed. The proposed method achieves the voltage extension, torque improvement, and improved dynamic performance by establishing a new stator flux linkage adjustment method. The stator flux linkage reference is adjusted based on the torque reference, operating speed, and modulation index. Two voltage feedback paths are established and chosen based on the torque reference and operating speed. The stator resistance and nonlinear inductance characteristics are constructed based on the experimental test. Thus, accurate current control is achieved. Compared to feedforward-based FWC methods, the

proposed method improves the output torque and power. Compared to feedback-based FWC methods, the proposed method improves the dynamic performance and avoids the voltage saturation and windup problem. Compared to the mixed FWC methods, which only have one feedback path, the proposed method improves the dynamic performance.

The influence of extended dc-link voltage utilization is analyzed. The nonlinear relationship between voltage and torque is solved mathematically. The torque, torque ripple, and current ripple trends with modulation index in voltage extension region are analyzed, and the harmonic spectra of voltage, current, and torque with or without voltage extension are compared, which provide the guidance to make the tradeoff between maximizing the torque and torque ripple alleviation.

Acknowledgments

At first, I would like to thank my supervisor Dr. Ali Emadi for giving me the chance to work at McMaster Automotive Resource Centre (MARC). I have met with and learned from so many researchers from all over the world at MARC. I have the chance to speak to and work with industry partners. All these opportunities are given by my supervisor Dr. Emadi. I would like to thank Dr. Emadi for his guidance, discussions, and suggestions on my research. Dr. Emadi's hard-working, enthusiasm and creativity in the research areas have inspired me and will guide me for my future work and my life.

I also would like to thank Dr. Berker Bilgin. He is always patient and willing to teach and lead us on industry projects. He always has great ideas on how the projects will go on. The projects are well-organized, and we are working efficiently thanks to Dr. Bilgin. We know what we need to do clearly when we are working under his guidance. His concentration, patience and passion when working will be helpful for my future work.

In addition, I would like to thank Dr. Mehdi Narimani, Dr. Jennifer Bauman, Dr. Ryan Ahmed, and Dr. Mohamed Bakr, for giving us technical lessons. We have learned lots of knowledge and techniques from courses.

Besides, I would like to thank my colleagues at MARC. I would like to thank Dr. Jianbin Liang, Dr. Brock Howey, Dr. Yawei Wang, Dr. Ehab Sayed, Dr. Jianing Lin, Mehdi Eshaghian, Chris Mak, and Diego Valencia Garcia, for helping and sharing experiences with me. I also would like to thank Dr. Ahmed Abdelrahman, Sujana Darasa, Nathan Emery for working together. Special thanks to Paul Nguyen, Dan Manolescu, Teresa Janes, Theresa Mitchell, and Cheryl Gies for their help on study and research.

I would like to thank my friends. Thank you, Zekun Xia, Jing Zhao, Deqiang Wang, Dianxun Xiao, Gaoliang Fang, Fei Gao, Guanghan Zhao, Alice Dong, and Yuhang Yang for the great time I spent with you.

I would like to thank my parents for all your love and support.

Contents

List of Figures

List of Tables

Chapter 1
Introduction

1.1 Background and Motivation

The popularity of electric vehicles (EVs) and hybrid electric vehicles (HEVs) has been increasing due to the incremental cost of fossil fuels and concerns about the environment [1]-[4]. Interior permanent magnet synchronous motors (IPMSMs) are widely used in EVs and HEVs, which is owing to their superior features such as high power density, wide speed range, and high efficiency [5]-[8]. In EVs and HEVs, the wide speed range is required, the operating regions of IPMSMs are extended to flux-weakening (FW) region.

IPMSM optimal operating regions can be classified as MTPA (maximum torque per ampere) region and flux-weakening region. With the increase of speed, the back electromotive force (EMF) is increasing. When the back EMF is higher than the maximum phase voltage, the current regulation loops are saturated, and the *dq*-axis current cannot track the current references. The back EMF should be reduced by weakening the flux when the current regulation loops are saturated. The

way is to reduce the *d*-axis current to weaken the air gap flux to keep the operating point on the voltage limit because the torque is mainly proportional to the *q*-axis current. This is called the flux-weakening control. If the *d*-axis current is not reduced, the *q*-axis will be reduced due to the dc-link voltage limit. The *q*-axis current and torque will fluctuate, which will cause deterioration of the performance of IPMSM drive systems. The flux-weakening region is on the left of MTPA and inside the current constraint. To be more specific, when the speed of the operating point is larger than the speed of the intersection point of torque with MTPA, the operating point is in the flux-weakening region. The flux-weakening region is shown as the green region in Fig. 1.2. An IPMSM drive system can be classified as a finite-speed drive system and an infinite-speed drive system. As shown in Fig. 1.2, for a finite-speed drive system, the center of voltage constraints is outside of the current constraint; for an infinite-speed drive system, the center of voltage constraints is inside of the current constraint. Maximum torque per voltage (MTPV) only exists in an infinite-speed drive system.

In the MTPA region, MTPA control is implemented. MTPA control can be classified as model-based, signal injection-based, and searching based.

In the FW region, there are more technical problems, such as the windup problem and slower dynamic response. These problems are caused by voltage saturation. Flux-weakening control techniques have been proposed to solve these problems, which can be classified as feedback (FB)-based, feedforward (FF)-based,

and mixed approaches. However, the existing feedback-based, feedforward-based, and mixed approaches have their limitations.

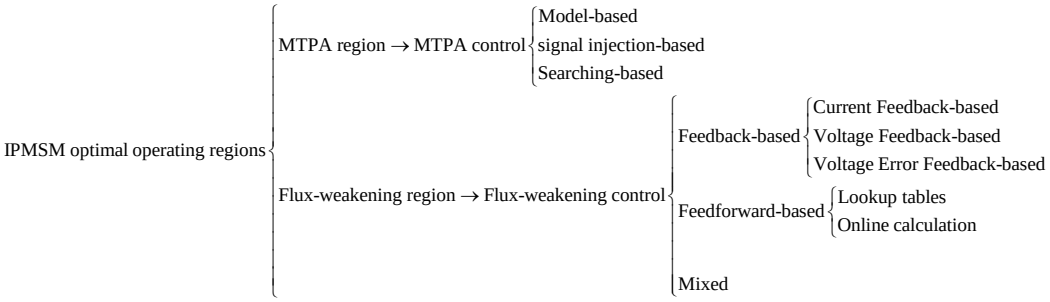

Fig. 1.1 Diagram of IPMSM operating regions

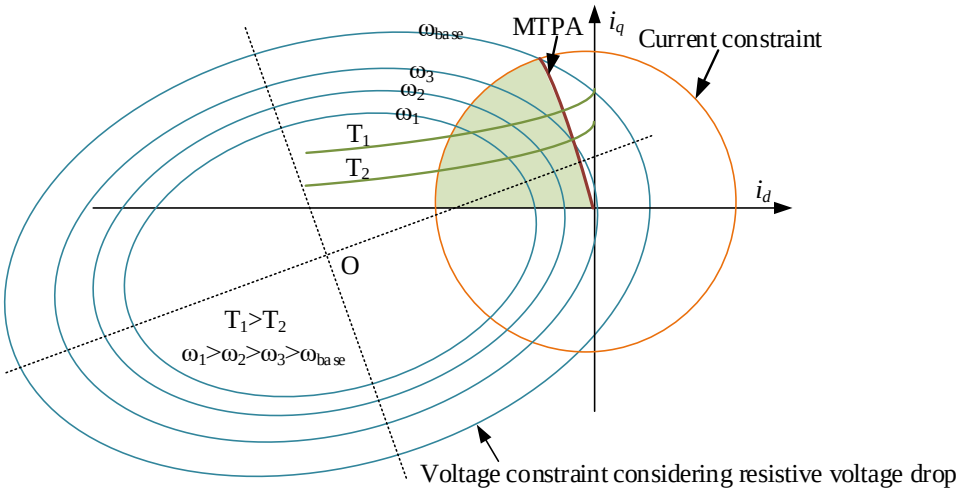

(a)

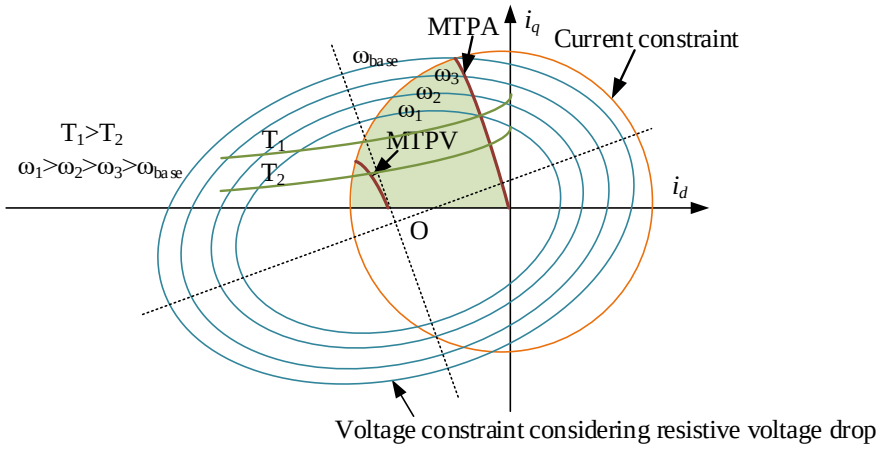

(b)

Fig. 1.2 IPMSM operating regions. (a) Finite-speed drive system. (b) Infinite-speed drive system.

The feedback-based flux-weakening control methods are motor parameters independent and thus insensitive to the variations of motor parameters. However, the feedback-based flux-weakening control methods cannot provide the optimal current references to achieve higher efficiency, and the transient performance is limited. Also, the inconsistency between FB-based FW control and anti-windup control puts the IPMSM control systems into a double squeeze.

The feedforward-based flux-weakening control methods find the optimal operating points based on motor parameters [11]-[13]. However, the FF-based FWC is sensitive to motor parameters variation. The control performance would degrade due to parameters variation. In [11]-[13], the maximum voltage is immutable and limited to the linear region of the space vector modulation (SVM). In [12], the optimal current references are calculated online, which requires less memory usage. However, the online calculation process is often time-consuming.

In [13], the optimal current reference lookup tables (LUTs) are obtained by finite element analysis (FEA). However, the detailed dimension of the machine is required.

Mixed flux-weakening techniques combine the feedback-based method with the feedforward-based method [14]-[17], which has the advantage of motor parameters insensitivity and fast dynamic performance. In the mixed flux-weakening methods, the current references are derived from the torque commands and stator flux linkage references. In [14], the modulation index (MI) reference is set to the constant value, which is not flexible enough and limits the dc-link voltage utilization. In [15], a mixed FW control for ramp torque command is proposed. The current references are on the current constraint when the torque command increases, which increases the core loss and reduces motor efficiency. In [16] and [17], the dc-link voltage is not included in the feedback loop, in which the dc-link voltage fluctuation is not considered.

The voltage overmodulation techniques are implemented in FW control methods to extend the voltage utilization. In [18], the overmodulation is divided into two modes: mode I (0.906 <modulation index (MI)< 0.952) and mode II (0.952 <MI< 1). In [14], only the overmodulation mode I is reached, which limits the voltage utilization rate.

The resistive voltage drop is often neglected in FW control methods to simplify the calculation process. However, the accuracy of optimal operating points calculation and FW control is degraded.

Table 1.1 Comparison of flux-weakening control methods

FWC methods	Robustness	Stability of regulation loops
FB-Based FWC	✓	
FF-Based FWC		✓
Mixed FWC	✓	✓

1.2 Contributions

The contributions have been made to the stable and accurate flux-weakening control for IPMSMs with improved torque performance, which are summarized as follows:

1) A mixed flux-weakening control method with constant parameters is proposed, which increases the dc-link voltage utilization rate, and improves the torque tracking performance. The proposed method has the fast dynamic performance provided by the feedforward path and the ability to compensate for the parameters mismatch owing to the closed-loop feedback path.
2) The influence of the resistive voltage drop and magnetic saturation is theoretically analyzed. Because of the highly nonlinear relationship among voltage, speed, and torque, the resistive voltage drop is ignored in most mixed flux-weakening control methods to simplify the calculation of operating points and the feedback path. However, the accuracy of flux-weakening control is degraded if the resistive voltage drop is ignored, which would cause the parameter mismatch and the error on tracking currents,

especially at high speed. The resistive voltage drop and magnetic saturation cause the shifting of voltage ellipses and torque loci. The operating points with and without considering the resistive voltage drop and magnetic saturation are compared in this thesis.

3) A mixed flux-weakening control method considering the resistive voltage drop and magnetic saturation is proposed, which increases the accuracy of flux-weakening control. To improve the dynamic performance, there are two feedback paths in the proposed flux-weakening control method. Compared to FF-based flux-weakening control methods, the proposed method improves the torque and power. Compared to FB-based flux-weakening control methods, the proposed method improves the dynamic performance, and avoids the voltage saturation and windup problem, and improves the stability of the IPMSM drive system. Compared to the mixed flux-weakening control methods which only have one feedback path, the proposed method improves the dynamic performance. Compared to the flux-weakening methods which do not consider the resistive voltage drop, the proposed method avoids the error on the tracking currents caused by parameter mismatch.
4) The highly nonlinear relationship between voltage and torque considering the resistive voltage drop is solved mathematically. The torque, torque ripple, and current ripple trends with modulation index in voltage extension region are analyzed. The harmonic spectra of voltage, current, and torque

with or without voltage extension are compared. The analysis of the relationship among voltage, torque, and torque ripple can help to make the tradeoff between maximizing the torque and torque ripple alleviation.

1.3 Thesis Outline

This thesis is organized as follows:

In Chapter 2, the IPMSM model, operating regions, and existing flux-weakening (FW) methods are introduced. The feedback-based FW methods, feedforward-based FW methods, and mixed FW methods are introduced.

In Chapter 3, a flux-weakening control strategy with constant parameters is proposed, which increases the dc-link voltage utilization rate, and improves the tracking performance. The voltage extension is realized by implementing an overmodulation algorithm. The tracking performance is improved by implementing a current predictive controller. The torque-stator flux linkage-current LUTs are obtained as the optimal current references. The stator flux linkage reference is adjusted based on the torque reference, speed, and MI in the proposed flux regulator.

In Chapter 4, the flux-weakening control method considering the resistive voltage drop and magnetic saturation is proposed. A new stator flux linkage adjustment (SFLA) method is proposed in the proposed flux-weakening control method. To improve the dynamic performance, there are two feedback paths in the proposed FWC method. The feedback path is chosen based on the torque reference and operating speed. The influence of the resistive voltage drop and magnetic

saturation are theoretically analyzed and considered in the optimal current reference LUTs and SFLA algorithm to improve the accuracy of FW control.

In Chapter 5, the windup phenomenon of the current regulation loop in the voltage extension region is analyzed. The mathematical relationship between voltage and torque is solved. The torque, torque ripple, and current harmonics trends in voltage extension region are analyzed.

The conclusions are presented, and the possible future works are listed in Chapter 6.

Chapter 2
IPMSM Model, Optimal Operating Regions, and Existing Flux-Weakening Control Techniques

2.1 Introduction

In this chapter, the IPMSM model, operating regions which include maximum torque per ampere (MTPA) and flux-weakening (FW) region, and existing flux-weakening methods are introduced. The existing flux-weakening methods include feedback-based FW methods, feedforward-based FW methods, and mixed FW methods. Mixed FW methods mix the feedforward-based FW control with the feedback-based FW control.

2.2 IPMSM Model

The dynamic model is represented in the *dq* reference frame. In the rotating reference frame, the voltage equations for IPMSMs are written as

$$L_d \frac{di_d}{dt} = \omega_e L_q i_q - R_s i_d + u_d \tag{2.1}$$

$$L_q \frac{di_q}{dt} = -\omega_e (L_d i_d + \lambda_m) - R_s i_q + u_q \tag{2.2}$$

where L_d and L_q are *d*- and *q*-axis inductances, λ_m is the permanent magnet flux linkage, u_d and u_q are *d*- and *q*-axis voltages, and ω_e is the electrical angular frequency. The electromagnetic torque, T_e is expressed as

$$T_e = \frac{3}{2} n_p \left[\lambda_m i_q + \left(L_d - L_q \right) i_d i_q \right] \tag{2.3}$$

where n_p is the number of pole pairs.

In order to analyze the dynamic behavior of an IPM machine, it is desirable to simulate the motor performance with the PWM VSI [20]. The PWM effects on loss in electric machines have been analyzed in [21] and [22]. The high-frequency current ripple generated by the PWM causes losses, which degrade the efficiency of the IPM machine [21]. The PWM VSI increases the complexity of the flux linkage pattern by inducing harmonics in the current and flux density waveforms, which cause additional losses and thermal problems [22]. Besides, the electric machines fed by PWM VSI could also exhibit higher acoustic noise level due to the high-frequency current ripple [23], [24].

The nonlinear electromagnetic characteristics of IPMSMs can be obtained by experiment test or finite element analysis (FEA). Efforts have been made to couple electromagnetic FEA with electric circuits [25]-[27]. However, if the PWM effects are considered and the VSI is modeled in FEA, the time step has to be set to

a much smaller value to take the high switching frequency into account. This results in higher computation cost and longer simulation time [28]. In order to avoid FEA computation in the dynamic simulation, lookup tables (LUTs) are used to establish the nonlinear electromagnetic characteristics of electric machines [29]-[31]. The flux linkage, torque, and voltage LUTs can be obtained from FEA or experiments. The detailed dimensions of motors are needed when using FEA for characterization. Ideal current waveforms would be required to obtain the LUTs, which would be much faster than modeling the VSI directly in FEA. In [29], a model based on the current LUTs as a function of the flux linkage and rotor position was presented considering the iron loss effect. The model did not include the PWM VSI; therefore, the harmonic content induced by high-frequency current ripple was ignored. These harmonics cause additional iron losses, which should not be neglected. In [30], a model considering the temperature effects was presented. However, the derivative calculation of flux linkage was used, which would accumulate errors and could cause instability, especially with a small time step when considering the drive system. In [31], another model was presented, which required the *d*- and *q*-axis self- and mutual-inductances, and the flux produced by permanent magnets. The authors have used simplifications for the calculation of *d*- and *q*-axis flux produced by the permanent magnets, which would reduce the accuracy of the model.

To ensure the accuracy of FW control, the accurate electromagnetic characteristics of IPMSMs are required. The inductances vary nonlinearly due to the magnetic saturation, which are functions of currents. The process to obtain the

nonlinear inductance LUTs based on the experimental test is as follows: The dyno motor drives the IPMSM at a speed which is close to and a bit lower than the base speed. The *d*-axis and *q*-axis currents are controlled and recorded. The *d*-axis and *q*-axis voltages are also recorded. The inductances for different current references are calculated by voltage equations.

The flux linkages in the *dq* reference system are expressed as

$$\begin{bmatrix} \lambda_d \\ \lambda_q \end{bmatrix} = L_{dq} \begin{bmatrix} i_d \\ i_q \end{bmatrix} + \begin{bmatrix} \lambda_m \\ 0 \end{bmatrix} \tag{2.4}$$

A mathematical model based on the derivative of the flux linkages could accumulate errors and cause instability. Therefore, an integral form is used to model the electrical dynamics of the motor. *d*-axis and *q*-axis flux linkages are reorganized as

$$\lambda_d = \int \left(u_d - R_s i_d + \omega_e \lambda_q \right) dt \tag{2.5}$$

$$\lambda_q = \int \left(u_q - R_s i_q - \omega_e \lambda_d \right) dt . \tag{2.6}$$

As shown in Fig. 2.1, the IPM machine is fed by a three-phase VSI, which consists of six switches and six diodes. The number of the combinations of switching states is eight, from [0 0 0] to [1 1 1]. The space vector diagram for the three-phase VSI is shown in Fig. 2.2. The space vector diagram is divided into six sectors formed by six active vectors V_i, i = 1, 2, …, 6, and the zero vector V_0 is at the center.

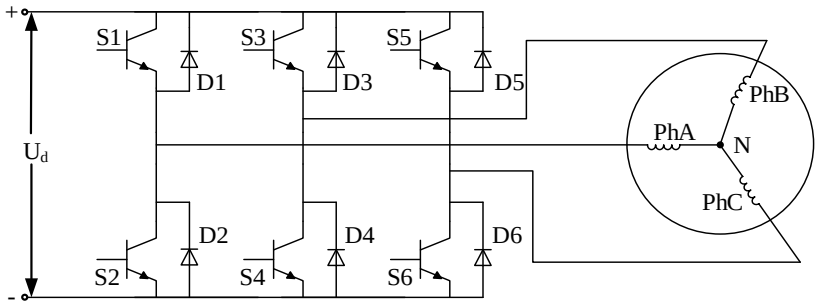

Fig. 2.1 IPM machine drive.

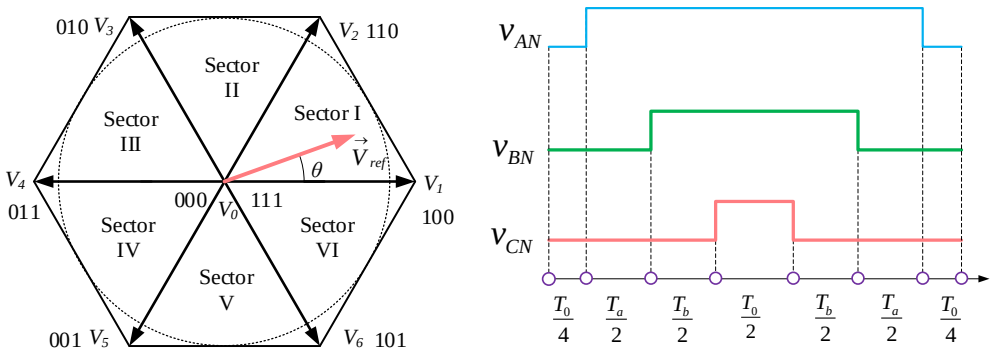

(a) (b)

Fig. 2.2 Space vector diagram. (a) eight voltage states; (b) three-phase voltage waveforms in sector III for one PWM switching cycle.

As shown in Fig. 2.2(a), θ is the angle between V_{ref} and the active space vector. The time duration of switching states is

$$T_a = \frac{\sqrt{3}T_s V_{ref}}{U_d}\sin\left(\frac{\pi}{3}-\theta\right) \tag{2.7}$$

$$T_b = \frac{\sqrt{3}T_s V_{ref}}{U_d}\sin\theta \tag{2.8}$$

$$T_0 = T_s - T_a - T_b \tag{2.9}$$

where T_a, T_b, and T_0 are the dwell time for vectors V_1, V_2, and V_0.

The dwell time for the vectors represents the on- and off- state time of the switches. The reference voltage and the sampling period T_s can be calculated by the eight space vectors. The inverter output phase voltage waveforms in sector III for one switching cycle is shown in Fig. 2.2(b). The sampling period T_s is divided into seven segments.

Using the Backward Euler method, the integration in (2.5) and (2.6) is discretized as

$$\lambda_d(n+1) = \lambda_d(n) + T_s\left[u_d(n+1) - Ri_d(n) + \omega_e(n)\lambda_q(n)\right] \tag{2.10}$$

$$\lambda_q(n+1) = \lambda_q(n) + T_s\left[u_q(n+1) - Ri_q(n) - \omega_e(n)\lambda_d(n)\right] \tag{2.11}$$

where T_s is the sampling period. The IPM machine model is co-simulated with the drive system, using *d*- and *q*-axis reference currents. The reference voltage u_d^* and u_q^* are generated by the PI controller with the close-loop *dq* current error.

u_α^* and u_β^* are calculated by inverse Park transformation as

$$\begin{bmatrix} u_\alpha^* \\ u_\beta^* \end{bmatrix} = \begin{bmatrix} \cos\theta_e & -\sin\theta_e \\ \sin\theta_e & \cos\theta_e \end{bmatrix} \begin{bmatrix} u_d^* \\ u_q^* \end{bmatrix}. \tag{2.12}$$

The output of SVM is the on and off time of each of the six VSI switches. The outputs of the inverter are three-phase voltages. Applying the Park transformation, the three-phase voltages are converted into u_d and u_q.

$$\begin{bmatrix} u_d \\ u_q \end{bmatrix} = \frac{2}{3} \begin{bmatrix} \cos(\theta_e) & \cos\left(\theta_e - \frac{2\pi}{3}\right) & \cos\left(\theta_e + \frac{2\pi}{3}\right) \\ -\sin(\theta_e) & -\sin\left(\theta_e - \frac{2\pi}{3}\right) & -\sin\left(\theta_e + \frac{2\pi}{3}\right) \end{bmatrix} \begin{bmatrix} u_a \\ u_b \\ u_c \end{bmatrix} \tag{2.13}$$

2.3 IPMSM Optimal Operating Regions

For an IPMSM drive system, the optimal operating regions include two parts: the MTPA region and the flux-weakening region. As shown in Fig. 2.3, for a finite-speed IPMSM drive system, the flux-weakening region includes two parts: constant torque part like AB and current constraint part like BC.

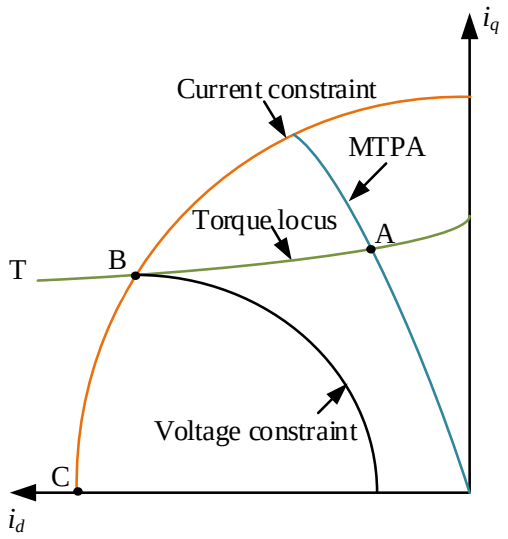

Fig. 2.3 IPMSM operating regions

2.3.1 Maximum Torque per Ampere (MTPA) Region

The MTPA is formed by a series of tangent points of current amplitude circles and torque isolines. The process to solve the MTPA by sweeping the current is as follow:

1) Set the sweep range of amplitude of current and *dq* angle.
2) Calculate the i_d and i_q based on amplitude of current and *dq* angle.

3) Calculate the torque.

4) For each amplitude of the current, find the maximum torque point, and record the *dq* angle of the maximum torque.

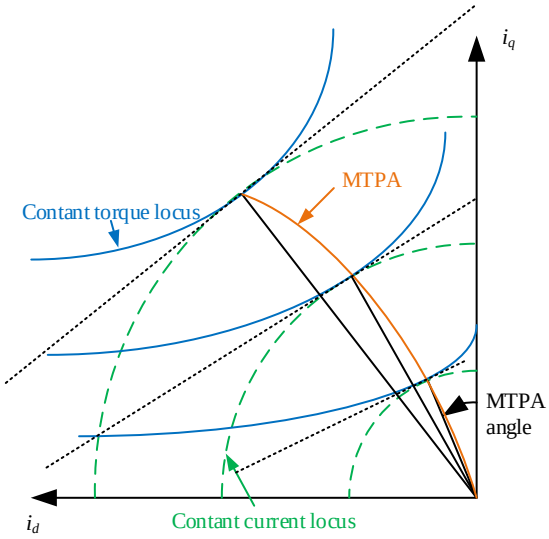

Fig. 2.4 MTPA by sweeping the current

The MTPA can be solved mathematically instead of sweeping the current and *dq* angle. The MTPA trajectory is expressed using optimization as

$$\begin{aligned} &\min \ \ i_d^2 + i_q^2 \\ &s.t. \ \ T_e - \frac{3}{2} P\left[\left(L_d - L_q\right) i_d i_q + \lambda_m i_q\right] = 0 \\ &\quad i_d^2 + i_q^2 \le I_s^2 \end{aligned} \tag{2.14}$$

The MTPA is further solved as [52]

$$i_d + \frac{L_d - L_q}{\lambda_m}\left(i_d^2 - i_q^2\right) = 0\,. \tag{2.15}$$

When $\omega^* \le \omega_b$ and $T_e^* \le T_b$, the optimal point is the intersection of MTPA trajectory and torque locus. The i_d^* and i_q^* are obtained by solving

$$\min \ f_1^2 + f_2^2$$
$$S.t. \begin{cases} f_1 = T_e^* - \dfrac{3}{2} n_p \left[\lambda_m i_q + \left(L_d - L_q \right) i_d i_q \right] \\ f_2 = i_d + \dfrac{L_d - L_q}{\lambda_m} \left(i_d^2 - i_q^2 \right) \end{cases} \tag{2.16}$$

where ω_b is the base speed, and T_b is the torque at base speed.

When $\omega^* \leq \omega_b$ and $T_e^* > T_b$, the optimal point is the intersection of MTPA trajectory and current constraint. The i_d^* and i_q^* are obtained by solving

$$\min \ f_1^2 + f_2^2$$
$$S.t. \begin{cases} f_1 = i_d + \dfrac{L_d - L_q}{\lambda_m} \left(i_d^2 - i_q^2 \right) \\ f_2 = I_{s\max}^2 - i_d^2 - i_q^2 \end{cases} \tag{2.17}$$

When $\omega^* > \omega_b$ and $\omega^* \leq \omega_{MTPAT}$, the optimal point is the intersection of MTPA trajectory and torque locus. The i_d^* and i_q^* are obtained by solving (2.16). ω_{MTPAT} is the speed of the intersection of MTPA trajectory and torque locus.

2.3.2 Flux-Weakening Region

When $\omega^* > \omega_{MTPAT}$ and $i_{dVT}^2 + i_{qVT}^2 < I_{smax}^2$, the optimal point is the intersection of torque locus and voltage constraint. The i_d^* and i_q^* are obtained by solving

$$\min \ f_1^2 + f_2^2$$
$$S.t. \begin{cases} f_1 = T_e^* - \dfrac{3}{2} n_p \left[\lambda_m i_q + \left(L_d - L_q \right) i_d i_q \right] \\ f_2 = \omega^* - \dfrac{V_{s\max}}{\sqrt{\left(L_d i_d + \lambda_m \right)^2 + \left(L_q i_q \right)^2}} \end{cases} \tag{2.18}$$

where i_{dVT} and i_{qVT} are the dq axis currents of the intersection of voltage ellipse and torque curve.

When $\omega^* > \omega_{MTPAT}$ and $i_{dVT}^2 + i_{qVT}^2 \geq I_{smax}^2$, the optimal point is the intersection of current constraint and voltage constraint. The i_d^* and i_q^* are obtained by solving

$$\min \ f_1^2 + f_2^2$$
$$S.t. \begin{cases} f_1 = I_{s\max}^2 - i_d^2 - i_q^2 \\ f_2 = \omega^* - \dfrac{V_{s\max}}{\sqrt{\left(L_d i_d + \lambda_m\right)^2 + \left(L_q i_q\right)^2}} \end{cases} \tag{2.19}$$

By calculating the optimal points for the entire reference speed and reference torque range based on (2.16) - (2.19), the optimal i_d^* and i_q^* LUTs without stator resistance are obtained. The optimal operating points can also be calculated online.

2.4 Existing Flux-Weakening Control Techniques for IPMSMs

The operating regions of IPMSMs are extended to the flux-weakening (FW) region where the wide speed range is required. In FW regions, FW techniques have been proposed, which can be classified as feedback (FB)-based, feedforward (FF)-based, and mixed approaches. By appropriate flux-weakening control, the maximum available torque can be achieved, and the voltage saturation is avoided.

2.4.1 Feedback-Based Flux-Weakening Control

FB-based FW control methods aim at maintaining the output voltages of the current regulators within the voltage limit by using the current or voltage error as the feedback to compensate for the input current. The look-up tables (LUTs) or online calculation of optimal operating points are not required. These methods are robust to the uncertainty of motor parameters due to the closed-loop feedback. However, FB-based FW methods cannot find the optimal operating points to achieve high efficiency. Also, dynamic performance is limited.

Another problem of FB-based flux-weakening control using voltage signals is the confliction between flux-weakening control and antiwindup control. When the phase voltage reference is set to a value that is larger than $Vdc/\sqrt{3}$, there is a part of the region that is out of the voltage hexagon boundary than would not be realized by SVM-based inverter, which can put the system into an unstable situation.

In this region, the antiwindup control are implemented. To keep the stable control of the system, the feedback signal of voltage is used to decrease the *d*-axis current. However, in the voltage extension region, the inconsistency between FB-based FW methods and voltage overmodulation boundary puts the IPMSM control systems into a double squeeze. As shown in Fig. 2.5, the circle, ellipse, and distorted hexagon represent the current constraint, phase voltage reference magnitude, and modulation limit. In Fig. 2.5, an operating point A is located outside the voltage limit. With the flux-weakening control, point A will be moved to A_1, which is on the voltage constraint calculated by voltage equations. With antiwindup control, point A will be moved to A_2, which is on the voltage hexagon limit to avoid losing control of current regulation loops. The operating point is moved to two different points according to two limits: voltage limit of flux-weakening control and SVM-based inverter output hexagon limit. The MI is more difficult to increase because the conflict of two controllers puts the system into the double squeeze.

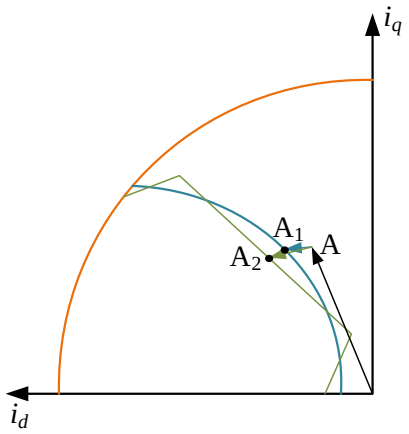

Fig. 2.5 Conflict between flux-weakening control and antiwindup control

- *Current Feedback-based Flux-Weakening Control*

Current FB-based FW control is first proposed in [32], in which the saturation of the current regulator is identified by the current feedback. When i_d^* and i_q^* are out of the voltage constraint, the voltage is saturated. The *d*-axis current error is the feedback signal, which is used to decrease the *q*-axis current when the voltage is saturated. The diagram of the current FB-based FW control is shown in Fig. 2.6.

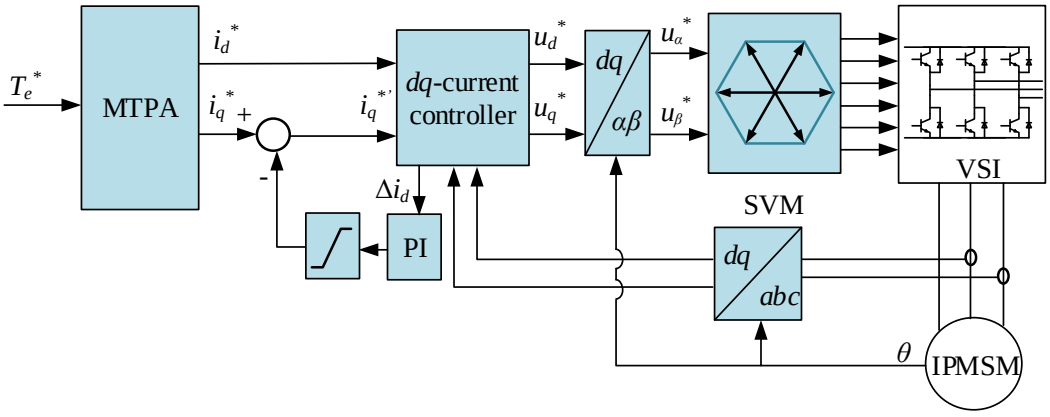

Fig. 2.6 Diagram of the current FB-based FW control

- *Voltage Feedback-based Flux-Weakening Control*

Voltage FB-based FW control includes two types. The first one is using *d*- and *q*- axis voltages as feedback signals. The second one is using *d*- and *q*- axis voltage errors as feedback signals. Using *d*- and *q*- axis voltages as feedback signals to compensate *d*-axis current was proposed in [33]. When the operating point is outer the voltage constraint, the voltage feedback is used to compensate for the *d*-axis current reference. The voltage feedback and the modification of the *q*-axis

current push the operating point to move on the voltage constraint, and to the flux-weakening region.

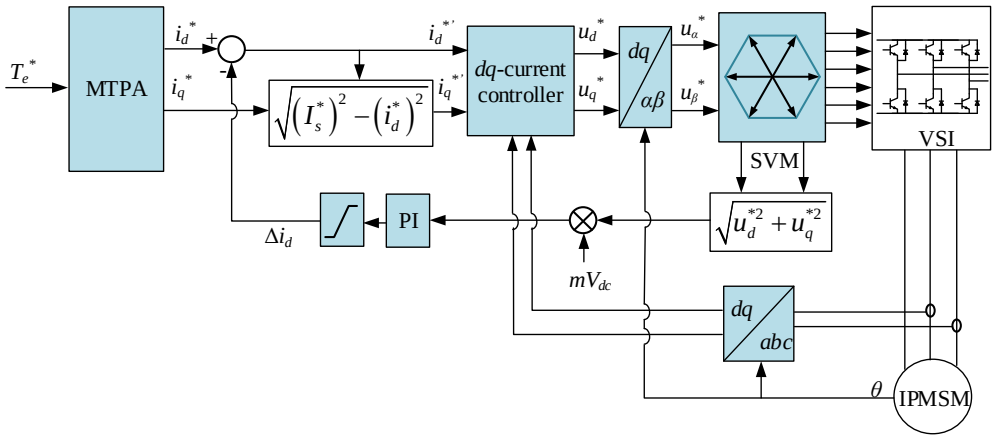

Fig. 2.7 Diagram of the voltage FB-based FW control using *d*-axis and *q*-axis voltages

Using voltage errors as feedback was proposed in [35]. This kind of method can avoid the saturation caused by the maximum phase voltage. Also, the voltage utilization rate is maximized because the confliction between antiwindup control and flux-weakening control is avoided. The *d*-axis and *q*-axis voltage errors are used to compensate *d*-axis current to consider the saturation of both *d*-axis and *q*-axis current regulation loop output voltages. However, the dc-link voltage feedback is not included in voltage FB-based FW control using voltage error, which cannot consider the fluctuation of dc-link voltage provided by batteries in EVs.

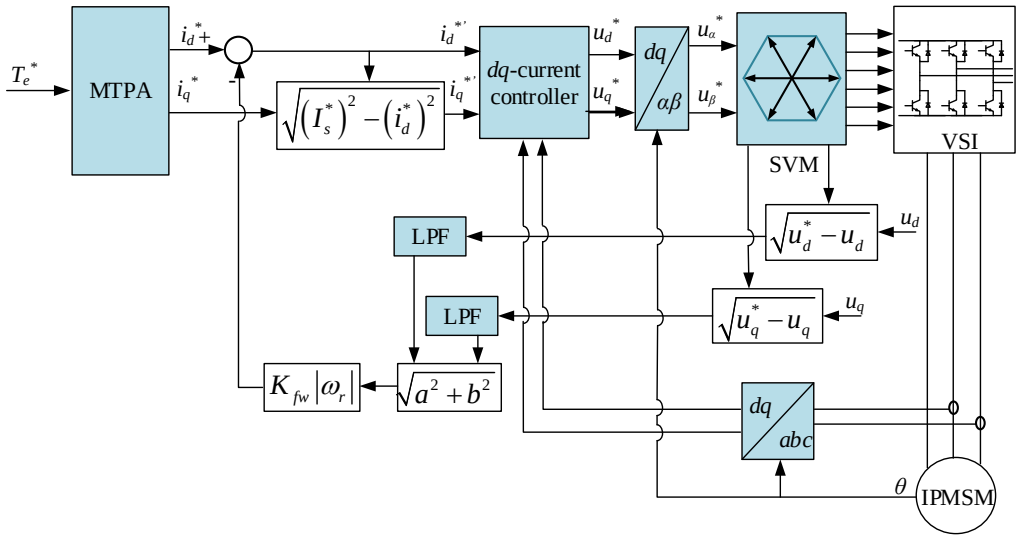

Fig. 2.8 Diagram of the voltage FB-based FW control using voltage errors

There are also other kinds of feedback signals, such as the dwell time of voltage vectors. All the feedback signals like the dwell time of voltage vectors can be derived by current or voltage signals. In [34], the dwell time of the voltage zero vector in the modulation algorithm is used as the feedback to compensate for the *d*-axis current. In [35], the *d*-axis and *q*-axis voltage errors are used to compensate *d*-axis current, and the *q*-axis current is modified according to the current limit and the *d*-axis current. To eliminate the conflicts between two current regulation loops, the single-current-regulator FW methods [36]-[38] are proposed, in which only the *d*-axis current regulator or *q*-axis current regulator is needed. To improve the dynamic performance and the stability of FB-based FW control, the voltage regulation loop is theoretical analyzed and developed in [39]-[41]. The feedback voltage ripple is analyzed and reduced in [41].

2.4.2 Feedforward-Based Flux-Weakening Control

In FF-based FW methods, the optimal operating points are obtained by feedforward LUTs or online calculation. FF-based FW methods guarantee the fast transient performance; however, are sensitive to parameters variation. The performance of FF-based FW methods relies on the accuracy of the feedforward optimal operating points.

In FF-based FW control, the feedforward path contains the optimal operating points in the entire torque and speed range, which include MTPA and flux-weakening regions. The feedforward path is established by LUTs, curve fitting, or online calculation methods, as shown in Fig. 2.9.

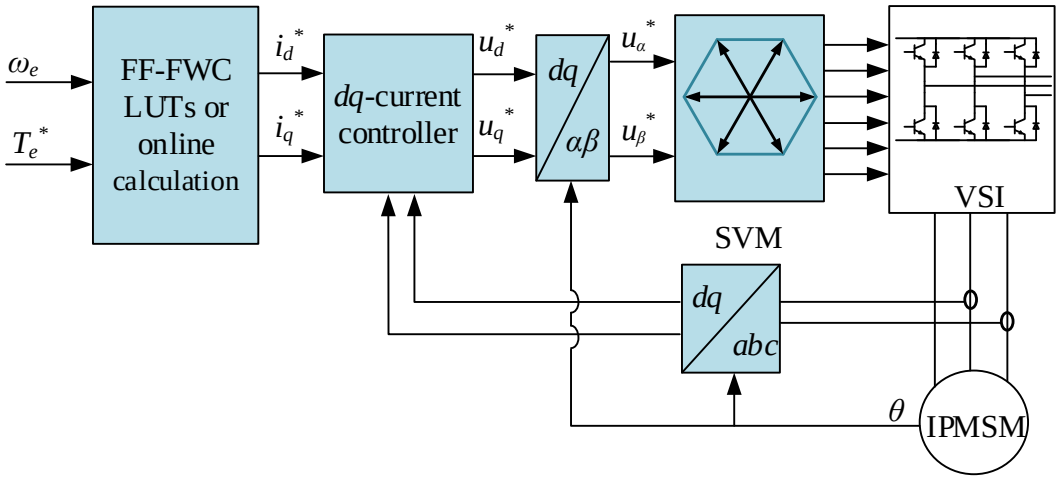

Fig. 2.9 Diagram of the FF-based FW control

In [42]-[45], the optimal current references are calculated online. These methods need less memory space. However, the online calculation has high calculation burden and requires high computational power. The saliency ratio is

particularly considered in [42]. The *d*-axis and *q*-axis inductances are estimated online in [43]. The winding resistance and inverter nonlinearity are considered in [44] and [45], which improves the accuracy of MTPA (maximum torque per ampere) trajectory, MTPV (maximum torque per volt) trajectory, and FW operation. In [45], the condition of dc-link voltage variation is also considered. Except for online calculation, another alternative approach is to store the optimal operating points in LUTs or fitted curves [46]-[48]. Experimental or finite element results are used to construct LUTs. The detailed dimensions of the motor are required if finite element results are used. The dc offset caused by the rotor position error is considered in [46]. The influence of the resistive voltage drop is discussed in [47]. The optimization is employed in [48] to obtain the minimum current for different torque and speed references. The maximum voltage vector is constant in [47] and [48], which don't consider the situation of voltage fluctuation.

2.4.3 Mixed Flux-Weakening Control

For calculating the optimal operating points, there are two kinds of inputs. One uses torque reference and speed as inputs [42]-[48], the other uses torque reference and stator flux linkage reference as inputs [14]-[17]. In [14]-[17], the stator flux linkage reference is adjustable and reflects the voltage saturation. In these methods, the optimal operating points are output by the FF path with the input of the torque reference and stator flux linkage reference, and the stator flux linkage reference is adjusted and compensated by the feedback voltage signal. The FF and

FB paths are both included. These methods are called mixed approaches. The antiwindup control and FW control are achieved at the same time by the mixed approach. The mixed FW control provides the optimal operating points by the feedforward path and refines the optimal solutions by the voltage feedback, which has the fast dynamic performance provided by the feedforward path and avoids the influence of parameters mismatch owing to closed-loop feedback.

In [14], stator flux-linkage reference contains two parts. The first part is calculated by dc-link voltage and ω_e, which is regarded as the main stator flux linkage. The second part is calculated by the difference MI and MI reference MI_ref, which is regarded as the compensated stator flux-linkage reference. However, the MI_ref is set to the constant value, which is not flexible enough and limits the dc-link voltage utilization.

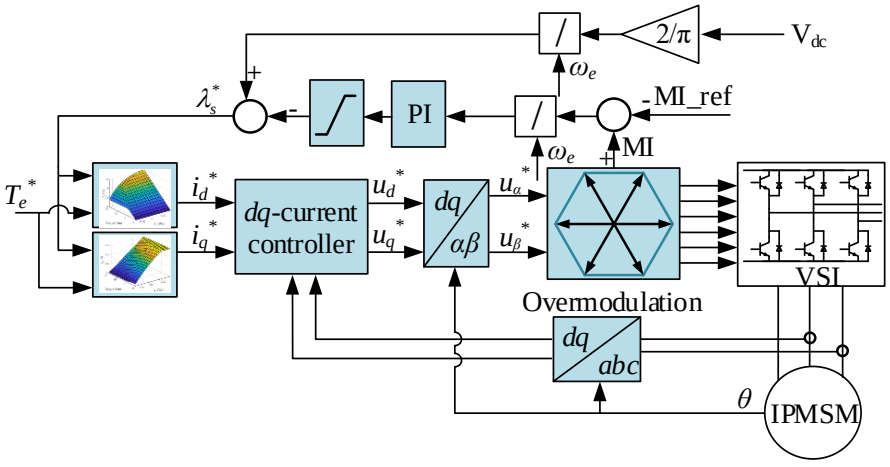

Fig. 2.10 Mixed flux-weakening control in [14]

In [15], a mixed FW control for ramp torque command is proposed. The torque command increases from 0-30Nm, and then decreases from 30-0 Nm. The

current references are on the current constraint when the torque command increases from 0-30Nm, which increases the core loss and reduces motor efficiency.

In [16] and [17], the *d*-axis and *q*-axis voltage differences before and after the modulation algorithm is used to compensate stator flux linkage reference. The dc-link voltage is not included in the feedback loop, in which the dc-link voltage fluctuation is not considered.

The magnetic saturation is considered in [14]-[17] by using nonlinear inductance characteristics. However, to simplify the calculation of optimal current references, the resistive voltage drop is neglect in [14]-[16], which degrades the accuracy of optimal operating points and FW control.

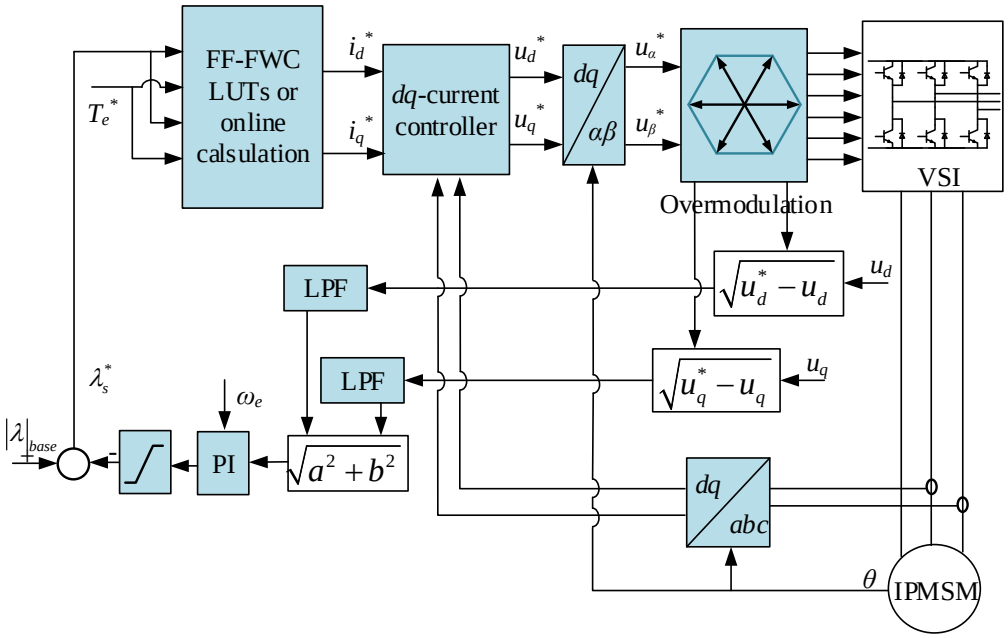

Fig. 2.11 Mixed flux-weakening control in [16][17]

2.5 Summary

The dynamic model [53], operating regions which include MTPA and FW region, and existing flux-weakening methods of IPMSMs are introduced in this chapter. The flux-weakening region includes two parts: the constant torque part and the current constraint part. FB-based FW methods are robust to the uncertainty of motor parameters; However, cannot find the optimal operating points to achieve high efficiency. Also, the dynamic performance is limited. FF-based FW methods guarantee the fast transient performance; however, are sensitive to parameters variation. The mixed FW control provides the optimal operating points by the feedforward path and refines the optimal solutions by the voltage feedback, which has the fast dynamic performance provided by the feedforward path and avoids the parameters mismatch owing to closed-loop feedback. However, the present mixed FW methods have their limitations.

Chapter 3
Proposed Flux-Weakening Control Strategy for IPMSMs with Constant Parameters

3.1 Introduction

In this chapter, a flux-weakening control strategy based on the mixed method is proposed for IPMSMs, which increases the dc-link voltage utilization rate, and improves the tracking performance. The overmodulation is implemented by modifying the time interval of the active voltage vectors in the SVM. The torque-stator flux linkage-current LUTs are used to derive the optimal current references. The stator flux linkage reference is adjusted based on the torque reference, speed, and MI.

3.2 IPMSM Operating Constraints

At steady state, the *d*-axis voltage, u_d, and *q*-axis voltage, u_q, in synchronous rotating reference frame can be expressed as in (3.1) and (3.2)

$$u_d = -\omega_e L_q i_q + R_s i_d \tag{3.1}$$

$$u_q = \omega_e (L_d i_d + \lambda_m) + R_s i_q \tag{3.2}$$

where L_d and L_q represent the *d*-axis and *q*-axis inductances, respectively. λ_m denotes the permanent magnet flux linkage, and ω_e is the angular electrical frequency. The electromagnetic torque T_e is expressed as

$$T_e = \frac{3}{2} n_p \left[\lambda_m i_q + \left(L_d - L_q \right) i_d i_q \right] \tag{3.3}$$

where n_p is the number of pole pairs.

The maximum current I_{smax} of an IPMSM is normally related to the motor itself and inverter thermal limit. The current references should satisfy

$$i_d^{*2} + i_q^{*2} \le I_{s\max}^2 . \tag{3.4}$$

The voltage limit V_{smax} is related to the dc-link voltage and modulation techniques. The voltage constraint is expressed as

$$u_d^{*2} + u_q^{*2} \le V_{s\max}^2 . \tag{3.5}$$

When the phase winding resistance is neglected at the steady state, the voltage constraint is simplified as

$$\sqrt{\left(L_d i_d + \lambda_m \right)^2 + \left(L_q i_q \right)^2} \le \frac{V_{s\max}}{\omega_e} . \tag{3.6}$$

The maximum current per ampere (MTPA) condition is expressed as

$$i_d + \frac{L_d - L_q}{\lambda_m}\left(i_d^2 - i_q^2\right) = 0\,. \tag{3.7}$$

3.3 Proposed Flux-Weakening Control Strategy

3.3.1 Overmodulation Technique and Flux Regulator

The MI is defined as

$$MI = \frac{\pi V_{ref}}{2V_{dc}} = \frac{\pi\sqrt{u_d^2 + u_q^2}}{2V_{dc}} \tag{3.8}$$

where V_{ref} is the reference voltage.

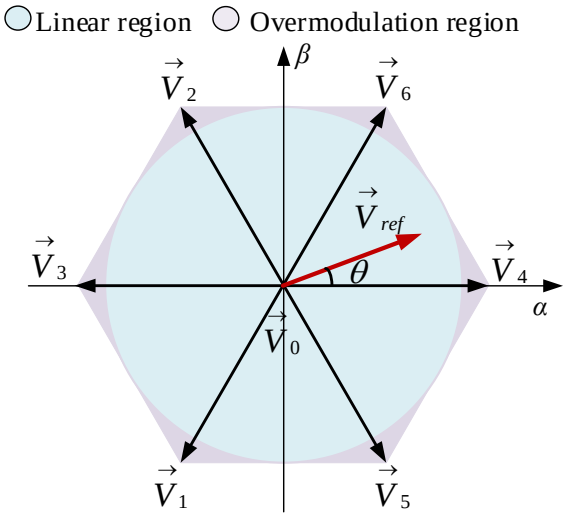

Fig. 3.1 Diagram of space vectors and the overmodulation region.

When MI = 0.906, the reference voltage is the largest inner circle of the hexagon, which is the maximum voltage in the linear modulation region, as shown in Fig. 3.1.

The overmodulation region is determined by the time interval of the zero space vector T_0. The overmodulation algorithm is implemented when $T_0 < 0$. When $T_0 < 0$ and $T_1 > T_s$, T_1 and T_2 are corrected as $T_1^{'} = T_s$ and $T_2^{'} = 0$. When $T_0 < 0$ and $T_2 > T_s$, T_1 and T_2 are corrected as $T_1^{'} = 0$ and $T_2^{'} = T_s$. When $T_1 < T_s$, $T_2 < T_s$, and $T_0 < 0$, T_1 and T_2 are corrected as

$$T_1^{'} = \frac{T_1 T_s}{T_1 + T_2}, T_2^{'} = \frac{T_2 T_s}{T_1 + T_2} \tag{3.9}$$

where T_s represents the sampling period. T_1 and T_2 denote the time interval of two active space vectors, respectively.

The proposed flux regulator is shown in Fig. 3.2. MI is calculated by u_d, u_q, and V_{dc}. λ_1 is calculated as the intersection of the torque reference and current limit, which is the minimum stator flux linkage for required torque reference. When MI is lower than the MI limit and $\lambda_s^* < \lambda_1$, λ_s^* is increased. This means the stator flux linkage reference λ_s^* is increased when $\lambda_s^* < \lambda_1$, and the PWM output is within the maximum boundary of the overmodulation limit. The voltage ellipse is expanded. The increase of λ_s^* would not stop until λ_s^* is larger than or equal to λ_1, or the maximum boundary of the overmodulation limit is reached.

The upper and lower limits of MI are defined in a hysteresis controller block. The upper limit is set to 1, and the lower limit is set to 0.906.

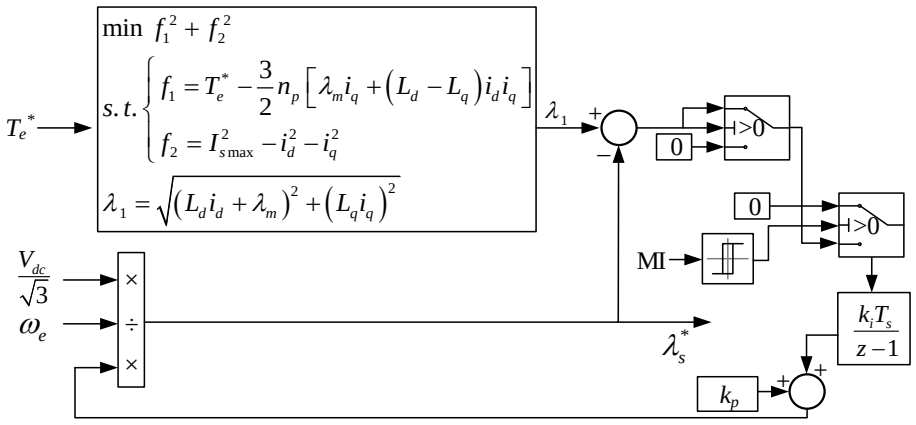

Fig. 3.2 Diagram of the flux regulator.

3.3.2 Current Predictive Controller

Instead of using a proportional-integral (PI) controller, a current predictive controller, which predicts the future dynamic behavior of the currents, is carried out, to improve the tracking performance. The objective is to minimize the difference between the current reference and the predicted current.

The voltage equations are expressed in state-variable form as

$$\begin{bmatrix} \frac{di_d}{dt} \\ \frac{di_q}{dt} \end{bmatrix} = \begin{bmatrix} -\frac{R_s}{L_d} & 0 \\ 0 & -\frac{R_s}{L_q} \end{bmatrix} \begin{bmatrix} i_d \\ i_q \end{bmatrix} + \begin{bmatrix} \frac{1}{L_d} & 0 \\ 0 & \frac{1}{L_q} \end{bmatrix} \begin{bmatrix} u_d \\ u_q \end{bmatrix} + \begin{bmatrix} \frac{\omega_e L_q i_q}{L_d} \\ -\frac{\omega_e \left(L_d i_d + \lambda_m \right)}{L_q} \end{bmatrix} . \quad (3.10)$$

By employing the Euler approximation, the discrete-time form of (3.10) is expressed as

$$x(k+1) = Ax(k) + Bu(k) + C \tag{3.11}$$

where T_s is the sampling period, and the matrix A, B, and C are expressed as

$$x = \begin{bmatrix} i_d \\ i_q \end{bmatrix}, A = \begin{bmatrix} 1 - \frac{T_s R_s}{L_d} & 0 \\ 0 & 1 - \frac{T_s R_s}{L_q} \end{bmatrix},$$

$$B = \begin{bmatrix} \frac{T_s}{L_d} & 0 \\ 0 & \frac{T_s}{L_q} \end{bmatrix}, C = \begin{bmatrix} \frac{T_s \omega_e(k) L_q i_q(k)}{L_d} \\ -\frac{T_s \omega_e(k)\left(L_d i_d(k) + \lambda_m\right)}{L_q} \end{bmatrix}.$$

According to (3.11), the predicted current is expressed as

$$\hat{x}(k+1) = Ax(k) + Bu(k) + C\,. \tag{3.12}$$

The performance indexes of *d*-axis and *q*-axis currents are expressed as

$$\begin{bmatrix} J_d \\ J_q \end{bmatrix} = \begin{Bmatrix} \left[\hat{i}_d(k+1) - i_d^*(k+1)\right]^2 \\ \left[\hat{i}_q(k+1) - i_q^*(k+1)\right]^2 \end{Bmatrix}. \tag{3.13}$$

To minimize the cost function of currents and obtain the optimal voltages,

$$\begin{bmatrix} \frac{\partial J_d}{\partial u_d} \\ \frac{\partial J_q}{\partial u_q} \end{bmatrix} = \begin{Bmatrix} \frac{\partial\left[\hat{i}_d(k+1) - i_d^*(k+1)\right]^2}{\partial u_d} = 0 \\ \frac{\partial\left[\hat{i}_q(k+1) - i_q^*(k+1)\right]^2}{\partial u_q} = 0 \end{Bmatrix}. \tag{3.14}$$

By solving (3.14), the optimized voltage references are calculated by

$$\begin{bmatrix} u_d^*(k) \\ u_q^*(k) \end{bmatrix} = \begin{bmatrix} R_s - \frac{L_d}{T_s} & 0 \\ 0 & R_s - \frac{L_q}{T_s} \end{bmatrix} \begin{bmatrix} i_d(k) \\ i_q(k) \end{bmatrix} + \begin{bmatrix} \frac{L_d}{T_s} & 0 \\ 0 & \frac{L_q}{T_s} \end{bmatrix} \begin{bmatrix} i_d^*(k+1) \\ i_q^*(k+1) \end{bmatrix} + \begin{bmatrix} -\omega_e(k) L_q i_q(k) \\ \omega_e(k)\left(L_d i_d(k) + \lambda_m\right) \end{bmatrix} . \quad (3.15)$$

3.4 Simulation Validation

The diagram of the IPMSM control system is shown in Fig. 3.3, which includes the optimal current reference LUTs, flux regulator, current predictive controller, overmodulation block, voltage source inverter (VSI), and the IPMSM. The stator flux linkage reference is adjusted by the flux regulator. The optimal current references for the given T_e^* and λ_s^* are obtained from LUTs. The current reference LUTs shown in Fig. 3.4 are derived from (3.3) - (3.7) for different T_e^* and λ_s^*. Table 3.1 shows the specifications of the reference IPMSM. In the following discussions, the simulation results obtained from the conventional method and the proposed method are compared. In the conventional method, the stator flux linkage reference is constant and calculated by (3.6) in the simulation with the PI controller. In the proposed method, the stator flux linkage is derived from the proposed flux regulator, and the PI controller is replaced by the current predictive controller. Fig. 3.5 (a) and (b) compare the simulated torque and power obtained from the conventional method and the proposed method. It can be observed that the torque

and power increase in the proposed method because of the proposed flux regulator and overmodulation technique. The voltage utilization rate is increased. The voltage trajectory is extended to the overmodulation region, as shown in Fig. 3.5(c).

Fig. 3.6 compares the dynamic *d*-axis and *q*-axis currents of the conventional method and the proposed method when the motor speed varies from 500 r/min to 1600 r/min. The torque command changes from 10 Nm to 20 Nm at 0.25s. The proposed method exhibits smaller tracking errors and faster tracking performance compared to the conventional method. Fig. 3.7 shows that the torque tracking performance of the proposed method is faster when the motor speed changes from 500 r/min to 1600 r/min, owning to the current predictive controller. Besides, the torque of the proposed method is increased in the flux-weakening region. In Fig. 3.6 and Fig. 3.8, the current error is calculated by

$$\Delta i(t) = i^{*}(t) - i(t). \tag{3.16}$$

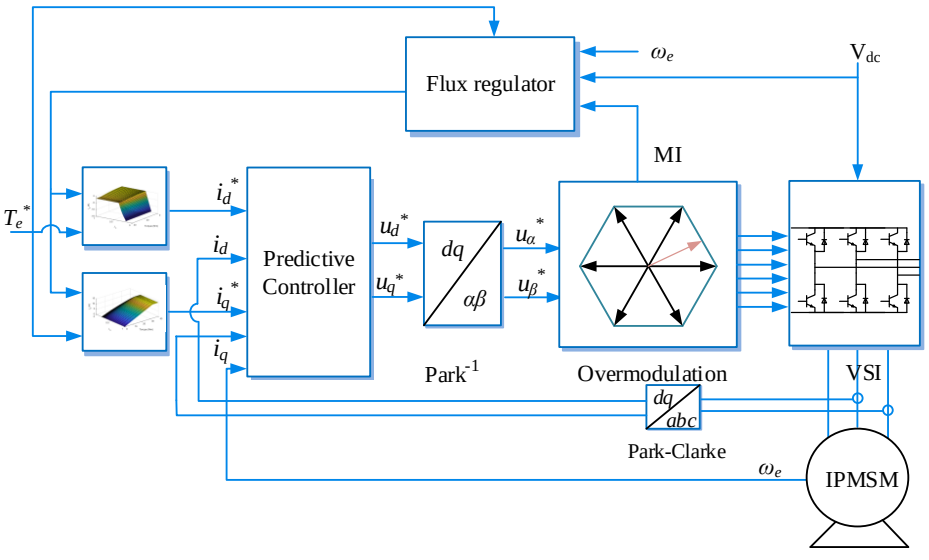

Fig. 3.3 Diagram of the IPMSM control system.

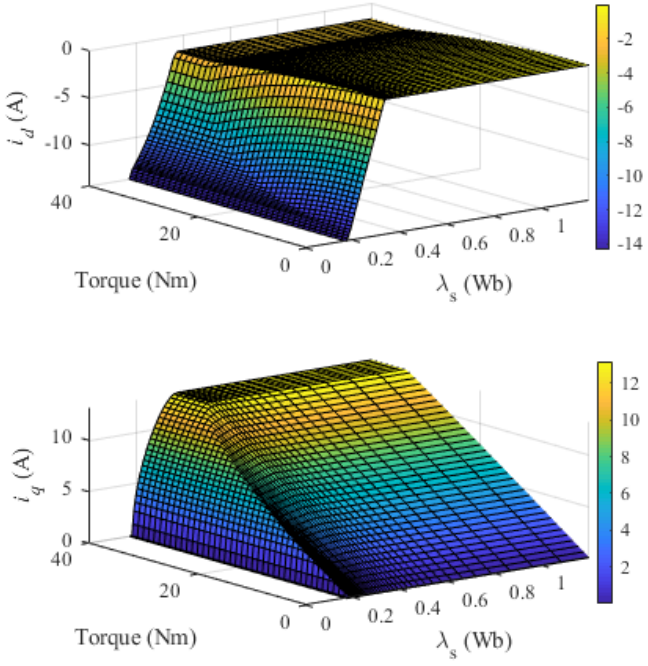

Fig. 3.4 Optimal current references corresponding to torque and stator flux linkage.

Table 3.1 IPMSM Specifications

Details	Value
DC-link voltage	300 V
Rated current	9.4 A
Number of pole pairs	5
d-axis inductance	11 mH
q-axis inductance	14.3 mH
PM flux linkage	0.333 Wb
Rated speed	900 r/min
Rated torque	33.5 Nm

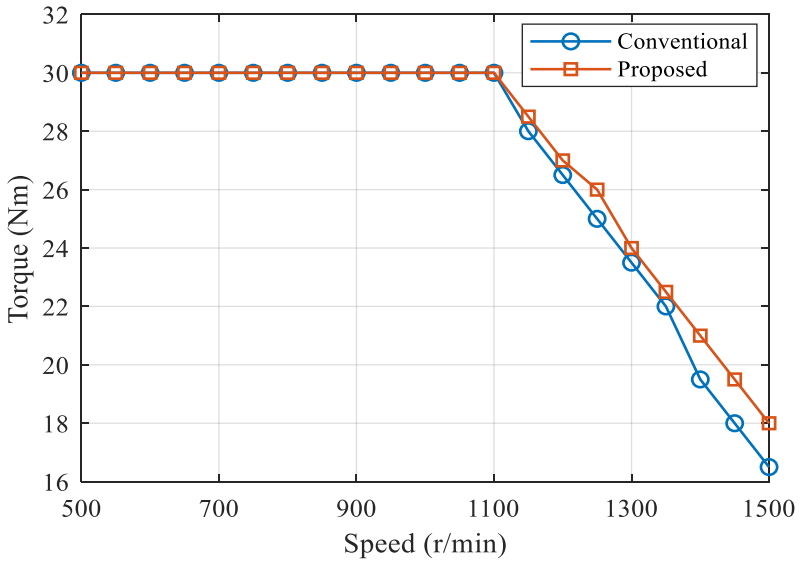
Conventional
Proposed
Torque (Nm)
Speed (r/min)
32
30
28
26
24
22
20
18
16
500
700
900
1100
1300
1500

(a)

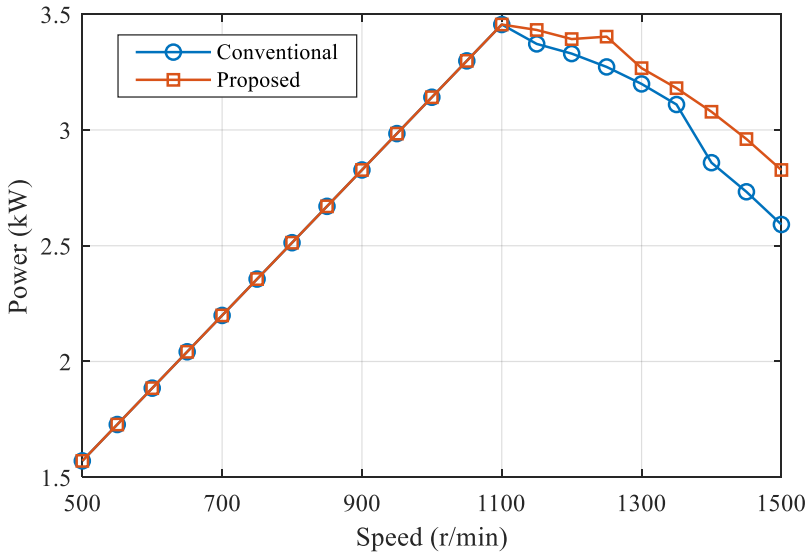
Conventional
Proposed
Power (kW)
Speed (r/min)
3.5
3
2.5
2
1.5
500
700
900
1100
1300
1500

(b)

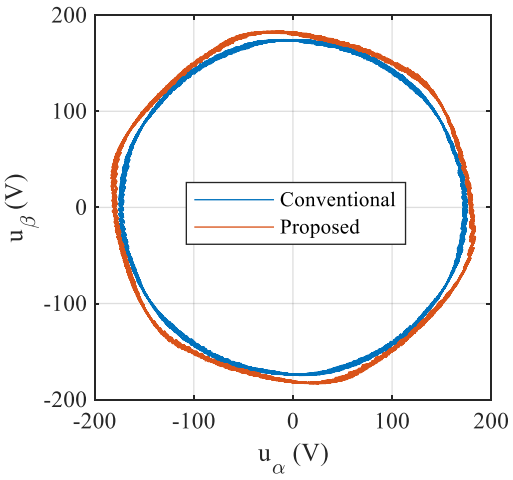

(c)

Fig. 3.5 Simulation results. Comparison between the conventional method and the proposed method. (a) Torque versus speed. (b) Power versus speed. (c) Voltage trajectory.

Fig. 3.8 compares the dynamic *d*-axis and *q*-axis currents of the conventional method and the proposed method. The speed changes from 500 r/min to 1400 r/min, and the torque command varies from 10 Nm to 30 Nm at 0.25s. Fig. 3.9 shows that the proposed method has faster torque tracking performance because of the current predictive controller. Besides, the average torque of the proposed method is increased in the flux-weakening region. This is due to the proposed flux regulator and overmodulation technique. The output voltage is extended to the quasi-six-step and six-step modes. It can be seen that the torque ripple increases with the torque. This is because the voltage overmodulation is applied, which increases the harmonic distortion in voltage. Therefore, higher current ripple and torque ripple are obtained.

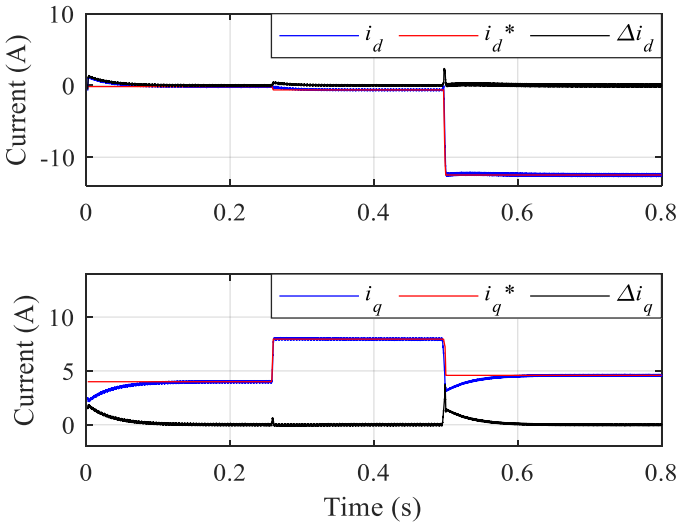

(a)

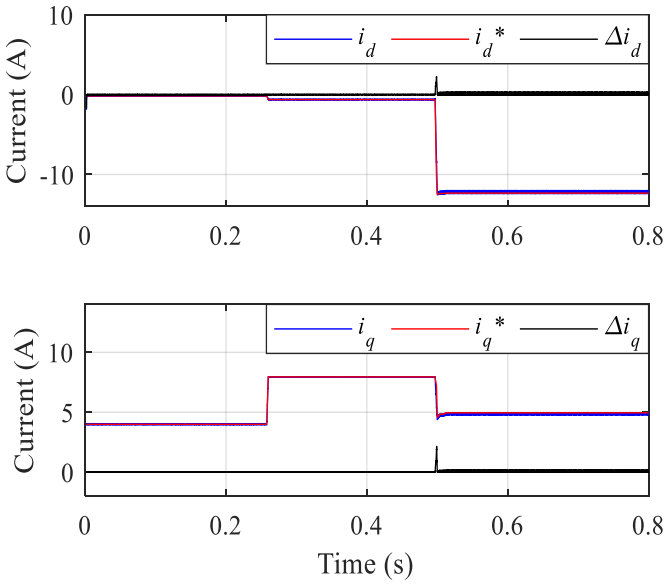

(b)

Fig. 3.6 Dynamic currents comparison between the conventional and proposed methods when the speed changes from 500 r/min to 1600 r/min. (a) Conventional. (b) Proposed.

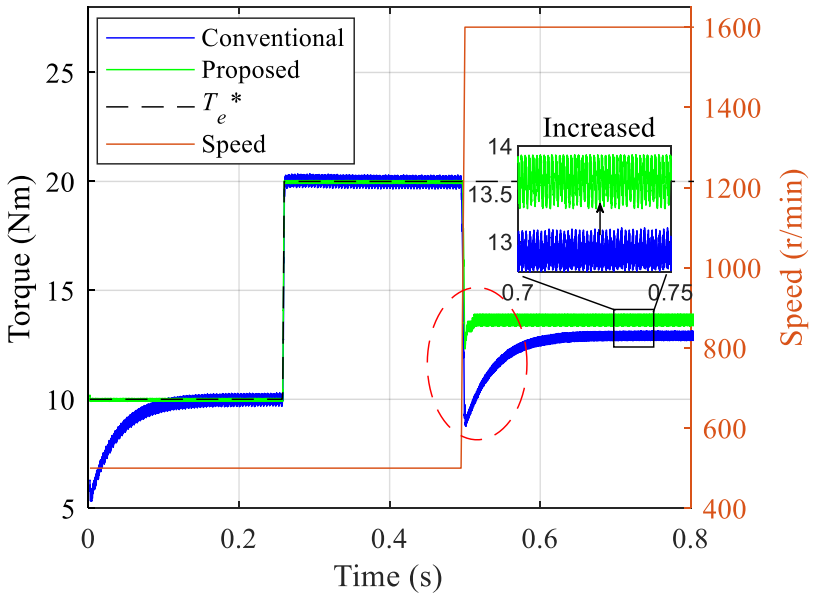

Fig. 3.7 Torque response comparison between the conventional and proposed methods when the speed changes from 500 r/min to 1600 r/min.

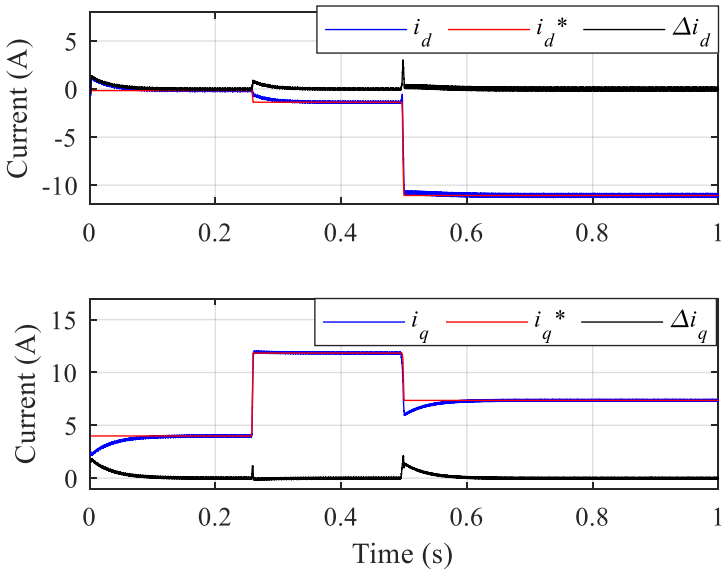

(a)

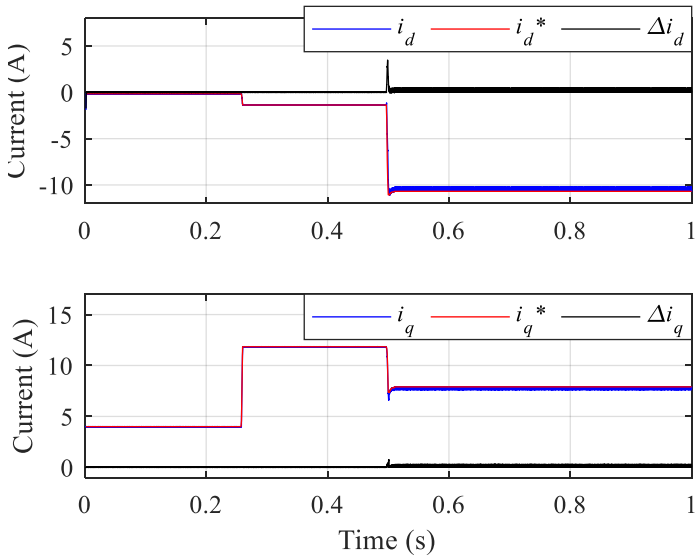

(b)

Fig. 3.8 Dynamic currents comparison between the conventional and proposed methods when the speed changes from 500 r/min to 1400 r/min. (a) Conventional. (b) Proposed.

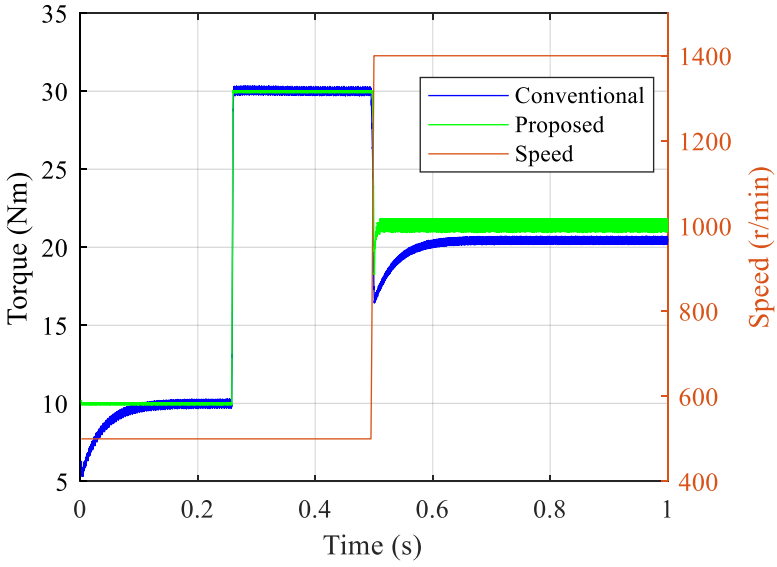

Fig. 3.9 Torque response comparison between the conventional and proposed methods when the speed changes from 500 r/min to 1400 r/min.

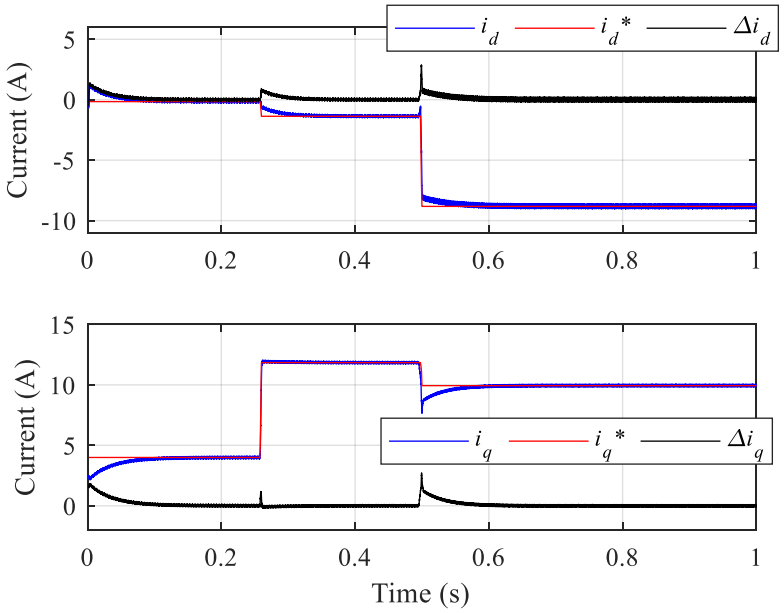

(a)

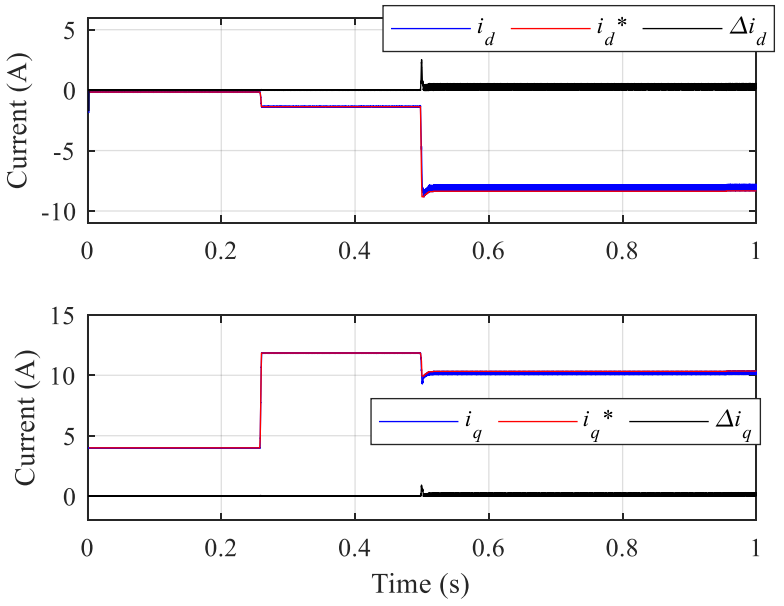

(b)

Fig. 3.10 Dynamic currents comparison between the conventional and proposed methods when the speed changes from 500 r/min to 1200 r/min. (a) Conventional. (b) Proposed.

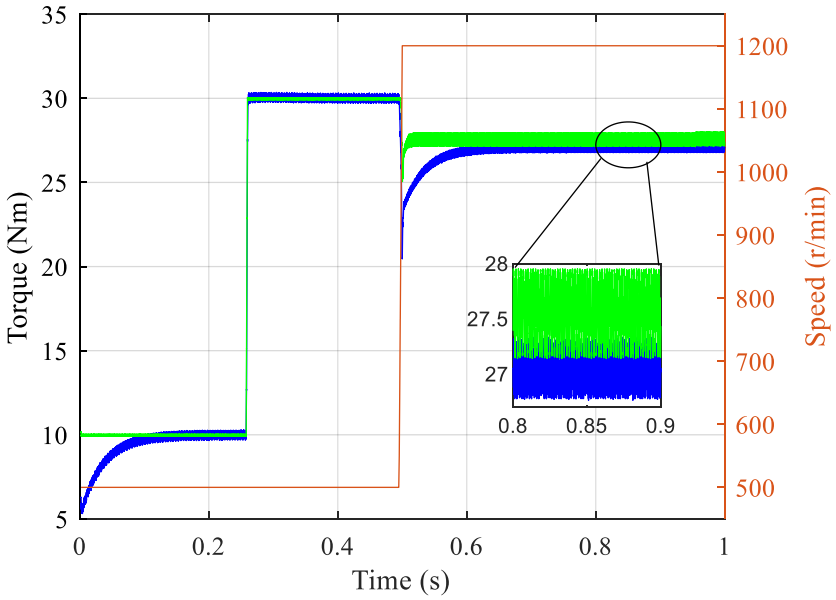

Fig. 3.11 Torque response comparison between the conventional and proposed methods when the speed changes from 500 r/min to 1200 r/min.

Fig. 3.10 compares the dynamic *d*-axis and *q*-axis currents of the conventional method and the proposed method. The speed changes from 500 r/min to 1200 r/min at 0.5s, and the torque command varies from 10 Nm to 30 Nm at 0.25s. Fig. 3.11 shows that the proposed method has faster torque tracking performance. Besides, the average torque of the proposed method is increased at 1200 r/min.

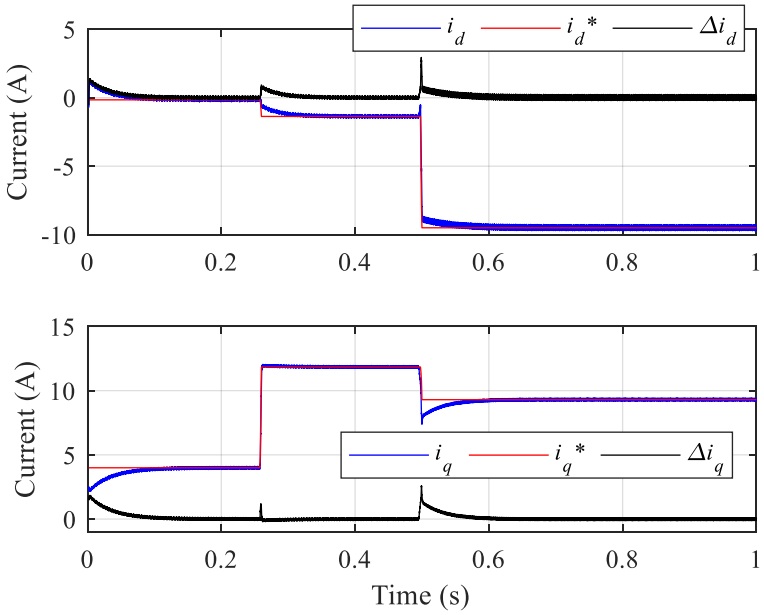

(a)

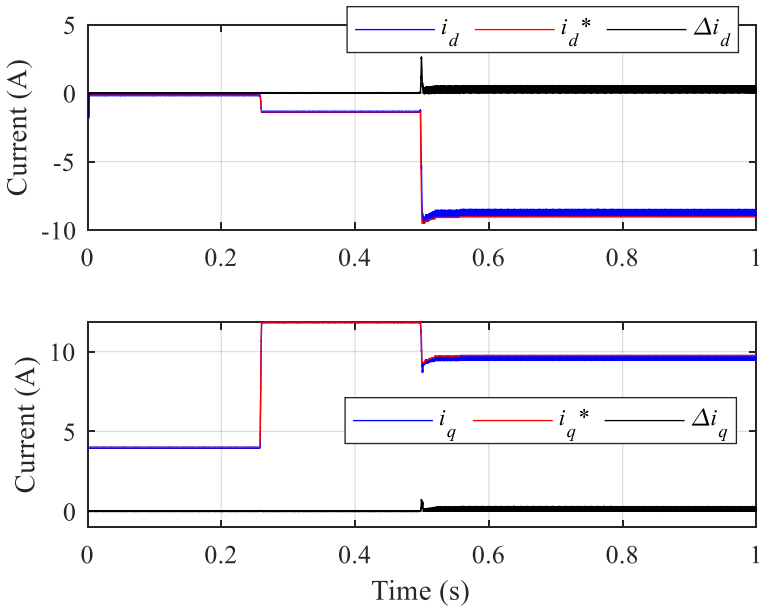

(b)

Fig. 3.12 Dynamic currents comparison between the conventional and proposed methods when the speed changes from 500 r/min to 1250 r/min. (a) Conventional. (b) Proposed.

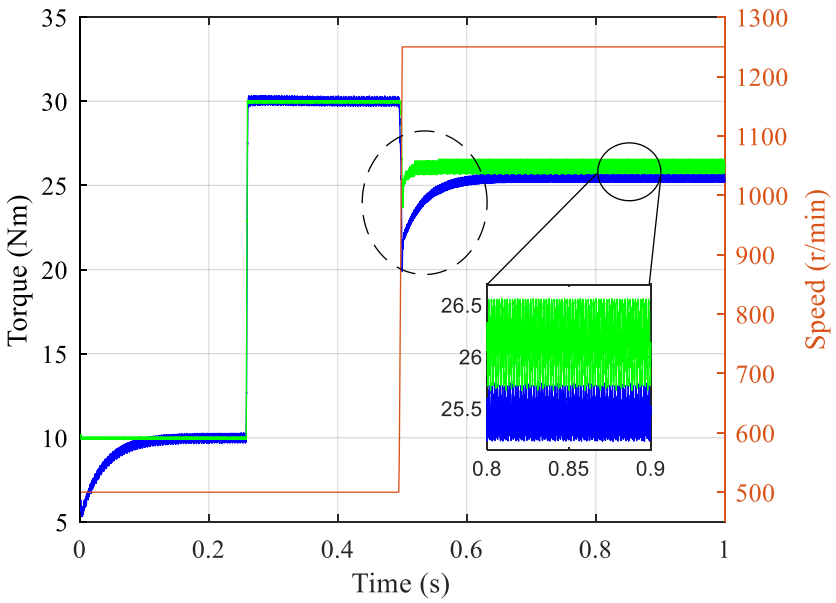

Fig. 3.13 Torque response comparison between the conventional and proposed methods when the speed changes from 500 r/min to 1250 r/min.

Fig. 3.12 compares the dynamic *d*-axis and *q*-axis currents of the conventional method and the proposed method. The speed changes from 500 r/min to 1250 r/min at 0.5s, and the torque command varies from 10 Nm to 30 Nm at 0.25s. Fig. 3.13 shows that the proposed method has faster torque tracking performance. Besides, the average torque of the proposed method is increased in the flux-weakening region.

3.5 Conclusion

In this chapter, a novel flux-weakening control strategy for IPMSMs is proposed, which extends the dc-link voltage utilization and improves the tracking

performance. The overmodulation region is achieved by the flux regulator. The torque and power are increased. The tracking performance is improved by the current predictive controller. Compared to the conventional method, the proposed method increases the torque and power with improved tracking performance[54].

Chapter 4
Proposed Flux-Weakening Control Strategy Considering Magnetic Saturation and Resistive Voltage Drop

4.1 Introduction

In the previous chapter, the flux-weakening (FW) control method with constant parameters has been presented. In this chapter, the flux-weakening method considering the resistive voltage drop and magnetic saturation is proposed. A new stator flux linkage adjustment (SFLA) method is proposed in the proposed flux-weakening method. In the proposed SFLA method, the stator flux linkage is adjusted based on MI, torque reference, and operating speed. To improve the dynamic performance, there are two feedback paths in the proposed FW method. The feedback path is chosen based on the torque reference and operating speed. The resistive voltage drop and magnetic saturation are considered to improve the accuracy of FW control.

4.2 Influence Analysis of Magnetic Saturation and Resistive Voltage Drop

4.2.1 Magnetic Saturation

In the rotating reference frame, the voltage equations for IPMSMs are written as

$$u_d = R_s i_d + \frac{d\left(L_d i_d + \lambda_m\right)}{dt} - \omega_e L_q i_q \tag{4.1}$$

$$u_q = R_s i_q + \frac{dL_q i_q}{dt} + \omega_e \left(L_d i_d + \lambda_m\right) \tag{4.2}$$

where u_d and u_q represent the d-axis and q-axis voltages, i_d and i_q denote the d-axis and q-axis currents, L_d and L_q are the d-axis and q-axis inductances, respectively. R_s is the stator resistance. λ_m is the permanent magnet flux linkage. ω_e denotes the electrical angular frequency. The electromagnetic torque is written as

$$T_e = \frac{3}{2} P\left[\left(L_d - L_q\right) i_d i_q + \lambda_m i_q\right] \tag{4.3}$$

where P is the number of pole pairs.

The current constraint is related to the inverter thermal limit. The maximum current satisfies

$$i_d^2 + i_q^2 \le I_{s\max}^2 \tag{4.4}$$

The voltage constraint is related to modulation techniques and the dc-link voltage. The maximum voltage satisfies

$$u_d^2 + u_q^2 \le V_{s\max}^2 \tag{4.5}$$

The MTPA trajectory is expressed using optimization as

$$\begin{aligned} &\min \ \ i_d^2 + i_q^2 \\ &s.t. \ \ T_e - \frac{3}{2} P\left[\left(L_d - L_q\right) i_d i_q + \lambda_m i_q\right] = 0 \\ &\quad i_d^2 + i_q^2 \le I_s^2 \end{aligned} \tag{4.6}$$

To obtain the optimal current LUTs and ensure the accuracy of FW control, accurate inductance characteristics are required. The inductances vary nonlinearly due to the magnetic saturation, which are functions of currents. The nonlinear inductance LUTs are constructed based on the experimental test in this chapter. The dyno motor drives the IPMSM at 600 r/min, which is close to and lower than the base speed. The speed should be lower than the base speed to prevent voltage saturation. The speed should be close to the base speed to reduce the influence of measurement error. The *d*-axis and *q*-axis currents are controlled and recorded. The *d*-axis current reference is from -6A to 0A with the interval of 2A, and the *q*-axis current reference is from 0A to 6A with the interval of 2A. The *d*-axis and *q*-axis voltages with averaged values are recorded. The interpolation is used to expand the inductance tables. The nonlinear inductances are calculated by steady state voltage equations, which are expressed as

$$L_q\left(i_d, i_q\right) = \frac{R_s i_d - u_d}{\omega_e i_q} \tag{4.7}$$

$$L_d\left(i_d, i_q\right) = \frac{u_q - R_s i_q}{\omega_e i_d} - \frac{\lambda_m}{i_d} \tag{4.8}$$

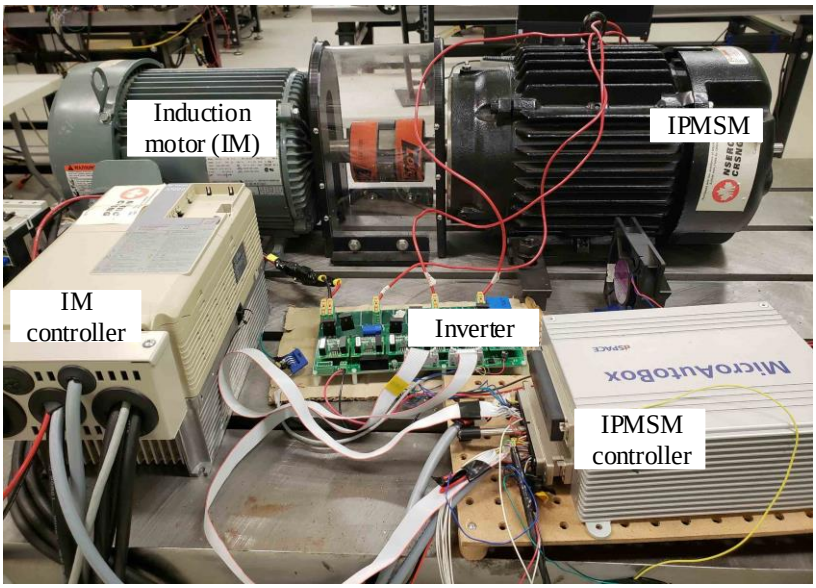

Fig. 4.1 Motor dyno setup

The dyno setup for IPMSM characterization is shown in Fig. 4.1. An Induction motor (IM) is used as the dyno motor, which is driven by a YASKAWA drive. The IPMSM control algorithms are implemented in MicroAutobox II. The IM works in speed control mode and drives the tested IPMSM at the given speed. The test IPMSM works in the current control mode. The sampling frequency is 10kHz.

The *d*-axis and *q*-axis inductances obtained by the experimental test are shown in Fig. 4.2. The comparison of the optimal operating region with or without considering magnetic saturation is shown in Fig. 4.3.

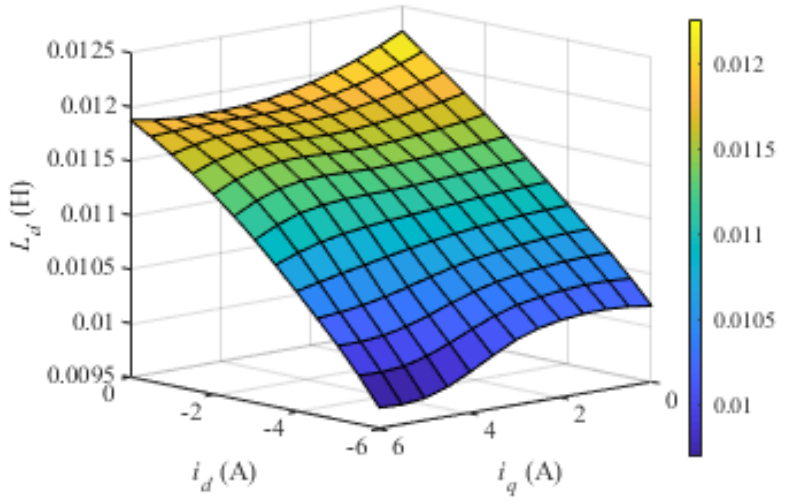

(a)

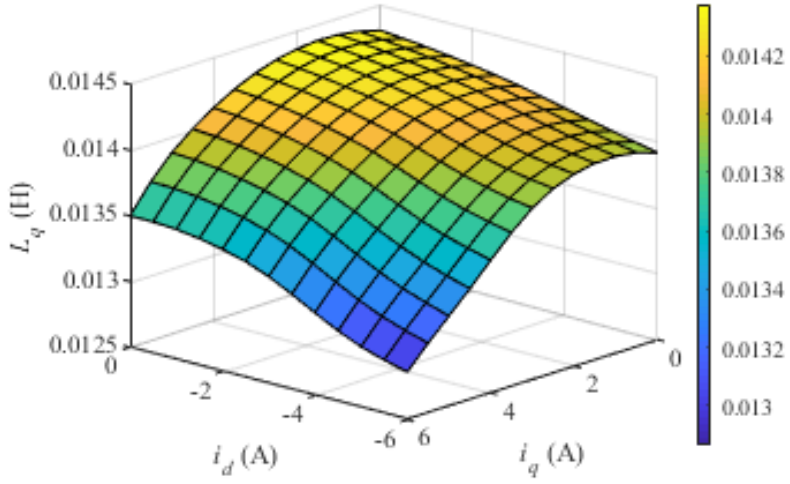

(b)

Fig. 4.2 *d*-axis and *q*-axis inductances as functions of currents by experimental test. (a) *d*-axis inductance. (b) *q*-axis inductance.

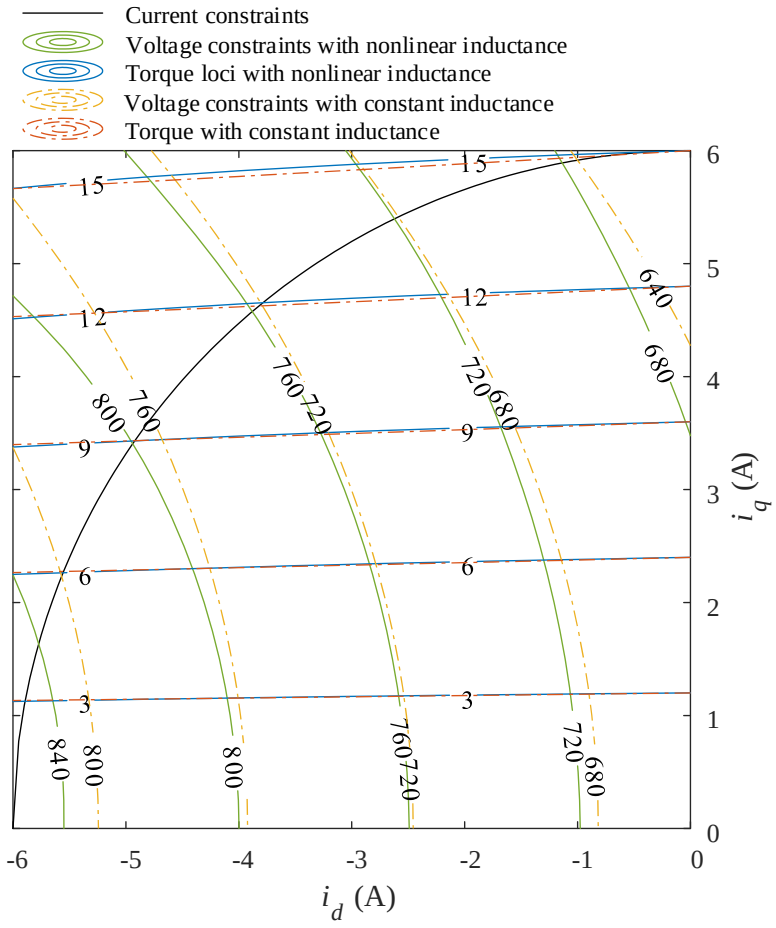

Fig. 4.3 Comparison of the optimal operating region with or without considering magnetic saturation

4.2.2 Resistive Voltage Drop

The voltage equations (4.9) and (4.10) at steady state considering the resistive voltage drop are written as

$$u_d = R_s i_d - \omega_e L_q \left(i_d, i_q\right) i_q \tag{4.9}$$

$$u_q = R_s i_q + \omega_e \left[L_d \left(i_d, i_q\right) i_d + \lambda_m \right] \tag{4.10}$$

By combining (4.5), (4.9) and (4.10), the voltage constraint considering the resistive voltage drop is rewritten as

$$\left[R_s i_d - \omega_e L_q \left(i_d, i_q\right) i_q \right]^2 + \left[R_s i_q + \omega_e L_d \left(i_d, i_q\right) i_d + \omega_e \lambda_m \right]^2 \le V_{s\max}^2 \tag{4.11}$$

Voltage constraint (4.11) can be drawn as a series of ellipses. The voltage limit ellipse is shrunk with the increase of the speed. The general equation of the voltage limit ellipses can be rewritten based on (4.11) as

$$a i_d^2 + b i_q^2 + c i_d i_q + d i_d + e i_q + f = 0 \tag{4.12}$$

where *a*, *b*, *c*, *d*, *e*, and *f* are expressed as

$$\begin{cases} a = \left[\omega_e L_d \left(i_d, i_q\right) \right]^2 + R_s^2, \ b = \left[\omega_e L_q \left(i_d, i_q\right) \right]^2 + R_s^2 \\ c = 2\omega_e R_s \left[L_d \left(i_d, i_q\right) - L_q \left(i_d, i_q\right) \right], \ d = 2\omega_e^2 L_d \left(i_d, i_q\right) \lambda_m \\ e = 2\omega_e R_s L_q \left(i_d, i_q\right), \ f = \omega_e^2 \lambda_m^2 - V_{s\max}^2 \end{cases} \tag{4.13}$$

As shown in Fig. 4.4, if the resistive voltage drop is considered, the intersection of the current limit circle and the voltage limit ellipse moves from point A to point B. Fig. 4.5 shows the comparison of voltage constraints between

considering and without resistive voltage drop at different speeds. The stator resistance is measured by Micro-Ohmmeter.

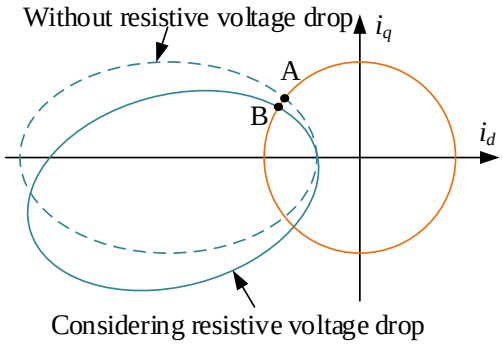

Fig. 4.4 Comparison of the voltage constraint ellipse with or without considering resistive voltage drop

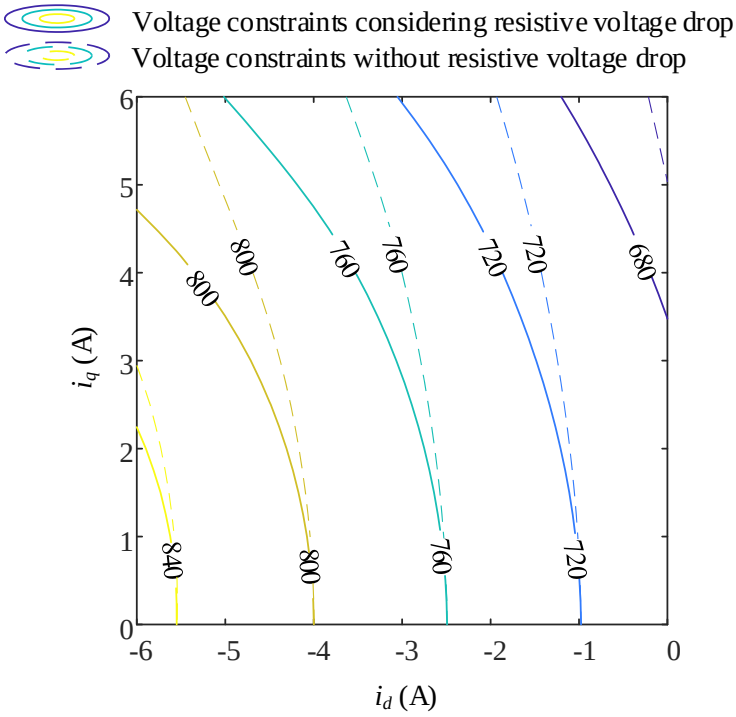

Fig. 4.5 Comparison of the optimal operating region with or without considering the resistive voltage drop.

4.3 Proposed Flux-Weakening Control Strategy

The diagram of the IPMSM control system is shown in Fig. 4.6, which includes the optimal current reference LUTs, the proposed stator flux linkage adjustment (SFLA) method, *dq*-current controller, voltage overmodulation algorithm, voltage source inverter (VSI), and the IPMSM. The optimal current references for the given torque reference T_e^* and the stator flux-linkage reference λ_s^* are output by the optimal current LUTs. The stator flux linkage reference is adjusted by the proposed SFLA method.

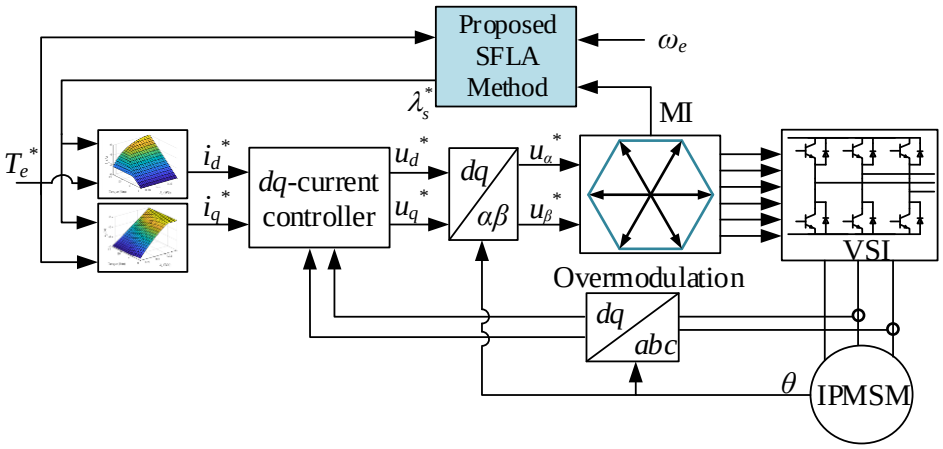

Fig. 4.6 IPMSM control system

The proposed SFLA strategy is shown in Fig. 4.7, which adjusts the stator flux linkage reference based on the input torque reference, speed, and MI. The saturation control protects the current regulation loops from saturation.

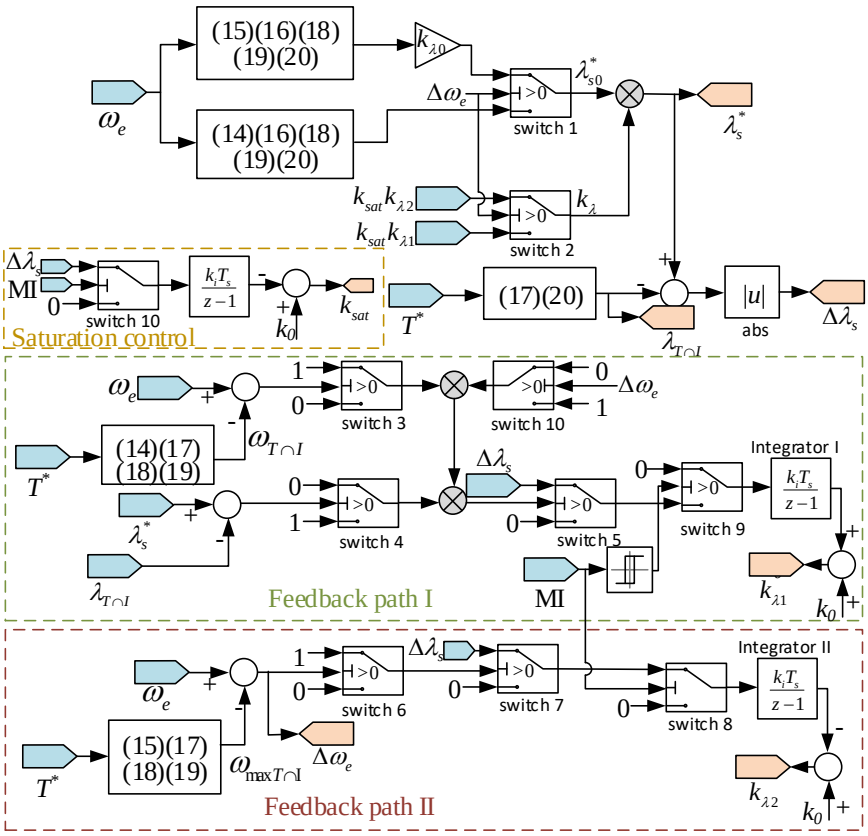

Fig. 4.7 Proposed SFLA strategy.

The maximum voltage of the space vector modulation mode is calculated as

$$V_{s\max} = \frac{1}{\sqrt{3}} V_{dc} \tag{4.14}$$

where V_{dc} is the dc-link voltage.

In this chapter, the overmodulation region is achieved. The maximum voltage of six-step mode is calculated as

$$V_{s\max} = \frac{2}{\pi} V_{dc} \tag{4.15}$$

The intersection of the current constraint and voltage constraint is solved by optimization as

$$\min \ f_1^2 + f_2^2$$
$$s.t. \begin{cases} f_1 = \omega_e^{*2} - \omega_e^2 \\ f_2 = I_{s\max}^2 - i_d^2 - i_q^2 \end{cases} \tag{4.16}$$

The intersection of the current constraint and torque loci is solved as

$$\min \ f_1^2 + f_2^2$$
$$s.t. \begin{cases} f_1 = T_e^* - \dfrac{3}{2} n_p \left\{ \lambda_m i_q + \left[L_d\left(i_d, i_q\right) - L_q\left(i_d, i_q\right) \right] i_d i_q \right\} \\ f_2 = I_{s\max}^2 - i_d^2 - i_q^2 \end{cases} \tag{4.17}$$

The speed on the voltage limit ellipse is calculated based on (4.12) and (4.13) as

$$\omega_e = \frac{-B + \sqrt{B^2 - 4AC}}{2A} \tag{4.18}$$

where *A*, *B*, and *C* are expressed as

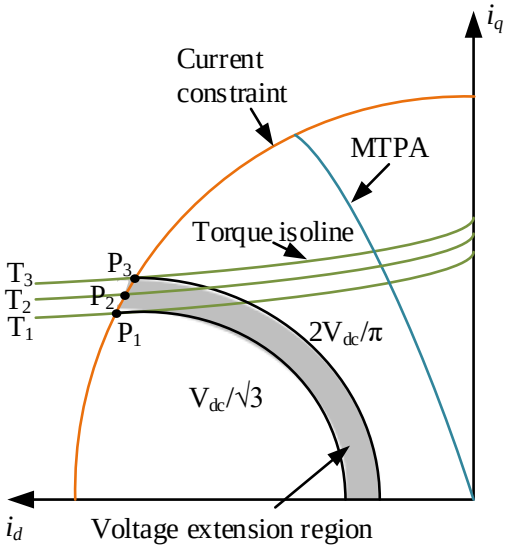

Fig. 4.8 Comparison of the optimal operating point with or without voltage extension.

$$\begin{cases} A = \left[L_d\left(i_d, i_q\right) i_d + \lambda_m \right]^2 + \left[L_q\left(i_d, i_q\right) i_q \right]^2 \\ B = 2R_s \left[L_d\left(i_d, i_q\right) i_d i_q + \lambda_m i_q - L_q\left(i_d, i_q\right) i_q i_d \right] \\ C = R_s^2 i_d^2 + R_s^2 i_q^2 - V_{s\max}^2 \end{cases} \tag{4.19}$$

The stator flux linkage is calculated as

$$\lambda_s = \sqrt{\left[L_d\left(i_d, i_q\right) i_d + \lambda_m \right]^2 + \left[L_q\left(i_d, i_q\right) i_q \right]^2} \tag{4.20}$$

Fig. 4.8 shows the comparison of the optimal operating point with or without voltage extension. The shadow region is the voltage extension region. Conventionally, the maximum voltage ellipse is calculated as $V_{dc}/\sqrt{3}$, and the maximum torque is T_1. However, the dc-link voltage utilization is limited. In this chapter, the stator flux linkage is adjusted in order to produce the maximum and stable torque.

As shown in Fig. 4.8, if the torque command is lower than T_1, the proposed SFLA method doesn't work because $Vdc/\sqrt{3}$ is enough to produce the torque.

If the torque command is larger than T_1 and smaller than T_3 (for example, T_2), the integrator I works. The stator flux linkage reference and the voltage ellipse are increased from point P_1 and expanded to point P_2. At the same time, if the MI is larger than the MI limit, the integrator I is stopped.

If the torque command is larger than T_3, the integrator II works. The stator flux linkage reference is initialized to point P_3, and decreased from point P_3, and the voltage ellipse is shrunk until the MI is inner the MI limit. The stator flux

linkage reference is decreased because the voltage at point P_3 is unachievable due to the voltage saturation.

When the integrator I works, k_λ is expressed as

$$\begin{cases} k_{\lambda 1}(1) = k_0 + k_i \int \Delta\lambda_s(0) \\ k_{\lambda 1}(n+1) = k_{\lambda 1}(n) + k_i \int \Delta\lambda_s(n) \\ k_\lambda(n+1) = k_{\lambda 1}(n+1) \end{cases} \tag{4.21}$$

When the integrator II works, k_λ is expressed as

$$\begin{cases} k_{\lambda 2}(1) = k_0 - k_i \int \Delta\lambda_s(0) \\ k_{\lambda 2}(n+1) = k_{\lambda 2}(n) - k_i \int \Delta\lambda_s(n) \\ k_\lambda(n+1) = k_{\lambda 2}(n+1) \end{cases} \tag{4.22}$$

When the integration is stopped, k_λ is expressed as

$$k_\lambda(n+1) = k_\lambda(n) \tag{4.23}$$

The dynamic stator flux linkage reference and the stator flux linkage difference are calculated as

$$\begin{cases} \lambda_s^*(n+1) = k_\lambda(n+1)\lambda_{s0}^* \\ \Delta\lambda_s(n+1) = \left|\lambda_s^*(n+1) - \lambda_{T\cap I}\right| \end{cases} \tag{4.24}$$

The dynamic MI is calculated as

$$MI(n+1) = \frac{\pi\sqrt{u_d(n+1)^2 + u_q(n+1)^2}}{2V_{dc}} \tag{4.25}$$

The flowchart of the proposed SFLA strategy is shown in Fig. 4.9. The procedure of the proposed SFLA method is explained as follow:

1) Calculate the speed of the intersection point of torque loci and current constraint $\omega_{T\cap I}$ by (4.14)(4.17)(4.18)(4.19). Calculate the maximum speed of the intersection point of torque loci and current constraints $\omega_{\max T\cap \mathrm{I}}$ by (4.15)(4.17)(4.18)(4.19). Compare the instantaneous speed ω_e with $\omega_{\max T\cap \mathrm{I}}$, and $\Delta\omega_e$ is calculated as $\omega_e - \omega_{\max T\cap \mathrm{I}}$.
2) If $\omega_e \le \omega_{\max T\cap \mathrm{I}}$, calculate the initial stator flux linkage reference λ_{s0}^* by (4.14)(4.16)(4.18)(4.19)(4.20). At the same time, if $\omega_e > \omega_{T\cap \mathrm{I}}$, $\lambda_s^* < \lambda_{T\cap I}$ and MI is inner the $\mathrm{MI}_{\mathrm{limit}}$, the integrator I is opened. Else the integrator I is stopped.
3) If $\omega_e > \omega_{\max T\cap \mathrm{I}}$, calculate the initial stator flux linkage reference λ_{s0}^* by (4.15)(4.16)(4.18)(4.19)(4.20). At the same time, if MI> $\mathrm{MI}_{\mathrm{limit}}$, the integrator II is opened. Else the integrator II is stopped.
4) Calculate λ_s^*, $\Delta\lambda_s$ by (4.24). Calculate MI by (4.25).

MI is limited by a hysteresis controller block. The upper limit is near and larger than 1. The lower limit is near and smaller than 1. For example, the upper limit of MI is set to 1.04, and the lower limit is set to 0.94. The limits are adjustable for different speed. The threshold of switch 8 is the same as the upper limit of MI. k_0 is set to 1. k_i is adjustable in this chapter. The dynamic response is faster when k_i is larger.

The proposed SFLA strategy adjusts the stator flux linkage reference based on the region of the speed. When ω_e is not higher than $\omega_{\max T\cap \mathrm{I}}$, the λ_{s0}^* is

calculated by the maximum phase voltage of space vector modulation mode. λ_s^* is increasing from λ_{s0}^* when $\omega_e > \omega_{T\cap I}$, $\lambda_s^* < \lambda_{T\cap I}$ and MI is inner the MI_{limit}. When ω_e is higher than $\omega_{\max T\cap I}$, λ_{s0}^* is calculated by the maximum phase voltage of six-step mode. λ_s^* is reducing from λ_{s0}^* when MI is outer the MI_{limit}.

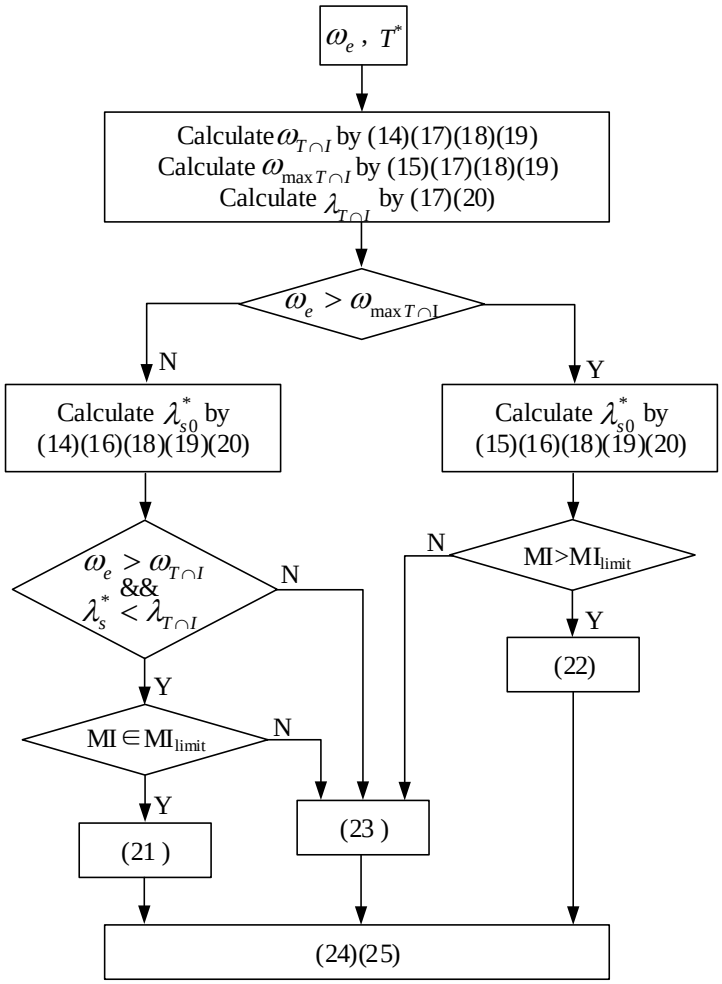

Fig. 4.9 Flowchart of the proposed SFLA strategy.

4.4 Voltage Overmodulation Technique and Optimal Current Reference LUTs

4.4.1 Voltage Overmodulation Technique

The voltage extension region is determined by the time interval of zero space vector T_0. The overmodulation algorithm works when $T_0<0$. If $T_0<0$, $T_1>T_2$ and $T_1>T_s$, T_1 and T_2 are corrected as $T_1'=T_s$ and $T_2'=0$. If $T_0<0$, $T_2>T_1$ and $T_2>T_s$, T_1 and T_2 are corrected as $T_1'=0$ and $T_2'=T_s$. If $T_1 \leqslant T_s$, $T_2 \leqslant T_s$, and $T_0<0$, T_1 and T_2 are corrected as

$$T_1' = \frac{T_1 T_s}{T_1 + T_2}, T_2' = \frac{T_2 T_s}{T_1 + T_2} \tag{4.26}$$

where T_s represents the sampling period. T_1 and T_2 denote the time interval of two active space vectors. The correction of time intervals is shown in Fig. 4.10 and Fig. 4.11. After correction, the operating points which were outside of the hexagon boundary will be on the hexagon boundary. The voltage reference will be in the overmodulation region, as shown in Fig. 4.12.

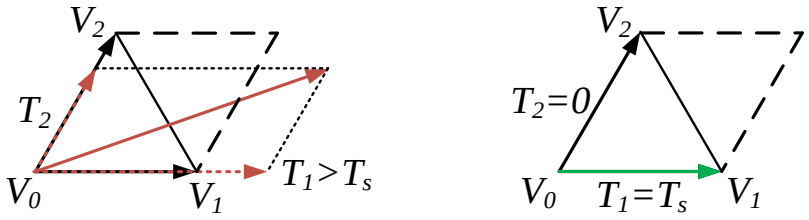

(a) Before correction (b) After correction

Fig. 4.10 Correction of time intervals when $T_0<0$, $T_1>T_2$ and $T_1>T_s$.

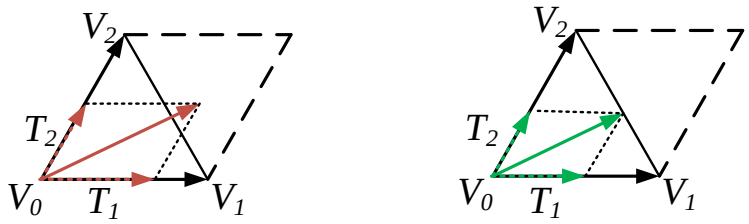

(a) Before correction (b) After correction

Fig. 4.11 Correction of time intervals when $T_1 \leqslant T_s$, $T_2 \leqslant T_s$, and $T_0<0$.

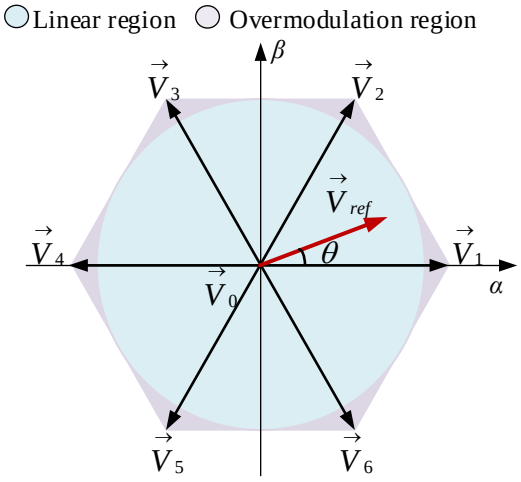

Fig. 4.12 Liner region and overmodulation region.

In the voltage extension region, the voltage reference is no more circular, which is shown as partial circular, and partial on the hexagon boundary. The voltage hexagon boundary is a rotating hexagon in the synchronous rotating reference frame, which rotates with the motor speed ω_e, as shown in Fig. 4.13. Fig. 4.14 shows the optimal operating regions by maximum voltage of linear region and by maximum voltage of overmodulation region.

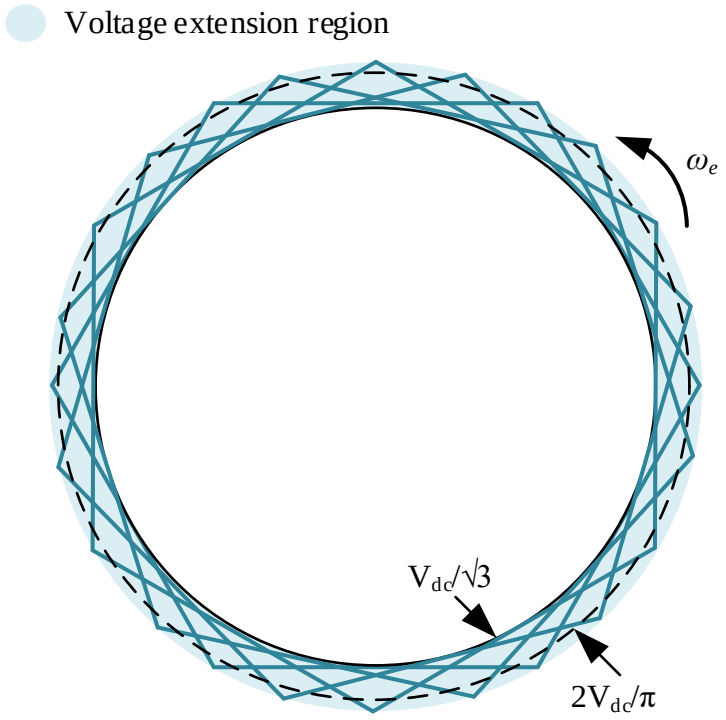

Fig. 4.13 Voltage extension region.

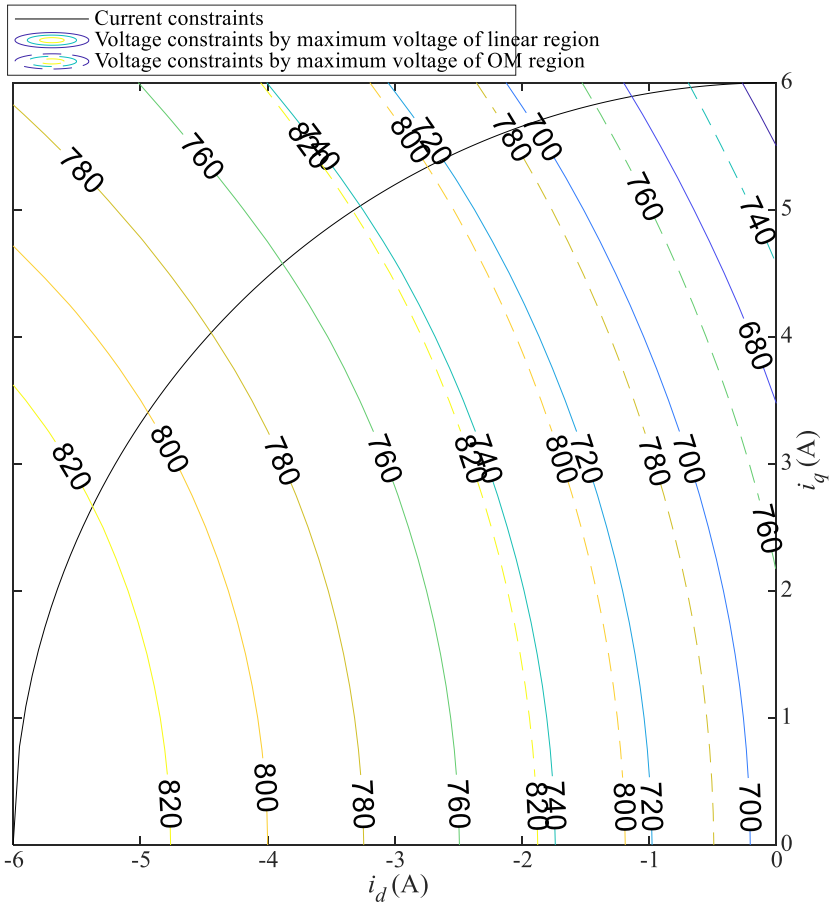

Fig. 4.14 Optimal operating regions by maximum voltage of linear region and by maximum voltage of overmodulation region.

4.4.2 Optimal Current Reference LUTs

The feedforward optimal current reference LUTs in the entire torque and speed range shown in Fig. 4.15 are solved as the intersections of the MTPA trajectory, voltage constraint, current constraint, and torque loci presented in Chapter 2 in different speed and torque regions. The nonlinear inductances are used to obtain the optimal current LUTs.

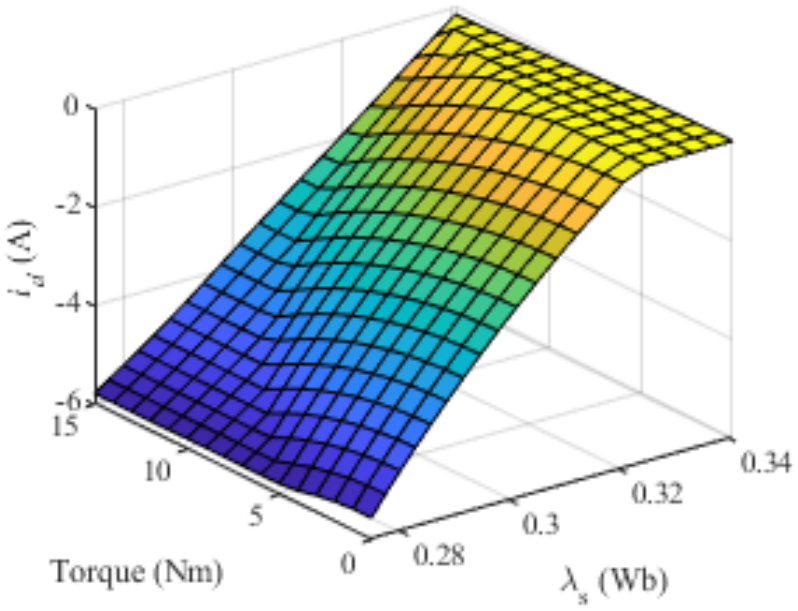

(a)

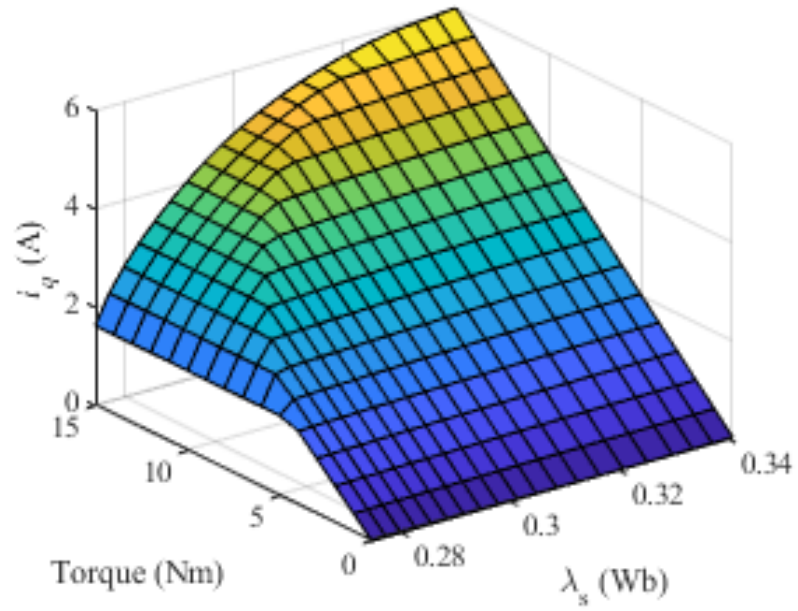

(b)

Fig. 4.15 Optimal current references corresponding to torque and λ_s.

4.5 Comparison Between the Proposed FWC Method and Existing FWC Techniques

4.5.1 Comparison Between FF-based Flux-Weakening Methods and the Proposed Method

Table 4.1 shows the details of the IPMSM drive system. The switching frequency is 10kHz. The speed is set as a constant value, and the torque command is set as a step command. The IPMSM drive system is simulated as the condition that the IPMSM is coupled with a dyno motor. The dyno motor is operated under speed control mode, and the IPMSM is operated under torque control mode.

In the FF-based flux-weakening methods, the operating point depends entirely on the feedforward path. The stator flux linkage reference is constant without adjustment. Fig. 4.16 shows the torque and currents of the conventional FF-based method at 740 r/min, with a step torque command changed from 1Nm to 14Nm. The torque of the conventional method cannot track the torque command, as shown in Fig. 4.16. Fig. 4.17 shows the torque and currents of the proposed method with the same operation condition of Fig. 4.16. Fig. 4.17 shows the torque precisely tracks the torque reference. This is because the proposed method has a higher voltage utilization rate. In the proposed method, when the torque command is higher than the torque calculated by the maximum phase voltage of SVM, the proposed SFLA method starts to work. The stator flux linkage reference is increased to improve the torque until the torque can track the torque command.

Fig. 4.19 shows the torque and currents of the conventional method at 820 r/min, with a torque step command changed from 1Nm to 14Nm. Fig. 4.20 shows the torque and currents of the proposed method with the same operation condition of Fig. 4.19. The torque in Fig. 4.19 and Fig. 4.20 cannot track the torque command. This is because the torque command is extremely high, which cannot be tracked even the six-step mode is achieved. However, the torque of the proposed method is still increased about 10% compared with the conventional FF-based flux-weakening methods method. Fig. 4.18 and Fig. 4.21 shown the voltage trajectory of the proposed method is extended to the voltage extension region.

Table 4.1 Details of the IPMSM Drive System

Details	Value
DC-Link voltage	210 V
Current limit	6 A
Number of pole pairs	5
PM flux linkage	333.3 mWb
Base speed	658 r/min
Maximum torque	15 Nm
Stator resistance	400 mΩ

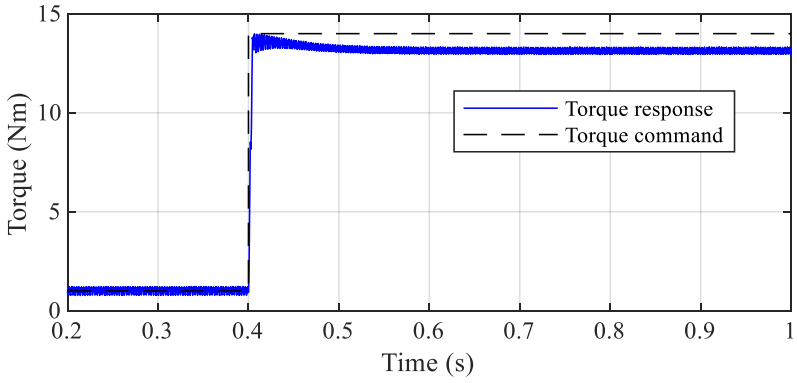

(a)

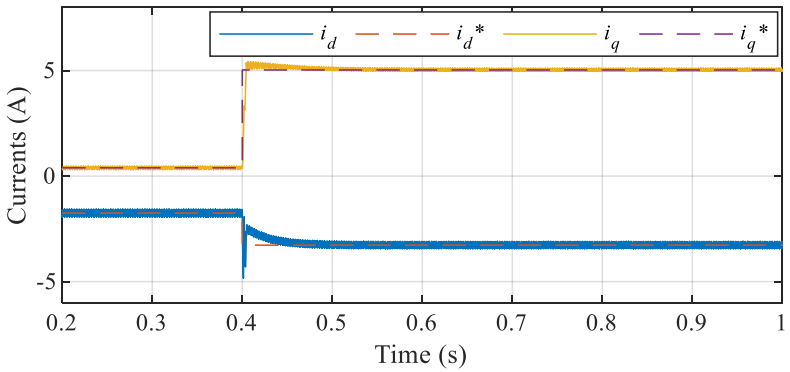

(b)

Fig. 4.16 Simulation results of FF-based flux-weakening control at 740 r/min. (a) Torque. (b) Currents.

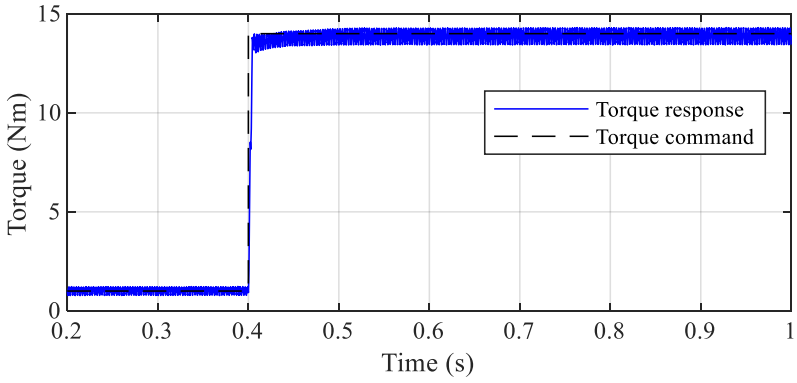

(a)

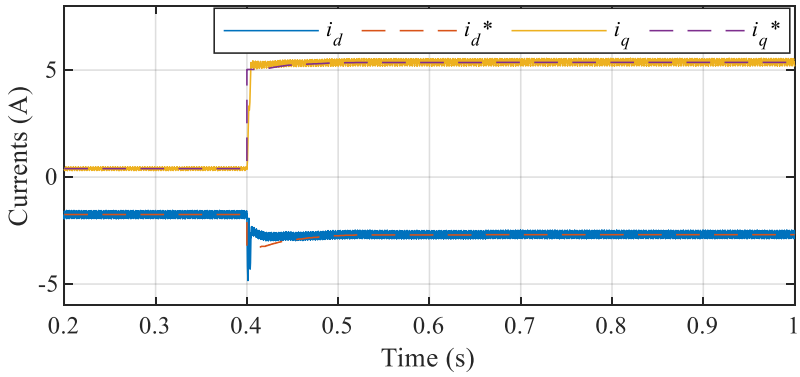

(b)

Fig. 4.17 Simulation results of proposed method at 740 r/min. (a) Torque. (b) Currents.

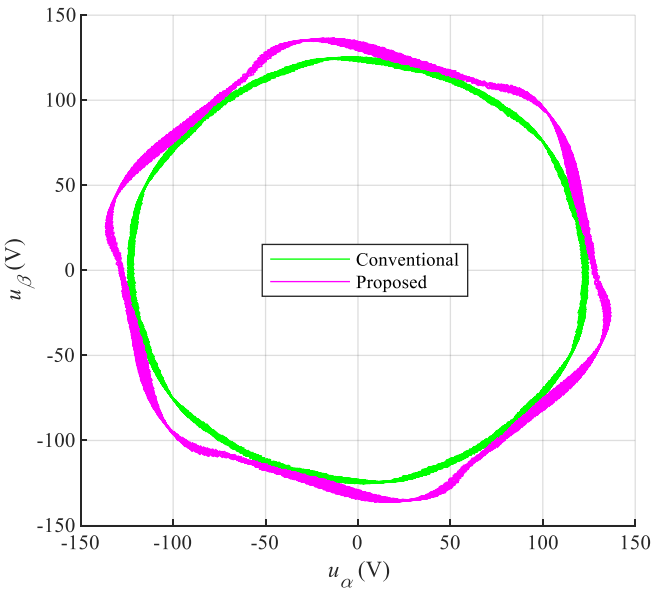

Fig. 4.18 Voltage trajectory of the conventional method and the proposed method at 740 r/min.

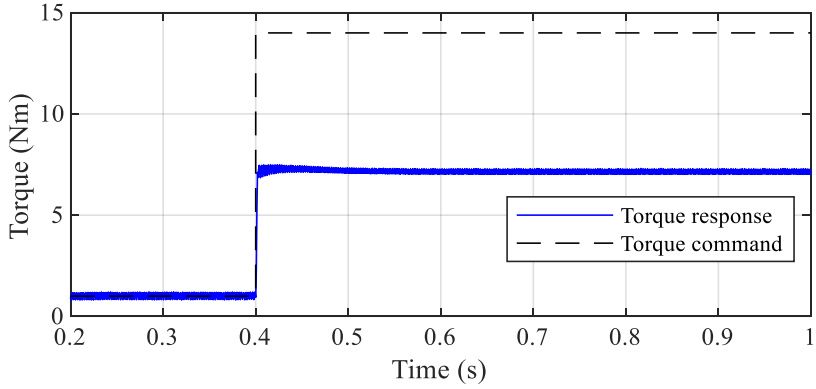

(a)

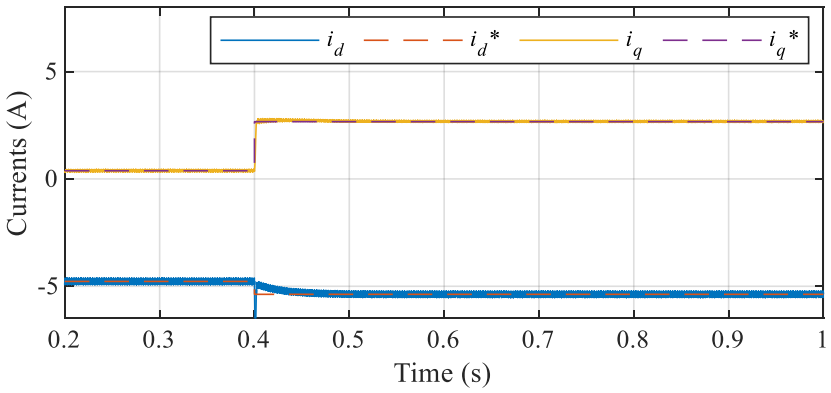

(b)

Fig. 4.19 Simulation results of FF-based flux-weakening control at 820 r/min. (a) Torque. (b) Currents.

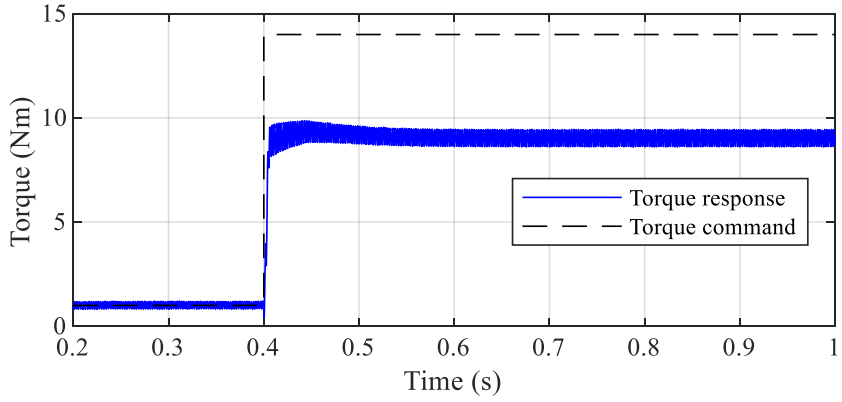

(a)

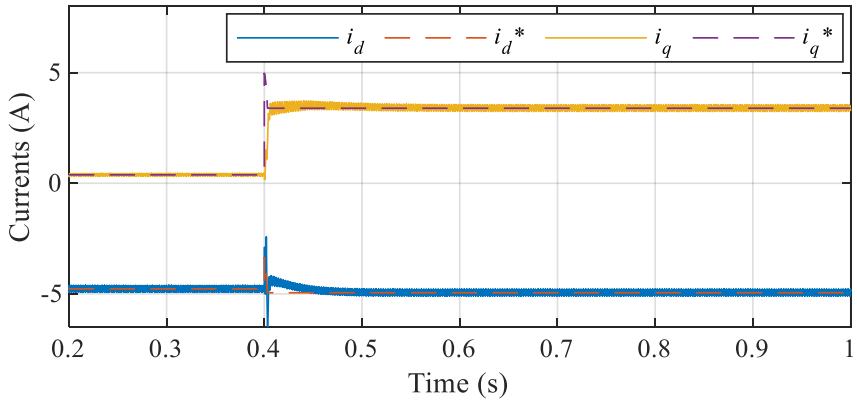

(b)

Fig. 4.20 Simulation results of proposed method at 820 r/min. (a) Torque. (b) Currents.

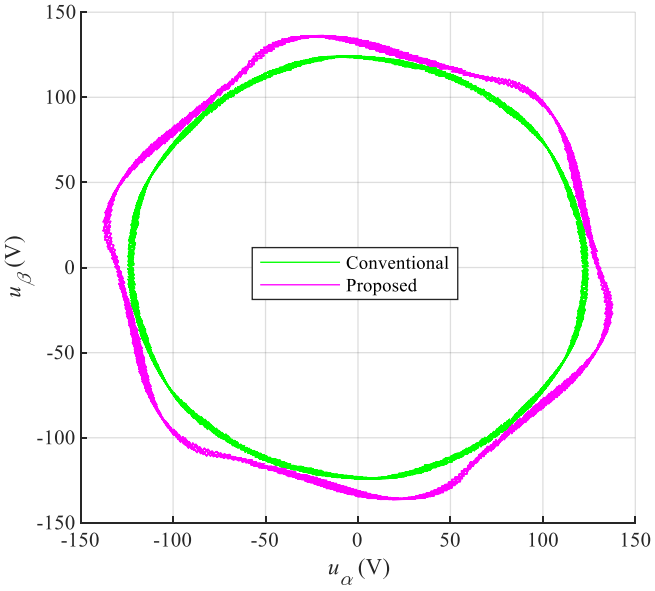

Fig. 4.21 Voltage trajectory of the conventional method and the proposed method at 820 r/min.

Torque response when motor parameter errors are introduced at 740 r/min:

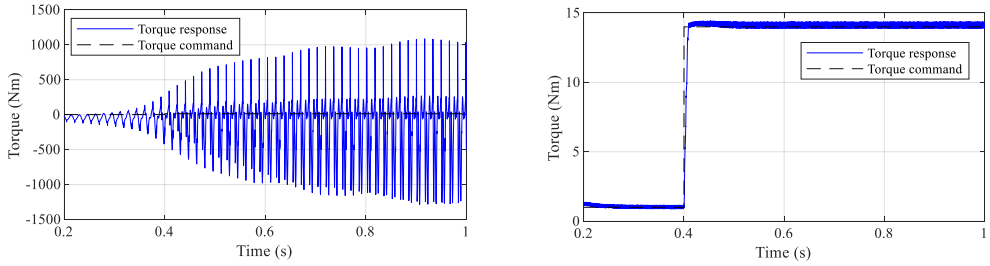

(a) FF-based (b) Proposed method

It can be seen that when motor parameter errors are introduced, the PI regulation loops are saturated in FF-based method, and the torque is unstable. In the proposed method, the modulation index as well as the voltage saturation is controlled, which provides better robustness to motor parameters variation.

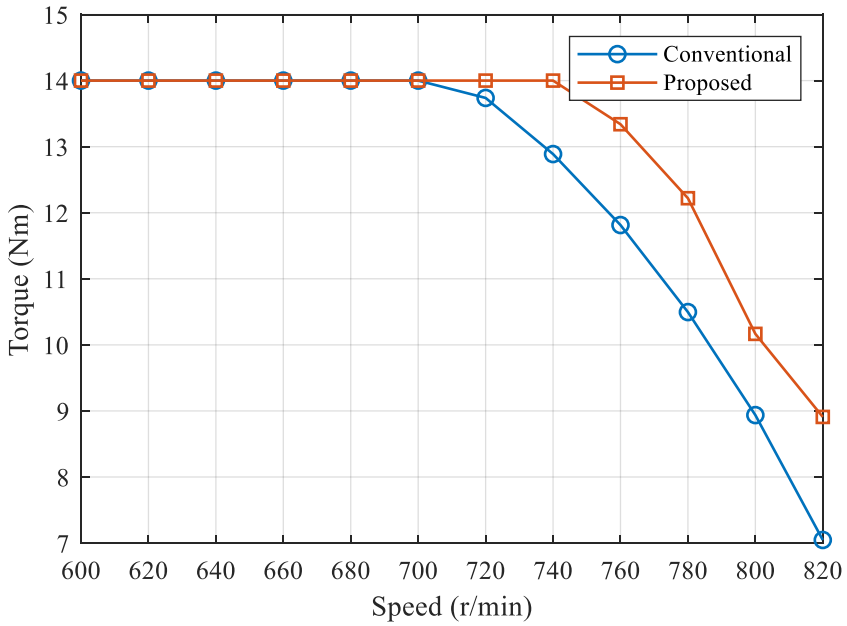

(a)

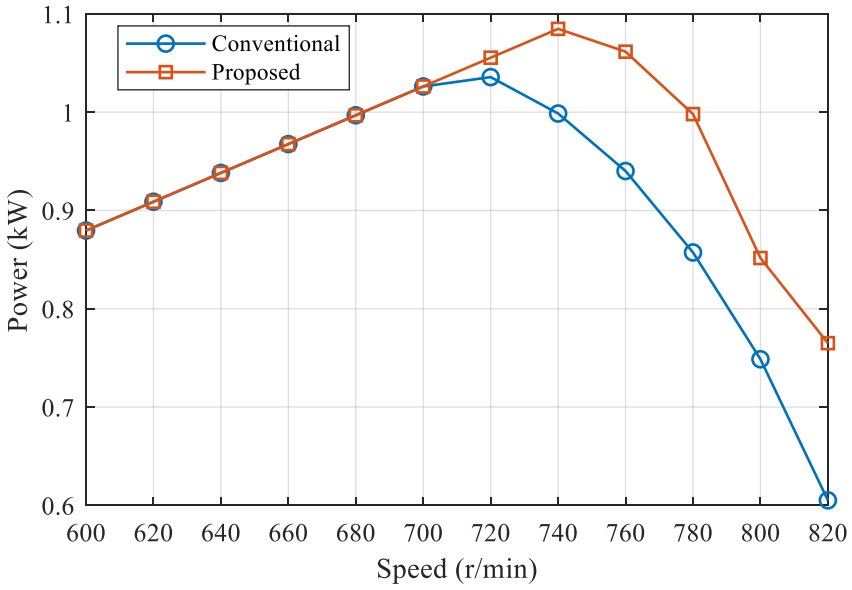

(b)

Fig. 4.22 Comparison between FF-based FWC and the proposed method. (a) Torque versus speed. (b) Power versus speed

Fig. 4.22 shows the comparison of the torque and power at different speeds when the torque reference is 14Nm. The speed range of the constant torque part of the proposed method is extended. In the current constraint region, the torque of the proposed method is improved compared to the conventional method.

4.5.2 Comparison Between FB-based Flux-Weakening Methods and the Proposed Method

Fig. 4.23 shows the torque and currents of FB-based flux-weakening control at 740 r/min. Fig. 4.24 shows the torque and currents of FB-based flux-weakening control at 740 r/min. The torque ripple and current ripple are larger in Fig. 4.23 during the transient process. This is because the voltage is keeping saturated in the transient process, and the voltage is distorted by induced low-order harmonics. In FB-based FW control, the operating point moves from MTPA to the flux-weakening region until the voltage is no more saturated. Before the operating point reaches the appropriate point, the voltage is keeping saturated, which not only degrades the dynamic response but also puts the drive system into a harsh condition.

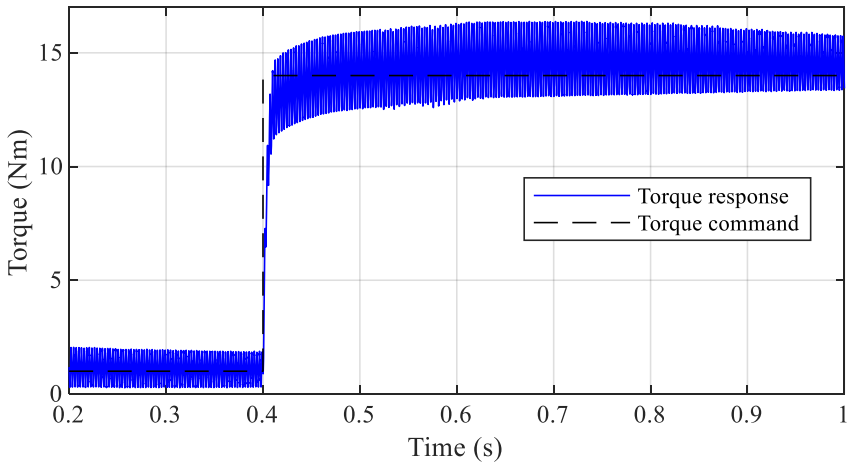

(a)

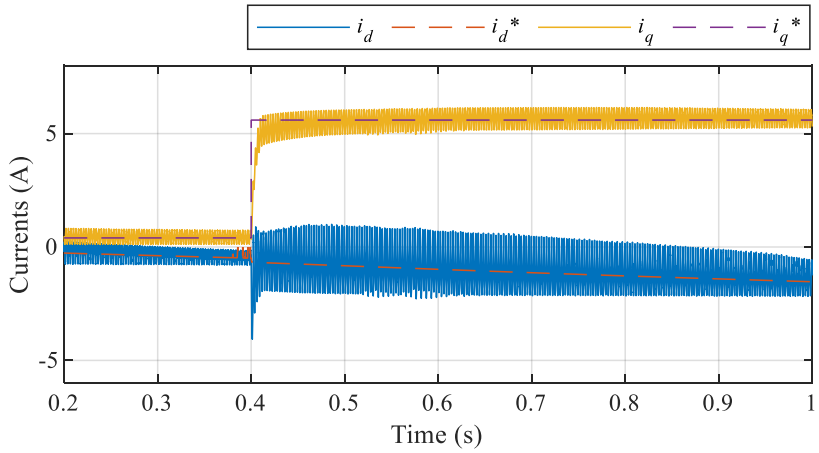

(b)

Fig. 4.23 Simulation results of FB-based flux-weakening control at 740 r/min. (a) Torque. (b) Currents.

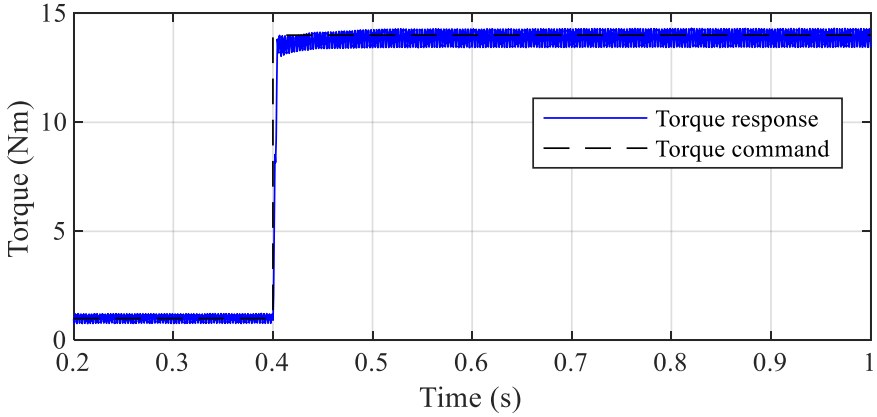

(a)

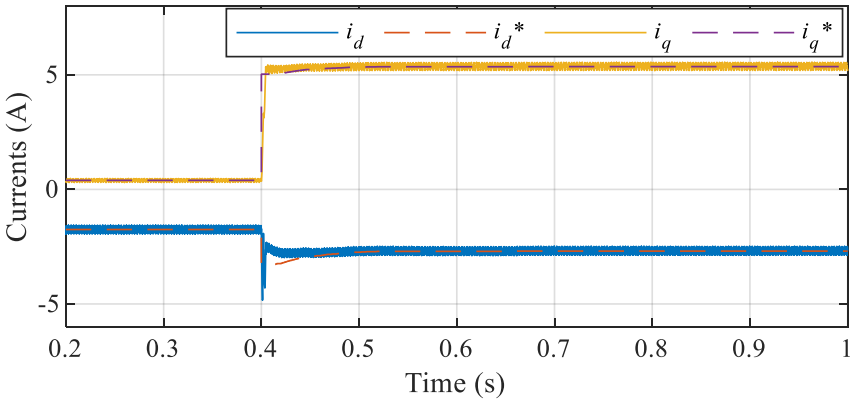

(b)

Fig. 4.24 Simulation results of proposed method at 740 r/min. (a) Torque. (b) Currents.

4.5.3 Comparison Between Mixed Flux-Weakening Methods with One Feedback Path and the Proposed Method

Fig. 4.25 shows the torque and currents if there is only one increasing feedback path with the same operation condition of Fig. 4.20 and Fig. 4.26. Although the torque in Fig. 4.25 can be achieved as the same value as the proposed

method, the dynamic response is slow, and the torque keeps slowly increasing and is stable after 1s. The torque of the proposed method is stable after 0.6s. This is because the proposed SFLA method has higher initial stator flux linkage reference and voltage reference, which provides a higher dynamic response speed.

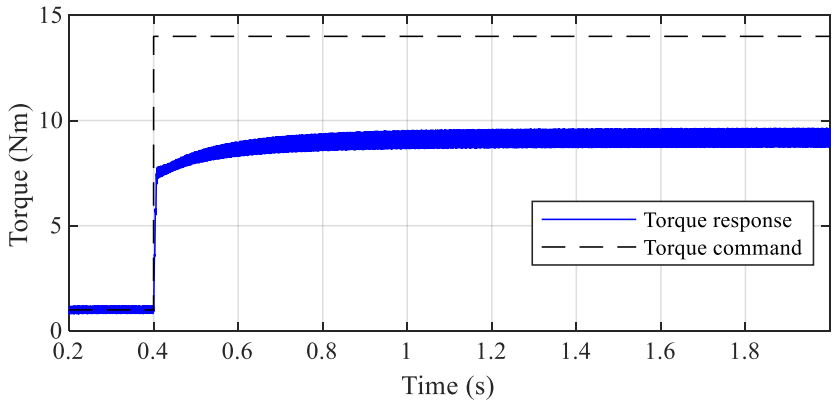

(a)

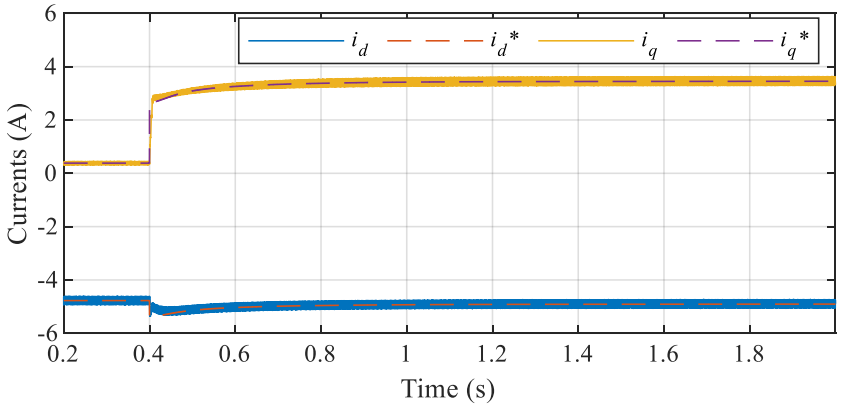

(b)

Fig. 4.25 Mixed FWC with only increasing feedback path at 820 r/min. (a) Torque. (b) Currents.

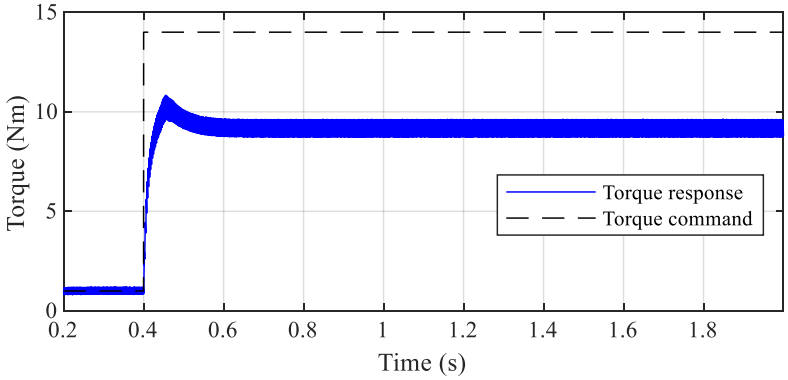

(a)

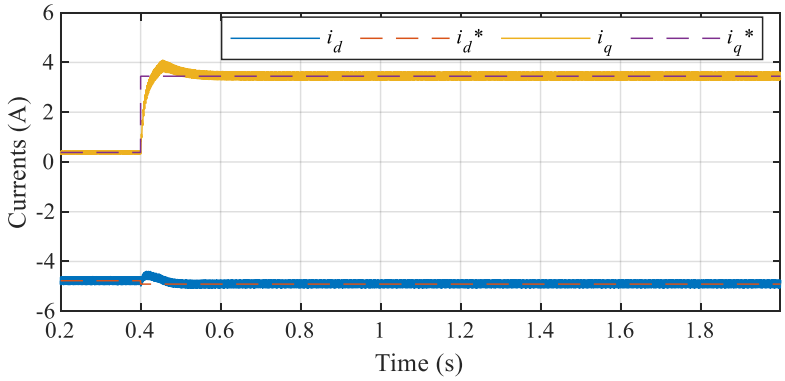

(b)

Fig. 4.26 The proposed method at 820r/min. (a) Torque. (b) Currents.

4.5.4 Comparison Between Considering and Ignoring Resistive Voltage Drop

Fig. 4.27 shows the comparison between considering and ignoring resistive voltage drop. The operating speed is 740 r/min, and the torque command is 12 Nm. Fig. 4.27(a) shows the higher torque ripple of torque ignoring the resistive voltage drop. Also, the *d*-axis and *q*-axis current ripples are larger, as shown in Fig. 4.27(b). The control error occurs, and the control performance is degraded without considering the resistive voltage drop. The reason is that the voltage ellipses formed by considering the resistive voltage drop are slant. When ignoring the resistive voltage drop, the operating point is calculated by a larger phase voltage. However, this larger phase voltage doesn't contribute to the torque. The larger phase voltage results in the higher torque ripple Due to the existence of the resistive voltage drop, when the dc-link voltage is not enough to generate this higher operating point, the tracking error would occur on the i_d and i_q

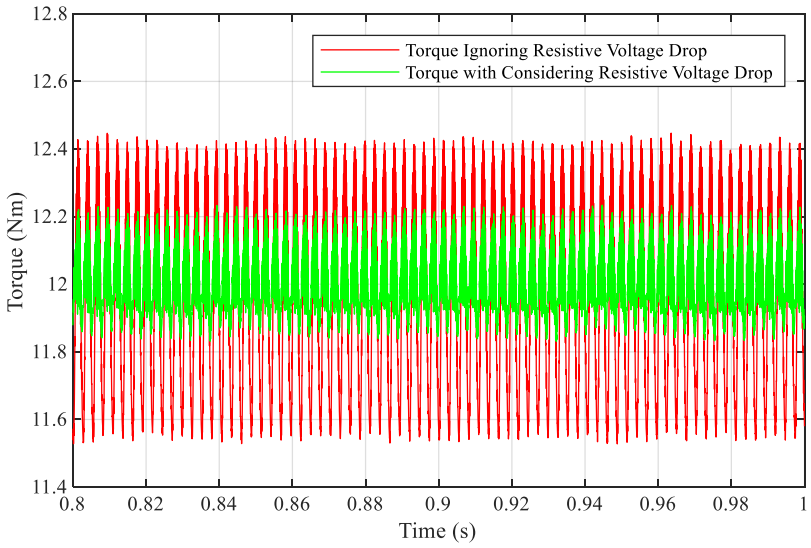

(a)

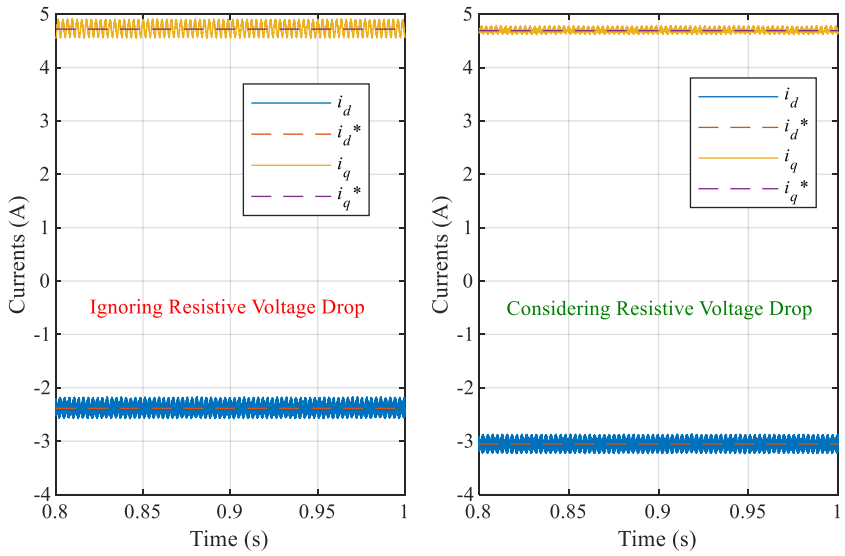

(b)

Fig. 4.27 Comparison between Considering Resistive Voltage Drop and Ignoring Resistive Voltage Drop. (a) Torque. (b) Currents.

4.6 Conclusion

A SFLA flux-weakening control method is proposed. The stator flux linkage reference is adjusted based on the torque, speed, and modulation index. Two voltage feedback paths are provided in the proposed SFLW-FW method. The feedback path is chosen based on the torque reference and operating speed. The resistive voltage drop and magnetic saturation are considered. Compared to the FF-based flux-weakening methods, the proposed method improves the torque and power. Compared to the FB-based flux-weakening methods, the proposed method improves the dynamic performance, and avoids the voltage saturation and windup problem, and improves the stability of the IPMSM drive system. Compared to the flux-weakening methods which only have one feedback path, the proposed method

improves the dynamic performance. Compared to the flux-weakening methods which do not consider the resistive voltage drop, the proposed method avoids the control error caused by parameter mismatch.

Chapter 5
Influence Analysis of Extended DC-Link Voltage Utilization

5.1 Windup Analysis

As shown in Fig. 5.1, in the shaded region, the voltage reference is smaller than the phase voltage magnitude of hexagon boundary. However, the voltage reference is larger than the maximum modulation output, which cannot realize by SVM-based inverter. In the shaded region and the region where the voltage is larger than the shaded region, the current regulation loops would have no response, which is called the windup phenomenon. Windup can degrade the dynamic performance of IPMSM drive systems, which is a problem in the voltage extension region. In general, the flux-weakening method can be regarded as a part of antiwindup control. In IPMSM drive systems, the current regulation output limit and inverter output limit can cause the windup problem. The windup phenomenon would happen when the voltage is over the inverter output limit. The voltage limit entirely depends on the current regulation output limit when windup happens. Antiwindup techniques

can avoid the windup of current regulation loops. It should be noticed that the voltage constraint of flux-weakening control and voltage saturation boundary of PI antiwindup control should be consistent to avoid putting the IPMSM control systems into a double squeeze.

To avoid the windup problem, the modulation index (MI) is controlled in the proposed flux-weakening methods in Chapter 3 and Chapter 4. In this chapter, the torque, torque ripple, current ripple, and harmonics are analyzed in voltage extension region, to carry out the influence of extended dc-link voltage on the torque and torque ripple.

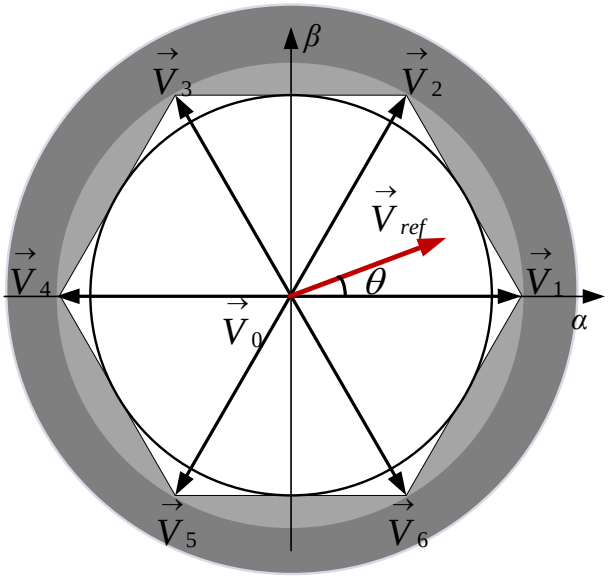

Fig. 5.1 Voltage saturation region

5.2 Mathematical Analysis of the Relationship Between Torque and Voltage

As analyzed in previous chapters, the torque is increased with the extension of voltage utilization. In this section, the mathematical expression of the relationship between the torque and voltage is derived. The torque is expressed as

$$T_e^* = \max\left\{\frac{3}{2}n_p\left[\lambda_m i_q + \left(L_d - L_q\right)i_d i_q\right]\right\}$$
$$s.t.\begin{cases} u_d^2 + u_q^2 \le V_{s\max}^2 \\ i_d^2 + i_q^2 \le I_{s\max}^2 \end{cases} \tag{5.1}$$

In the voltage extension region, the voltage reference is no more circular; the voltage boundary is shown in Fig. 5.2. The voltage boundary is a hexagon, which rotates with the motor speed ω_e in the synchronous rotating reference frame.

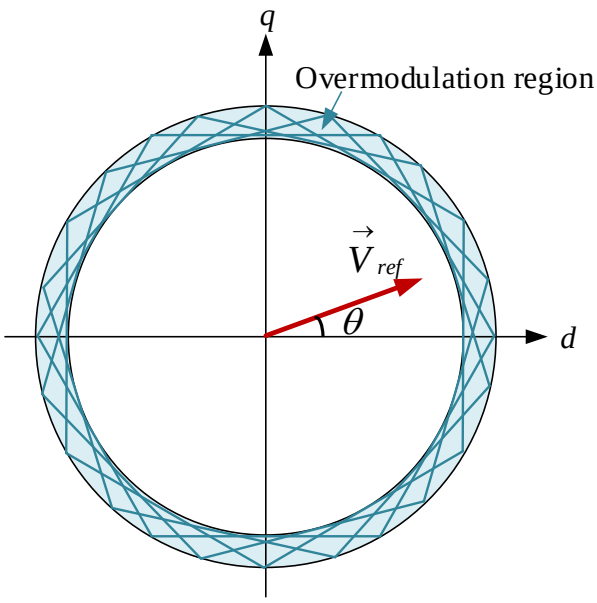

Fig. 5.2 Voltage boundary in the voltage extension region

When the dwell time of zero vector T_0 equals zero, the voltage reference is on the hexagon boundary, which is derived as follows.

When T_0 =0, $T_a + T_b = T_s$. It can be known that

$$\begin{cases} T_a = T_s - T_b \\ T_b = T_s - T_a \end{cases} \tag{5.2}$$

The voltage reference is solved as

$$\begin{aligned} \vec{V}_{ref} &= \frac{T_a}{T_s}\vec{V}_1 + \frac{T_b}{T_s}\vec{V}_2 + \frac{T_0}{T_s}\vec{V}_0 \\ &= \frac{T_a}{T_s}\vec{V}_1 + \frac{T_s - T_a}{T_s}\vec{V}_2 \\ &= \vec{V}_2 + \frac{T_a}{T_s}\left(\vec{V}_1 - \vec{V}_2\right) \end{aligned} \tag{5.3}$$

$$\begin{aligned} \vec{V}_{ref} &= \frac{T_a}{T_s}\vec{V}_1 + \frac{T_b}{T_s}\vec{V}_2 + \frac{T_0}{T_s}\vec{V}_0 \\ &= \frac{T_s - T_b}{T_s}\vec{V}_1 + \frac{T_b}{T_s}\vec{V}_2 \\ &= \vec{V}_1 + \frac{T_b}{T_s}\left(\vec{V}_2 - \vec{V}_1\right) \end{aligned} \tag{5.4}$$

To analyze the influence of extended dc-link voltage utilization on torque, the relationship between torque and voltage is derived as follows.

The voltage equations are expressed as

$$\begin{cases} u_d = -\omega_e L_q i_q + R_s i_d \\ u_q = \omega_e (L_d i_d + \lambda_m) + R_s i_q \end{cases} \tag{5.5}$$

The torque equation is written as

$$T_e = \frac{3}{2} n_p \left[\lambda_m i_q + \left(L_d - L_q\right) i_d i_q \right] \tag{5.6}$$

The *d*-axis and *q*-axis currents are solved by (5.5) as

$$\begin{vmatrix} i_d \\ i_q \end{vmatrix} = \frac{1}{R_s^2 + \omega_e^2 L_d L_q} \begin{vmatrix} R_s u_d + \omega_e L_q \left(u_q - \omega_e \lambda_m \right) \\ -\omega_e L_d u_d + R_s \left(u_q - \omega_e \lambda_m \right) \end{vmatrix} \tag{5.7}$$

Combine (5.6) with (5.7), the relationship between torque and voltage is solved as

$$T_e = \frac{3}{2} n_p \begin{bmatrix} \left(L_d - L_q \right) \dfrac{\left(R_s u_d + \omega_e L_q u_q - \omega_e^2 L_q \lambda_m \right)\left(R_s u_q - \omega_e L_d u_d - R_s \omega_e \lambda_m \right)}{\left(R_s^2 + \omega_e^2 L_d L_q \right)^2} \\ + \left(L_d - L_q \right) \dfrac{\lambda_m \left(R_s u_q - \omega_e L_d u_d - R_s \omega_e \lambda_m \right)}{\left(R_s^2 + \omega_e^2 L_d L_q \right)} \end{bmatrix} \tag{5.8}$$

where the variable parameters are the speed, *m*, u_d, and u_q.

By inversion (5.8), u_d and u_q can be written as the functions of torque and speed. Then in the IPMSM drive systems, the u_d and u_q can be calculated directly by torque and speed. The IPMSM drive systems without current regulation loops are studied and called current sensorless control in [55] and [56].

Based on derivations, the current constraint, voltage constraints, and torque loci can be drawn in the u_d - u_q plane, as shown in Fig. 5.4. The larger dashed circle is 2 V_{dc} /3. The smaller dashed circle is 2 V_{dc} / π, which is the magnitude of the fundamental component of phase voltage at six-step mode.

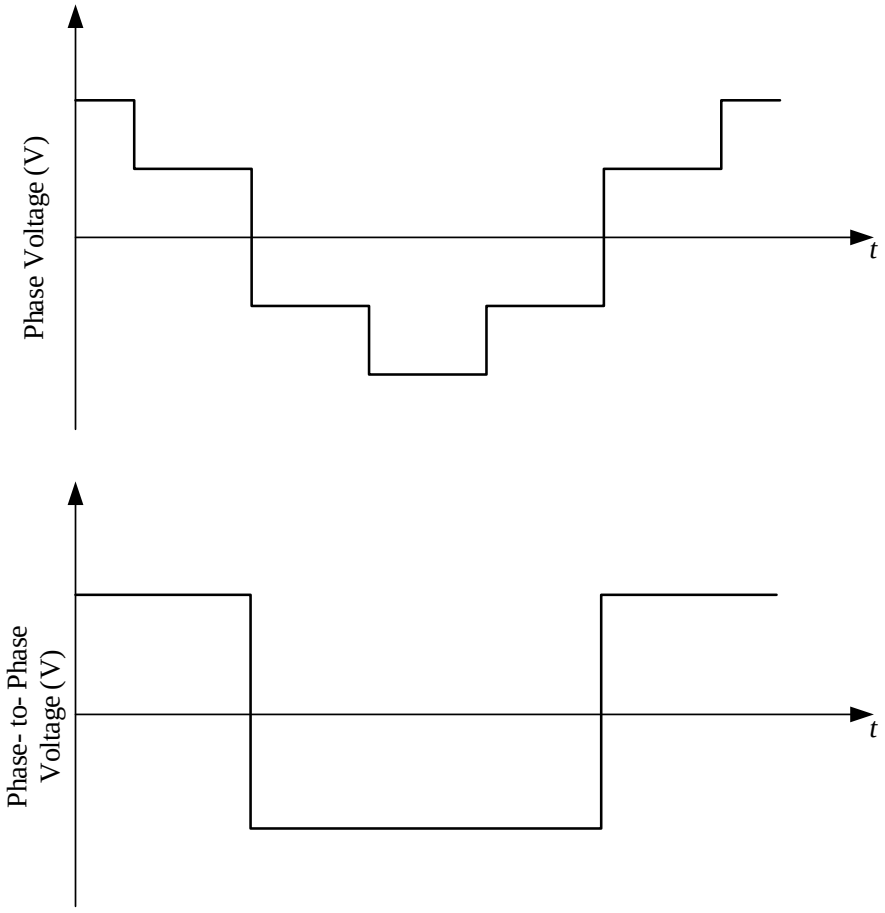

Fig. 5.3 Six-step mode

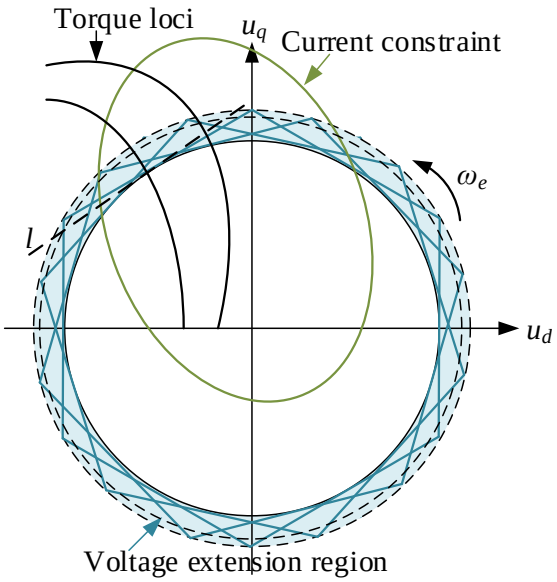

Fig. 5.4 Current constraint, voltage constraints and torque loci in u_d - u_q plane

In (5.8), the torque is expressed by u_d and u_q. To solve the relationship between the torque and dc-link voltage, u_d and u_q should be replaced by V_{dc}, which is calculated as

$$\begin{cases} i_d^2 + i_q^2 \le I_s^2 \\ u_d^2 + u_q^2 \le m^2 V_{dc}^2, MI = \dfrac{\pi}{2} m \end{cases} \tag{5.9}$$

where m is related to modulation strategies, and I_s is the maximum phase current. u_d and u_q are solved as

$$u_q = \frac{L_d \left(\left(-I_s^2 L_d^2 L_q^2 \omega_e^2 + I_s^2 L_q^4 \omega_e^2 + L_d^2 m^2 V_{dc}^2 - L_q^2 m^2 V_{dc}^2 + L_q^2 \omega_e^2 \lambda_m^2 \right)^{\frac{1}{2}} - L_q^2 \lambda_m \omega_e \right)}{\left(L_d - L_q \right) \left(L_d + L_q \right)} \tag{5.10}$$

$$u_d = \frac{-L_q\left(-m^2V_{dc}^2+\lambda_m^2\omega_e^2-I_s^2L_d^2\omega_e^2-\frac{2\lambda_m\omega_e\left(-I_s^2L_d^2L_q^2\omega_e^2+I_s^2L_q^4\omega_e^2+L_d^2m^2V_{dc}^2-L_q^2m^2V_{dc}^2+L_q^2\omega_e^2\lambda_m^2\right)^{\frac{1}{2}}-L_q^2\lambda_m\omega_e}{\left(L_d-L_q\right)\left(L_d+L_q\right)}\right)^{\frac{1}{2}}}{\left(L_d-L_q\right)\left(L_d+L_q\right)}$$

(5.11)

The relationship between torque and dc-link voltage or modulation index can be solved by combining (5.8), (5.10), and (5.11).

The tangent *l* on the inscribed circle in Fig. 5.4 is defined as

$$u_q = -\frac{\cos\theta}{\sin\theta}u_d + \frac{V_{dc}}{\sqrt{3}\sin\theta} \tag{5.12}$$

The torque on the tangent *l* is calculated as

$$T_e = \frac{3}{2}n_p\left[\frac{\left(L_d-L_q\right)}{\left(R_s^2+\omega_e^2L_dL_q\right)^2}\left(a_Tu_d^2+b_Tu_d+c_T\right)\right] \tag{5.13}$$

where

$$\begin{aligned}
a_T &= \left(R_s-\frac{\cos\theta}{\sin\theta}\omega_eL_q\right)\left(-\frac{\cos\theta}{\sin\theta}R_s-\omega_eL_d\right)\\
b_T &= \left(R_s-\frac{\cos\theta}{\sin\theta}\omega_eL_q\right)\left(\frac{V_{dc}}{\sqrt{3}\sin\theta}R_s-R_s\omega_e\lambda_m\right)\\
&\quad+\left(-\frac{\cos\theta}{\sin\theta}R_s-\omega_eL_d\right)\left(\frac{V_{dc}}{\sqrt{3}\sin\theta}\omega_eL_q-\omega_e^2L_q\lambda_m+\lambda_m\left(R_s^2+\omega_e^2L_dL_q\right)\right)\\
c_T &= \left(\frac{V_{dc}}{\sqrt{3}\sin\theta}\omega_eL_q-\omega_e^2L_q\lambda_m+\lambda_m\left(R_s^2+\omega_e^2L_dL_q\right)\right)\left(\frac{V_{dc}}{\sqrt{3}\sin\theta}R_s-R_s\omega_e\lambda_m\right)
\end{aligned}$$

(5.14)

5.3 Torque and Torque Ripple Analysis

The torque ripple is expressed as

$$T_r = \frac{T_{\max} - T_{\min}}{T_{avg}} \tag{5.15}$$

The standard deviation (STD) of torque measures the amount of torque variation, which indicates how close the instantaneous torque to the average torque. A lower torque STD means the torque is closer to the average torque. The torque STD is calculated as

$$Torque\ STD = \sqrt{\frac{1}{n-1}\sum_{i=1}^{n}\left(T_i - T_{avg}\right)^2} \tag{5.16}$$

The standard deviation of current is calculated as

$$Current\ STD = \sqrt{\frac{1}{n-1}\sum_{i=1}^{n}\left(I_i - I_{avg}\right)^2} \tag{5.17}$$

5.3.1 Torque and Torque Ripple Analysis for the Proposed Flux-Weakening Method with Constant Parameters

The results of torque, torque ripple, and current STD with the increase of MI at 1400 r/min are shown in Fig. 5.5 - Fig. 5.10 The torque is increased with the increase of MI, which reaches the same conclusion as the mathematical analysis of the relationship between the voltage and torque in 5.2. At the same time, the current STD and torque ripple are also increased with the increase of MI.

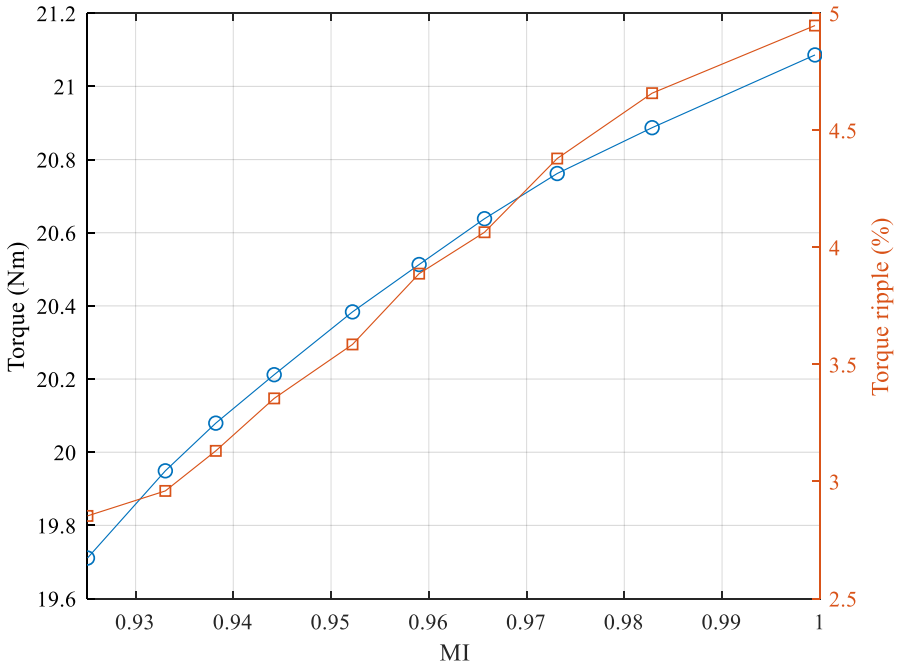

Fig. 5.5 Torque and torque ripple at different MI

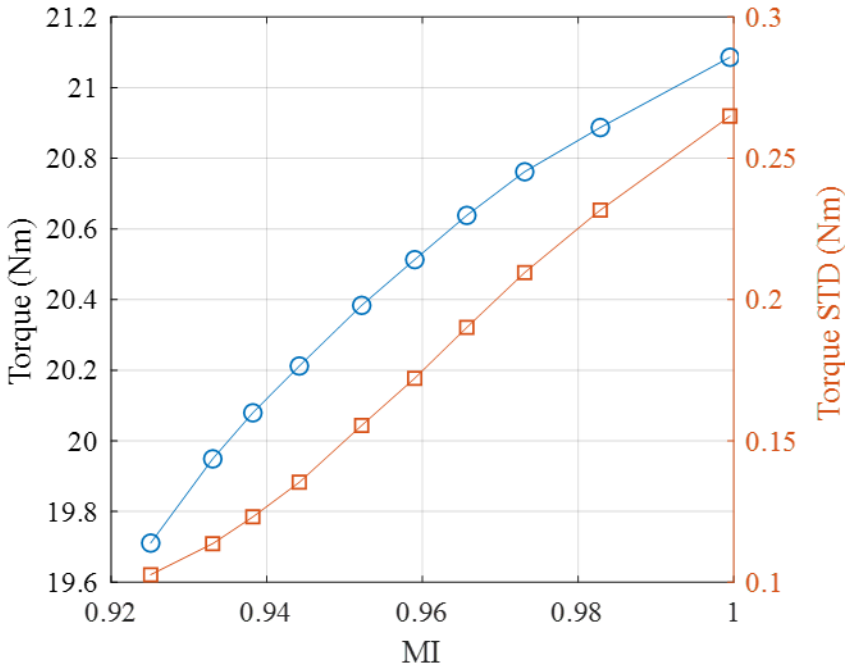

Fig. 5.6 Torque and torque STD at different MI

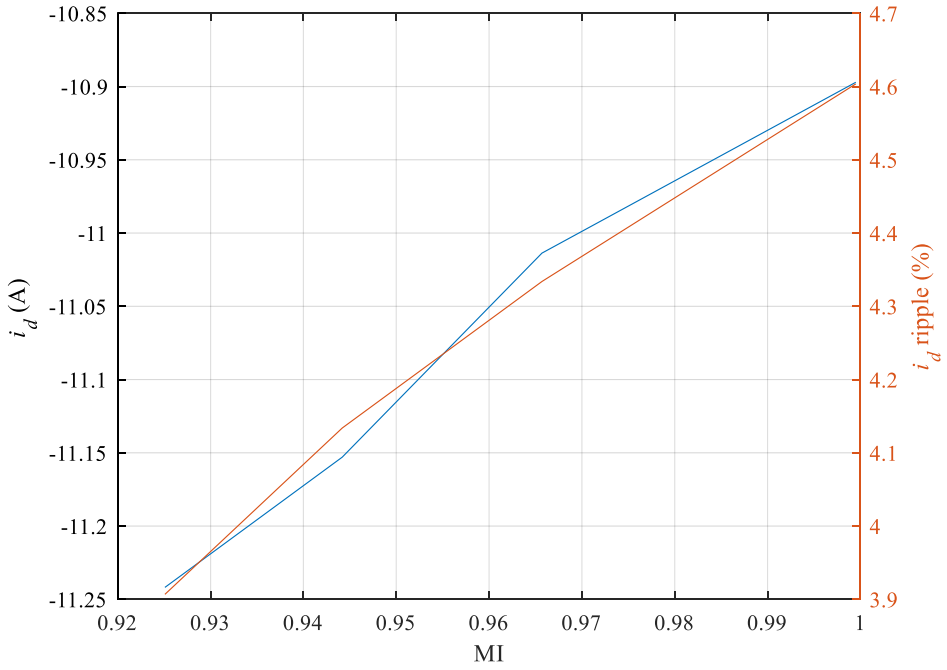

Fig. 5.7 i_d and i_d ripple at different MI

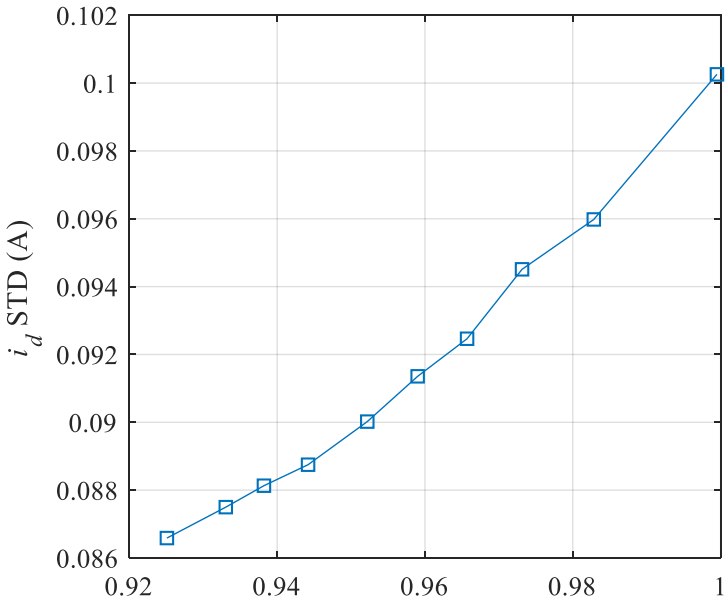

Fig. 5.8 i_d STD at different MI

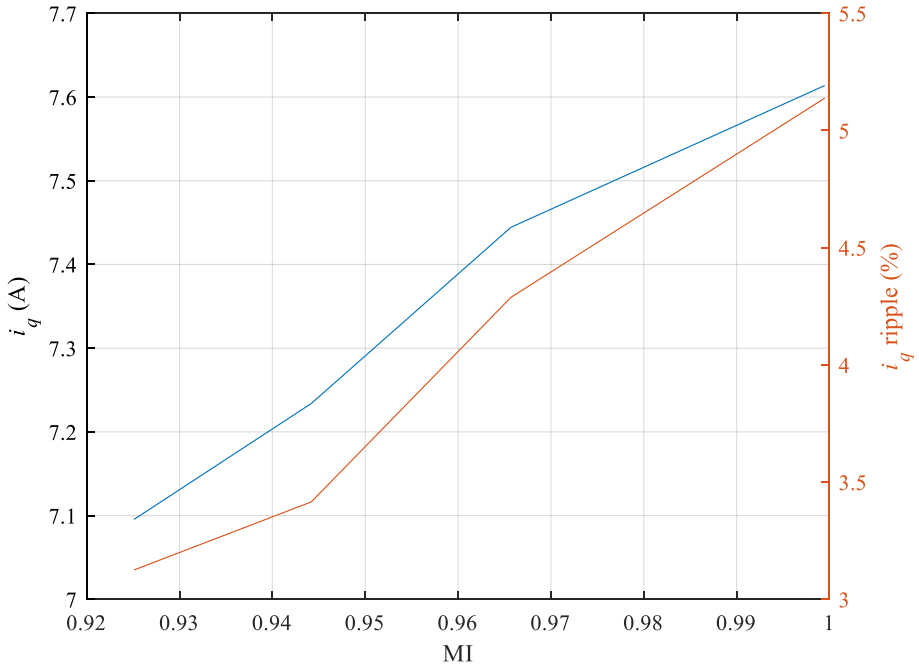

Fig. 5.9 i_q and i_q ripple at different MI

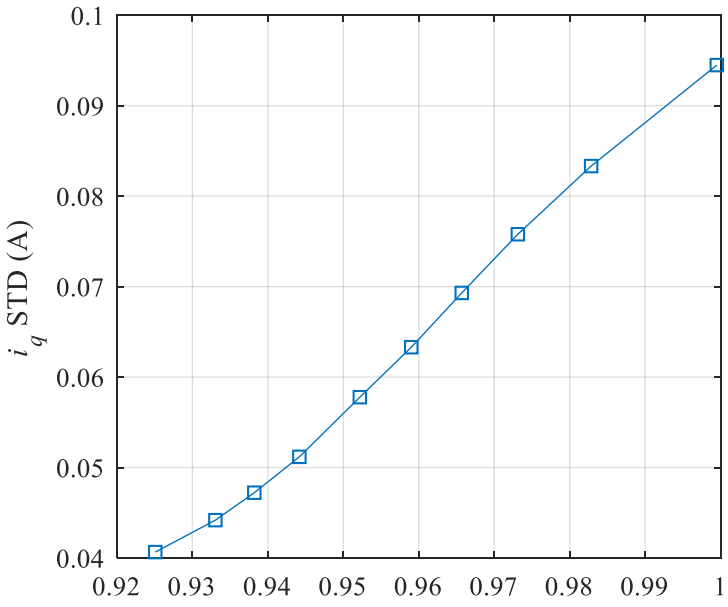

Fig. 5.10 i_q STD at different MI

5.3.2 Torque and Torque Ripple Analysis for the Proposed Flux-Weakening Method Considering Magnetic Saturation and Resistive Voltage Drop

The results of torque, torque ripple and STD, currents ripple and STD with the increase of MI at different speeds are shown in Table 5.1-Table 5.10 and Fig. 5.11- Fig. 5.19. The torque is increased with the increase of MI, which reaches the same conclusion as the mathematical analysis of the relationship between the voltage and torque in 5.2. At the same time, the torque ripple and STD, current ripple and STD are also increased with the increase of MI.

Table 5.1 Modulation index at different speed

MI	1	2	3	4
780 r/min	0.926	0.943	0.974	1
800 r/min	0.922	0.956	0.979	0.999
820 r/min	0.916	0.937	0.964	0.996

Table 5.2 Torque at different MI

Torque (Nm)	1	2	3	4
780 r/min	10.71	11.119	11.64	11.961
800 r/min	9.07	10.255	10.788	11.152
820 r/min	6.739	7.856	8.661	9.331

Table 5.3 Torque ripple at different MI

Torque ripple	1	2	3	4
780 r/min	4.324	4.675	6.971	8.774
800 r/min	6.553	13.637	18.23	20.876
820 r/min	5.857	7.917	11.534	14.145

Table 5.4 Torque STD at different MI

Torque STD (Nm)	1	2	3	4
780 r/min	0.081	0.122	0.222	0.3
800 r/min	0.106	0.283	0.403	0.477
820 r/min	0.058	0.115	0.205	0.298

Table 5.5 i_d at different MI

i_d (A)	1	2	3	4
780 r/min	-4.443	-4.275	-4.054	-3.902
800 r/min	-4.969	-4.7	-4.571	-4.479
820 r/min	-5.448	-5.244	-5.077	-4.917

Table 5.6 i_d ripple at different MI

i_d ripple	1	2	3	4
780 r/min	-7.428	-8.34	-8.709	-10.36
800 r/min	-6.398	-7.042	-7.778	-8.532
820 r/min	-5.911	-6.172	-6.471	-6.862

Table 5.7 i_d STD at different MI

i_d STD(A)	1	2	3	4
780 r/min	0.064	0.066	0.069	0.074
800 r/min	0.063	0.065	0.067	0.069
820 r/min	0.062	0.063	0.065	0.066

Table 5.8 i_q at different MI

i_q (A)	1	2	3	4
780 r/min	4.054	4.217	4.426	4.556
800 r/min	3.413	3.871	4.079	4.222
820 r/min	2.522	2.947	3.255	3.513

Table 5.9 i_q ripple at different MI

i_q ripple	1	2	3	4
780 r/min	4.585	4.926	7.046	8.896
800 r/min	6.765	13.789	18.415	21.138
820 r/min	5.997	7.924	11.587	14.217

Table 5.10 i_q STD at different MI

i_q STD(A)	1	2	3	4
780 r/min	0.032	0.047	0.085	0.115
800 r/min	0.04	0.108	0.154	0.183
820 r/min	0.022	0.044	0.077	0.113

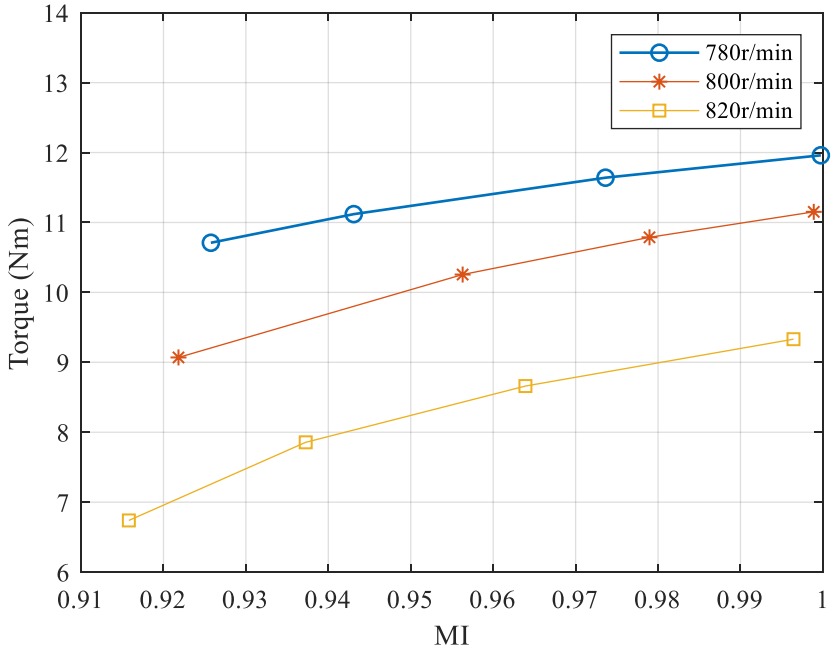

Fig. 5.11 Torque at different MI

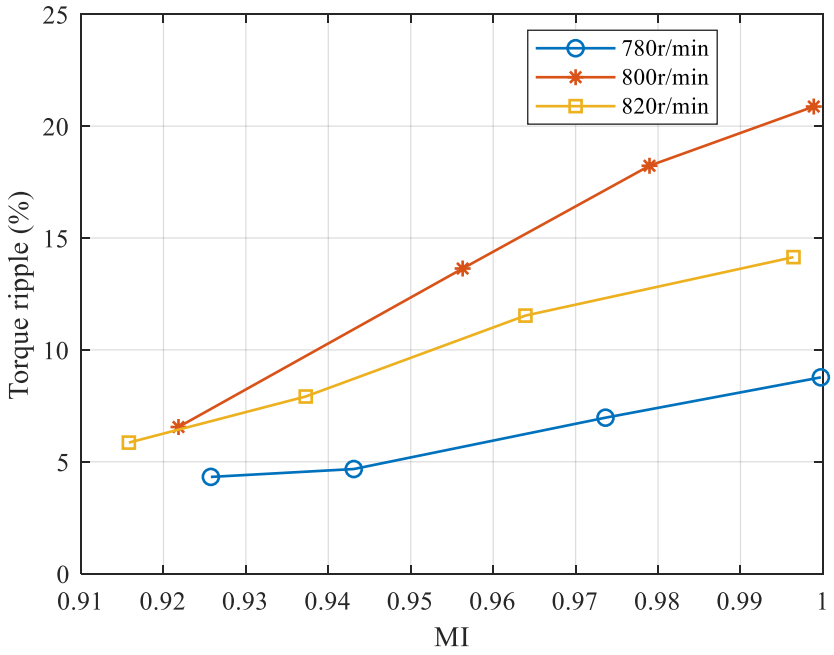

Fig. 5.12 Torque ripple at different MI

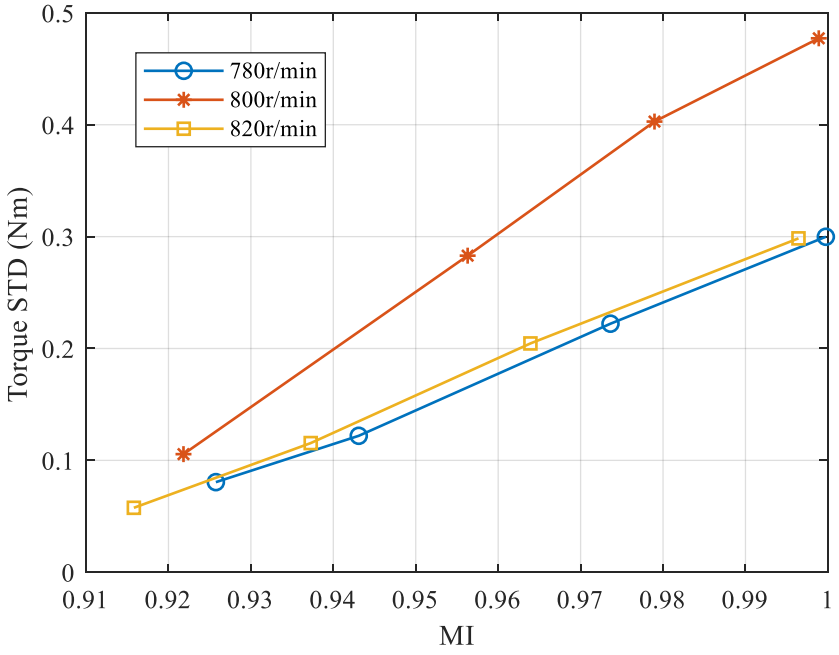

Fig. 5.13 Torque STD at different MI

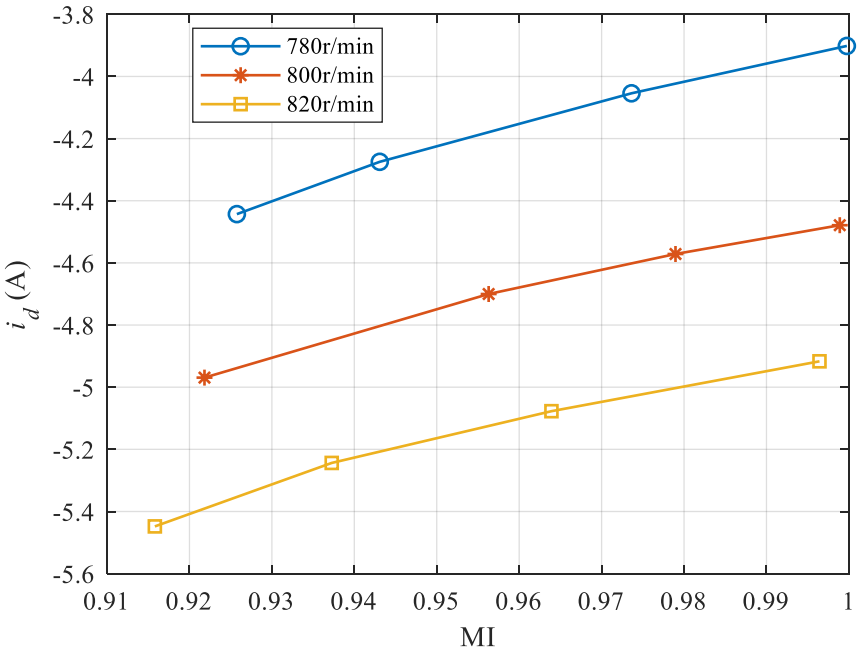

Fig. 5.14 i_d at different MI

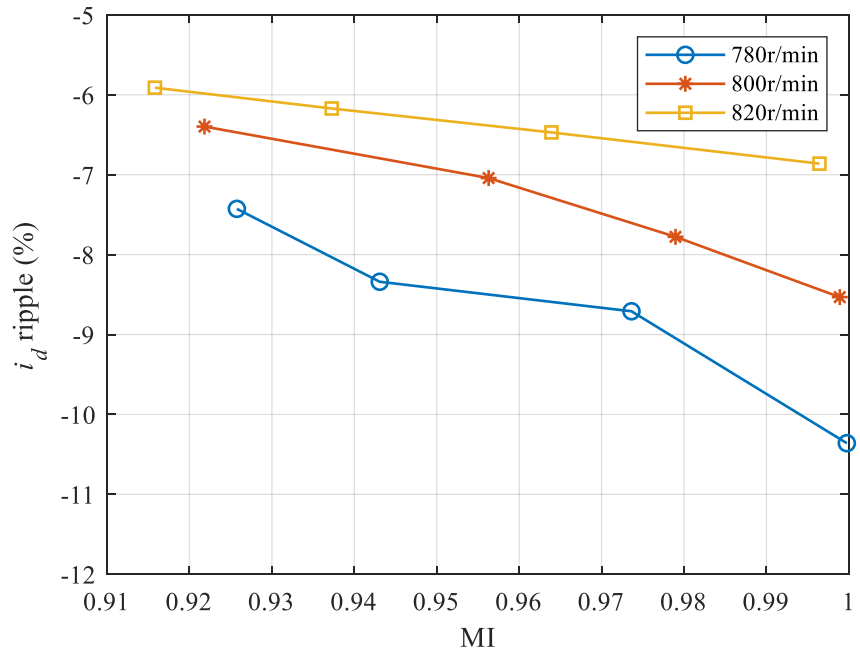

Fig. 5.15 i_d ripple at different MI

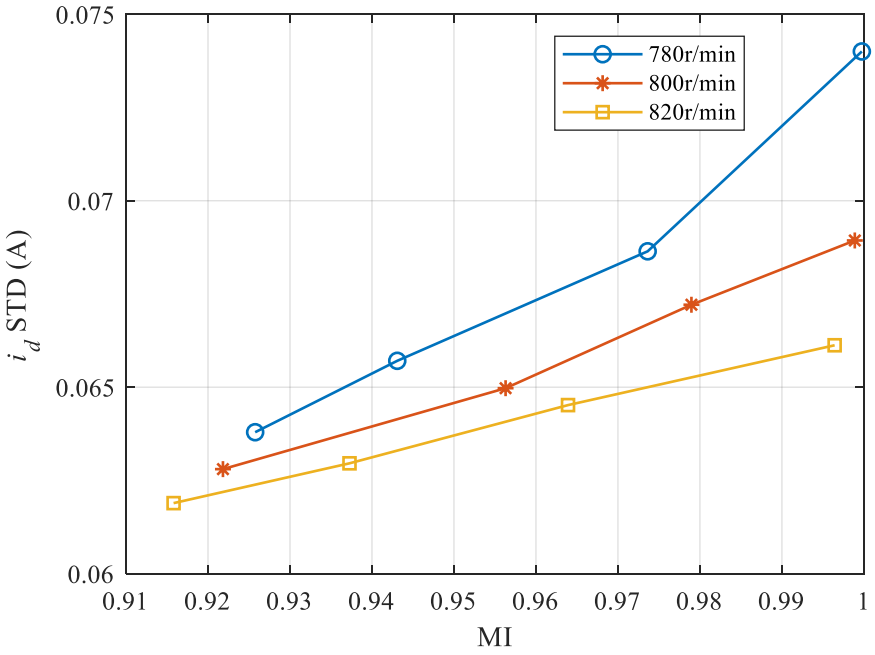

Fig. 5.16 i_d STD at different MI

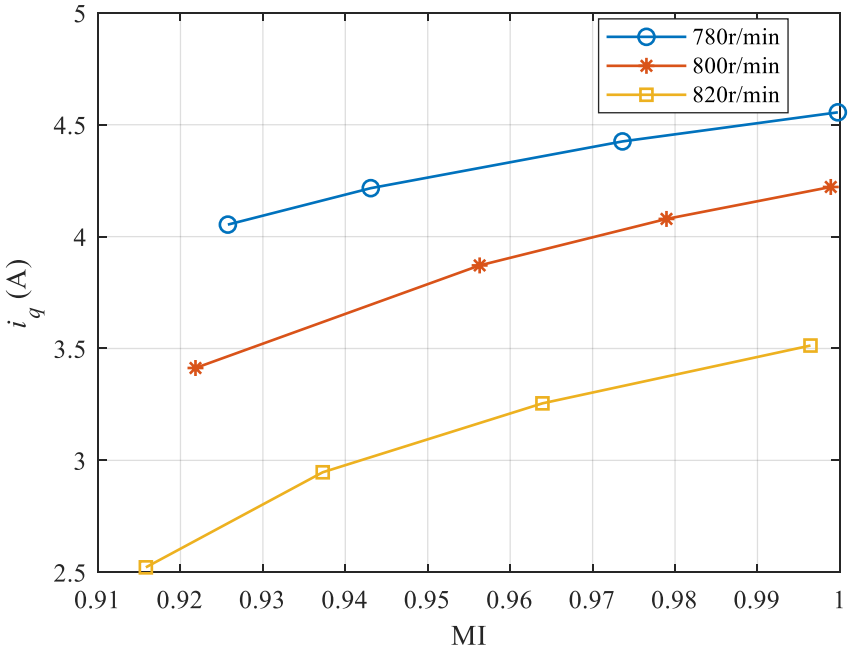

Fig. 5.17 i_q at different MI

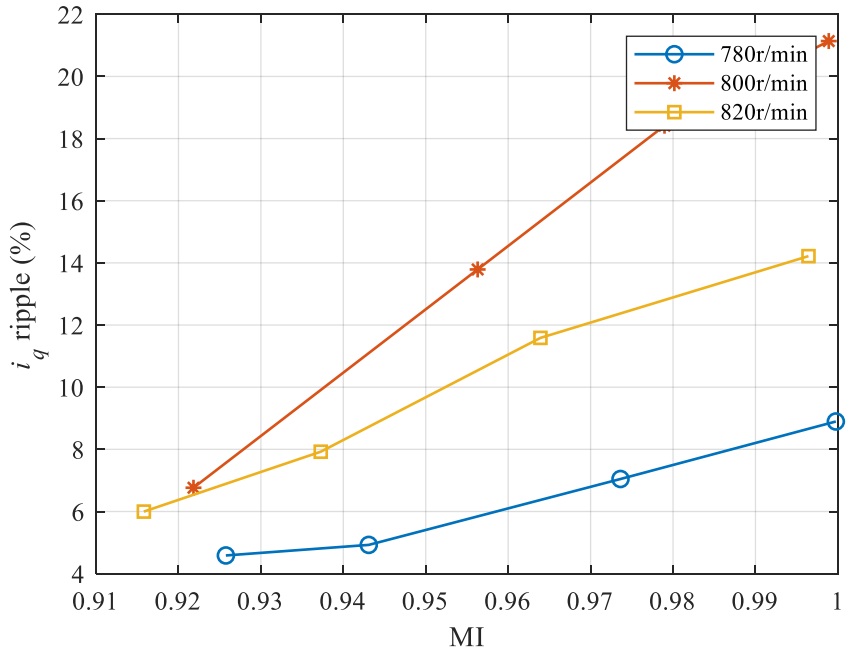

Fig. 5.18 i_q ripple at different MI

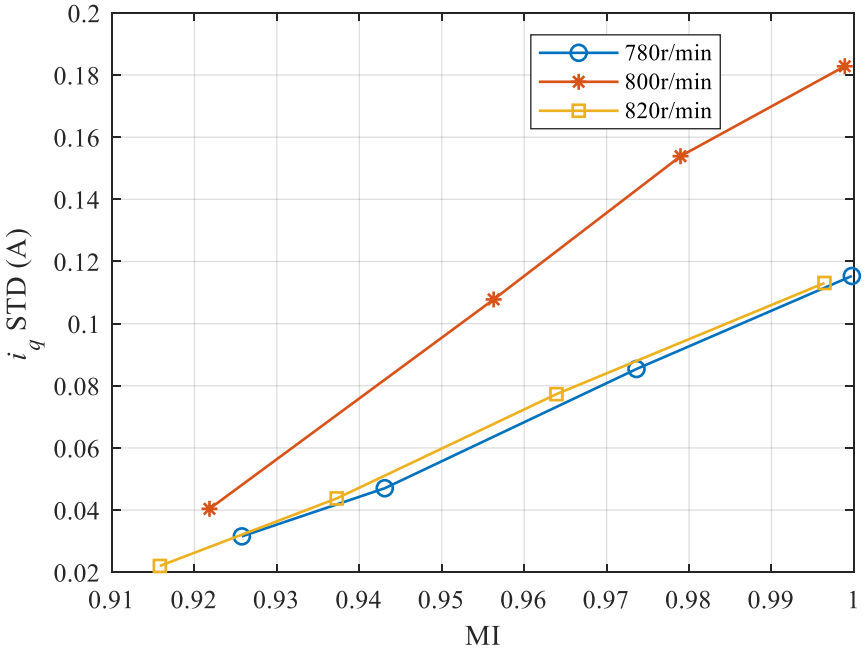

Fig. 5.19 i_q STD at different MI

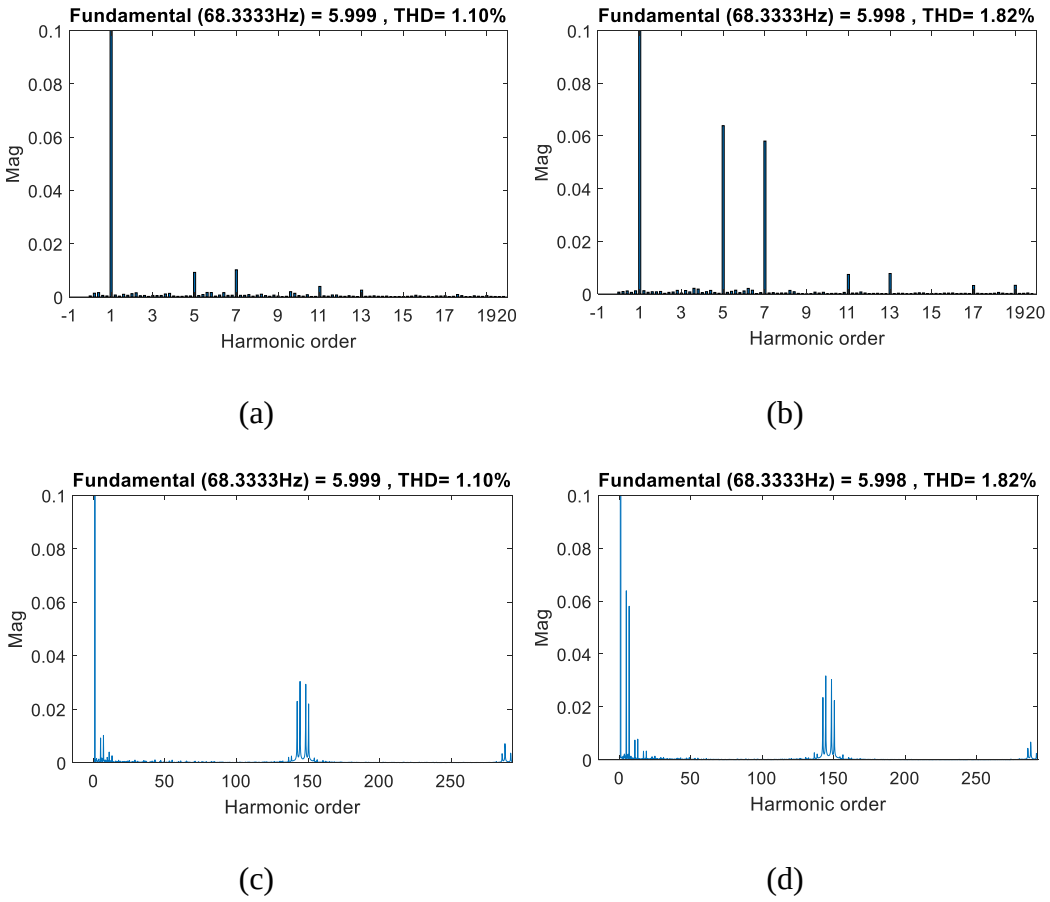

Fig. 5.20 Harmonic Spectra of the current with or without voltage extension. (a) Without extension. (b) With extension. (c) Without extension. (d) With extension.

As shown in Fig. 5.20, with voltage extension, the low order harmonics of current, especially 5th and 7th, are increased. The 146th harmonic is 10kHz, which is the switching frequency. The harmonics at f_{sw} and 2 x f_{sw} with and without voltage extension are similar.

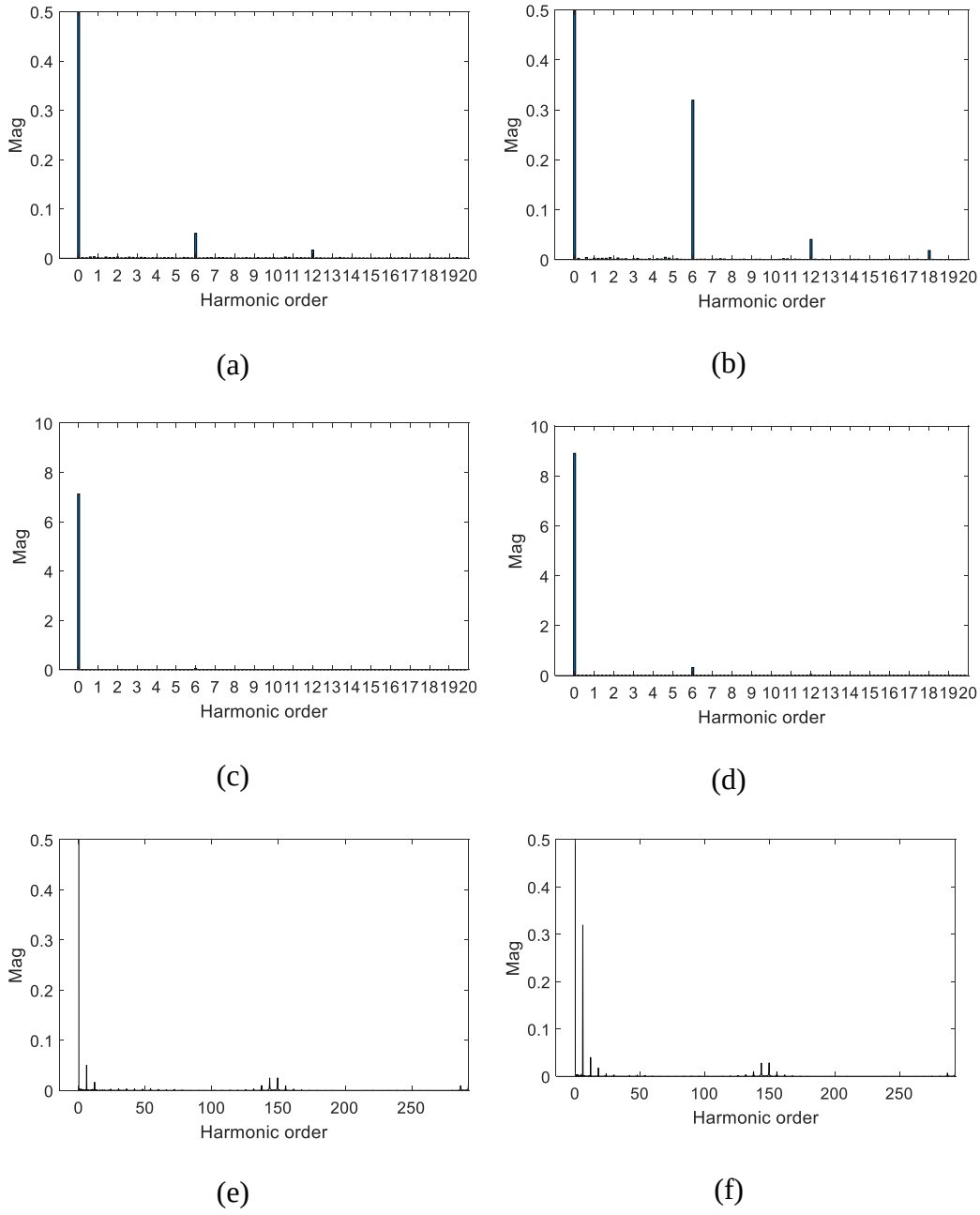

Fig. 5.21 Harmonic Spectra of the torque with or without voltage extension. (a) Without extension. (b) With extension. (c) Without extension. (d) With extension. (e) Without extension. (f) With extension.

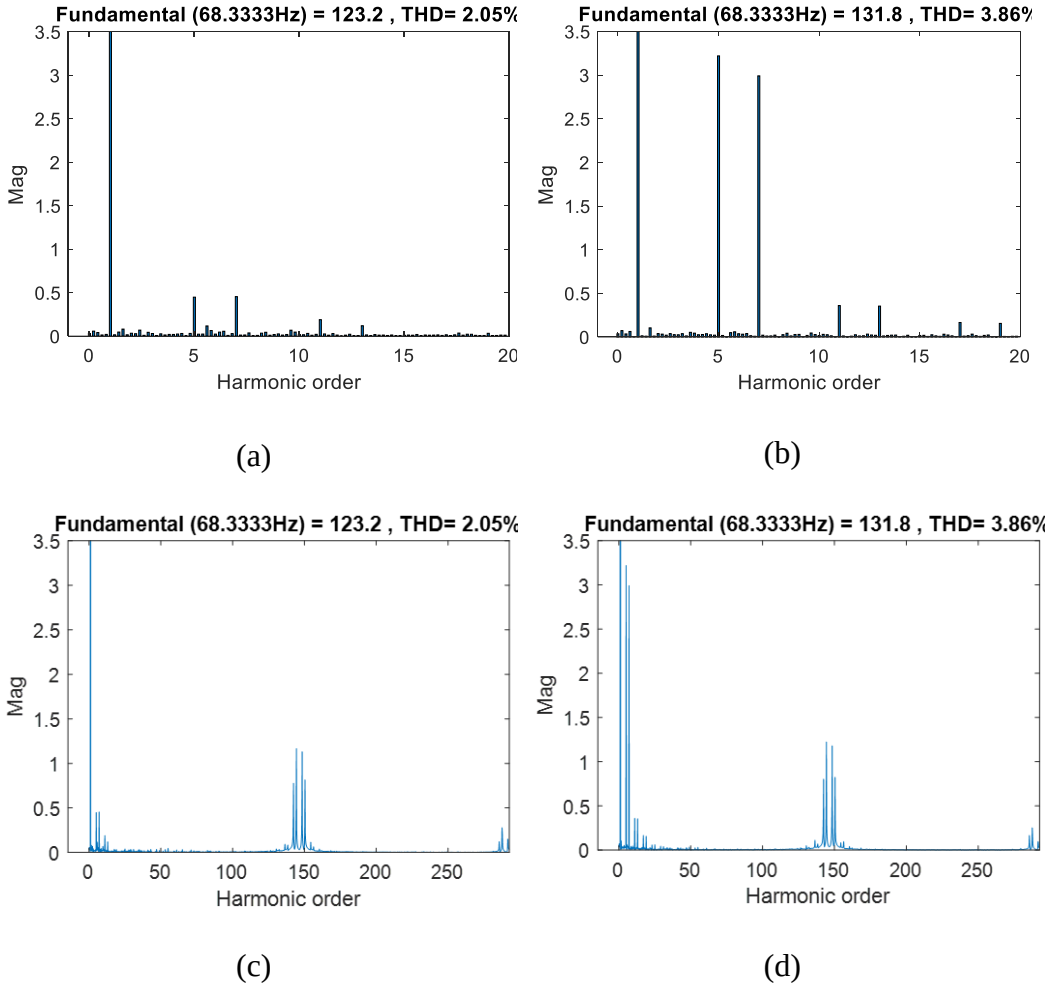

Fig. 5.22 Harmonic Spectra of the voltage with or without voltage extension. (a) Without extension. (b) With extension. (c) Without extension. (d) With extension.

As shown in Fig. 5.21, the torque amplitude of the dc component with voltage extension is increased. Low-order harmonics of torque are also increased, especially 6^{th} and 12^{th}. The harmonics of torque at f_{sw} and 2 x f_{sw} with and without voltage extension are similar.

As shown in Fig. 5.22, the fundamental component of voltage with voltage extension is increased. The low-order harmonics, especially 5^{th} and 7^{th} are also

increased. The 146th harmonic is 10kHz, which is the switching frequency. The harmonics at f_{sw} and 2 x f_{sw} with and without voltage extension are similar.

5.4 Conclusion

This chapter presents the windup phenomenon of the current regulation loops in voltage extension region and mathematical analysis of the relationship between voltage and torque. Then the torque, torque ripple, and current harmonics trends in voltage extension region are analyzed. The torque and power are increased with a higher voltage utilization rate. At the same time, the current STD and current ripple, torque STD and torque ripple are increased. Considering the tradeoff between maximizing the torque and torque ripple alleviation, finding a proper MI limit in the proposed flux-weakening methods to meet the requirement is accessible. The analysis of the voltage, torque, and torque ripple will act as the guidance to make the tradeoff between maximizing the torque and torque ripple alleviation. The advantages of extended dc-link voltage utilization are that the fundamental component of current regulator output voltages and dc component of torque are increased. A disadvantage of voltage extension is that low order harmonics of currents, voltage, and torque are increased. The windup phenomenon is also a problem in the voltage extension region, which makes the flux-weakening control complicated.

Chapter 6
Conclusions and Future Work

6.1 Conclusions

A flux-weakening control strategy for IPMSMs is proposed, which extends the dc-link voltage utilization and improves the tracking performance. With the proposed flux regulator and overmodulation technique, the voltage extension is achieved, and the torque and output power are increased. The tracking performance is improved by the current predictive controller.

A SFLA flux-weakening control method considering the resistive voltage drop and magnetic saturation is proposed. The stator flux linkage reference is adjusted based on the torque, speed, and modulation index. Two voltage feedback paths are provided in the proposed SFLA-FWC method. The feedback path is chosen based on the torque reference and operating speed. Compared to the FF-based flux-weakening methods, the proposed method can adjust the stator flux linkage reference, increase the voltage utilization rate, and improve the torque and power. The proposed method improves the dynamic performance and avoids the

windup problem in the transient process compared to the FB-based flux-weakening control methods. Compared to the mixed flux-weakening control methods, which only have one feedback path, the proposed method has a faster dynamic performance. The proposed method avoids the control error caused by parameter mismatch compared to the flux-weakening methods which ignore the resistive voltage drop.

The windup phenomenon of current regulation loops in voltage extension region, and the mathematical relationship between voltage and torque are analyzed. The MI is controlled in the proposed flux-weakening methods to avoid the windup problem. The torque, torque ripple, and current ripple and harmonics trends in voltage extension region are analyzed. The torque and power are increased with the increase in voltage utilization rate. The current ripple and torque ripple are also increased with the increase in voltage utilization rate.

The fundamental component of voltages and the dc component of torque are increased by extending the voltage utilization, which is the reason for improved torque and output power. The low order harmonics of voltage, current, and torque are also increased with the increase in voltage utilization rate, which induces larger torque ripple. The analysis of the relationship among voltage, current, torque, and torque ripple can help to make the tradeoff between maximizing the torque and torque ripple alleviation.

6.2 Future Work

Losses and efficiency in the voltage extension region can be further investigated. In chapter 5, the relationship between the voltage utilization rate and torque ripple has been analyzed, which will act as the guidance to make the tradeoff between maximizing the torque and torque ripple alleviation. The investigation of the relationship between motor losses and voltage utilization rate can act as the guidance to make the tradeoff between maximizing the torque and power, and not losing the efficiency. Motor losses which include iron loss, copper loss, and friction loss, can be obtained by FEA software, which requires the FEA model of the IPMSM. Motor losses can also be calculated by models and equations of losses.

In addition, the relationship between the voltage utilization rate and inverter loss can be investigated and act as the guidance to make the tradeoff. The inverter loss includes two parts: switching loss and conduction loss [57]. The inverter loss can be estimated based on current, voltage, MI, switching frequency, and power factor, or obtained by power analyzer, which is calculated as the difference between input power and inverter output power [58]. After the investigation of losses, the relationship between the efficiency of the IPMSM drive system and the dc-link voltage utilization rate can be used for efficiency optimization in the voltage extension region.

References

[1] A. Emadi, Y. J. Lee, and K. Rajashekara, “Power electronics and motor drives in electric, hybrid electric, and plug-in hybrid electric vehicles,” *IEEE Trans. Ind. Electron*., vol. 55, no. 6, pp. 2237–2245, Jun. 2008.

[2] D. Ronanki and S. S. Williamson, “Modular multilevel converters for transportation electrification: Challenges and opportunities,” *IEEE Trans. Transp. Electrif*., vol. 4, no. 2, pp. 399–407, Jun. 2018.

[3] S. Habib, M. M. Khan, F. Abbas, L. Sang, M. U. Shahid, and H. Tang, “A comprehensive study of implemented international standards, technical challenges, impacts and prospects for electric vehicles,” *IEEE Access*, vol. 6, pp. 13866–13890, Mar. 2018.

[4] J. Liang, J. W. Jiang, B. Bilgin, and A. Emadi, “Shaft design for electric traction motors,” *IEEE Trans. Transp. Electrif*., vol. 4, no. 3, pp. 720–731, Sep. 2018.

[5] K. L. V. Iyer, C. Lai, S. Mukundan, H. Dhulipati, K. Mukherjee, and N. C. Kar, “Investigation of interior permanent magnet motor with dampers for electric vehicle propulsion and mitigation of saliency effect during integrated charging operation,” *IEEE Trans. Veh. Technol*., vol. 68, no. 2, pp. 1254–1265, Feb. 2019.

[6] Y. Jiang, W. Xu, C. Mu and Y. Liu, "Improved deadbeat predictive current control combined sliding mode strategy for PMSM drive system," *IEEE Trans. Veh. Technol*., vol. 67, no. 1, pp. 251-263, Jan. 2018.

[7] B. Bilgin and A. Emadi, “Electric motors in electrified transportation: a step toward achieving a sustainable and highly efficient transportation system,” *IEEE Power Electron. Mag.*, vol. 1, no. 2, pp. 10-17, June. 2014.

[8] B. Bilgin, P. Magne, P. Malysz, Y. Yang, V. Pantelic, M. Preindl, A.Korobkine, W. Jiang, M. Lawford, and A. Emadi, "Making the case for electrified transportation," *IEEE Trans. Transp. Electrif.*, vol. 1, no. 1, pp. 4-17, June 2015.

[9] H. Liu, Z. Q. Zhu, E. Mohamed, Y. Fu, and X. Qi, “Flux-weakening control of nonsalient pole PMSM having large winding inductance, accounting for resistive voltage drop and inverter nonlinearities,” *IEEE Trans. Power Electron*., vol. 27, no. 2, pp. 942–952, Feb. 2012.

[10] D. Ding, G. Wang, N. Zhao, G. Zhang, and D. Xu, “Enhanced flux-weakening control method for reduced DC-link capacitance IPMSM drives,” *IEEE Trans. Power Electron*., vol. 34, no. 8, pp. 7788–7799, Aug. 2019.

[11] H. Ge, Y. Miao, B. Bilgin, B. Nahid-Mobarakeh, and A. Emadi, “Speed range extended maximum torque per ampere control for PM drives considering inverter and motor nonlinearities,” *IEEE Trans. Power Electron*., vol. 32, no. 9, pp. 1751–1759, Sep. 2017.

[12] Z. Q. Zhu, Y. S. Chen, and D. Howe, “Online optimal flux-weakening control of permanent-magnet brushless AC drives,” *IEEE Trans. Ind. Appl*., vol. 36, no. 6, pp. 1661–1668, Nov./Dec. 2000.

[13] H. W. Kock, A. J. Rix, and M. J. Kamper, "Optimal torque control of synchronous machines based on finite-element analysis," *IEEE Trans. Ind. Electron.*, vol. 57, no. 1, pp. 413–419, Jan. 2010.

[14] B. Cheng and T. R. Tesch, "Torque feedforward control technique for permanent-magnet synchronous motors," *IEEE Trans. Ind. Electron.*, vol. 57, no. 3, pp. 969–974, Mar. 2010.

[15] Y. Chen et al., "Improved flux-weakening control of IPMSMs based on torque feedforward technique," *IEEE Trans. Power Electron.*, vol. 33, no. 12, pp. 10970–10978, Dec. 2018.

[16] T. S. Kwon, G. Y. Choi, M. S. Kwak, and S. K. Sul, "Novel flux- weakening control of an IPMSM for quasi six-step operation," *IEEE Trans. Ind. Appl.*, vol. 44, no. 6, pp. 1722–1731, Nov./Dec. 2008.

[17] K. D. Hoang and H. K. A. Aorith, "Online control of IPMSM drives for traction applications considering machine parameter and inverter nonlinearities," *IEEE Trans. Transp. Electrif.*, vol. 1, no. 4, pp. 312–325, Dec. 2015.

[18] D. C. Lee and G. M. Lee, "A novel overmodulation technique for space-vector PWM inverters," *IEEE Trans. Power Electron.*, vol. 13, no. 6, pp. 1144–1151, Nov. 1998.

[19] S. Bolognani and M. Zigliotto, "Novel digital continuous control of SVM inverters in the overmodulation range," *IEEE Trans. Ind. Appl.*, vol. 33, no. 2, pp. 525–530, Mar./Apr. 1997.

[20] D. Hu, Y. M. Alsmadi, and L. Xu, "High-fidelity nonlinear IPM modeling based on measured stator winding flux linkage," *IEEE Trans. Ind. Appl*., vol. 51, no. 4, pp. 3012–3019, July. 2015.

[21] L. Chang and T. Jahns, "Prediction and evaluation of PWM-induced current ripple in IPM machines incorporating slotting, saturation, and cross-coupling effects," *IEEE Trans. Ind. Appl*., vol. 54, no. 6, pp. 6015–6026, Dec. 2018.

[22] E. Dlala and A. Arkkio, "A general model for investigating the effects of the frequency converter on the magnetic iron losses of a squirrel-cage induction motor," *IEEE Tran. Magnetics*, vol. 45, no. 9, pp. 3303–3315, Sept. 2009.

[23] W. C. Lo, C. C. Chan, Z. Q. Zhu, L. Xu, and D. Howe, "Acoustic noise radiated by PWM-controlled induction machine drives," *IEEE Trans. Ind. Electron*, vol. 47, no. 4, pp. 880–889, Aug. 2000.

[24] I. P. Tsoumas and H. Tischmacher, "Influence of the inverter's modulation technique on the audible noise of electric motors," *IEEE Trans. Ind. Appl*., vol. 50, no. 1, pp. 269–278, Jan./Feb. 2014.

[25] P. Zhou, W. N. Fu, D. Lin, S. Stanton, and Z. J. Cendes, "Numerical modeling of magnetic devices," *IEEE Trans. Ind. Appl*., vol. 40, no. 4, pp. 1803–1809, Jul./Aug. 2004.

[26] J. F. Bangura, "Directly coupled electromagnetic field-electric circuit model for analysis of a vector-controlled wound field brushless starter generator," *IEEE Trans. Energy Convers*., vol. 26, no. 4, pp. 1033–1040, Dec. 2011.

[27] W. Liang, J. Wang, T. Lu, and W. Fang, "A new method for multiple finite-element models in cosimulation with electrical circuit using machine multiloop modeling scheme," *IEEE Trans. Ind. Electron*, vol. 61, no. 12, pp. 6583–6590, Dec. 2014.

[28] J. Dong, B. Howey, B. Danen, J. Lin, J. W. Jiang, B. Bilgin, and A. Emadi, "Advanced dynamic modeling of three-phase mutually-coupled switched reluctance machine," *IEEE Trans. Energy Convers*., vol. 33, no. 1, pp. 146–154, Mar. 2018.

[29] X. Chen, J. Wang, B. Sen, P. Lazari, and T. Sun, "A high-fidelity and computationally efficient model for interior permanent-magnet machines considering the magnetic saturation, spatial harmonics, and iron loss effect," *IEEE Trans. Ind. Electron*, vol. 62, no. 7, pp. 4044–4055, Jul. 2015.

[30] S. Li, D. Han, and B. Sarlioglu, "Modeling of interior permanent magnet machine considering saturation, cross coupling, spatial harmonics, and temperature effects," *IEEE Trans. Transp. Electrif.*, vol. 3, no. 3, pp. 682–693, Sept. 2017.

[31] G. Luo, R. Zhang, Z. Chen, W. Tu, S. Zhang, and R. Kennel, "A novel nonlinear modelling method for permanent magnet synchronous motors," *IEEE Trans. Ind. Electron*, vol. PP, no. 99, pp. 1–1, Oct. 2016.

[32] T. M. Jahns, "Flux-weakening regime operation of an interior permanent-magnet synchronous motor drive," *IEEE Trans. Ind. Appl*., vol. IA-23, no. 4, pp. 681–689, 1987.

[33] J. M. Kim and S. K. Sul, "Speed control of interior permanent magnet synchronous motor drive for the flux weakening operation," *IEEE Trans. Ind. Appl*., vol. 33, no. 1, pp. 43–48, 1997.

[34] P. Y. Lin and Y. S. Lai, "Voltage control technique for the extension of DC-link voltage utilization of finite-speed SPMSM drives," *IEEE Trans. Ind. Electron*., vol. 59, no. 9, pp. 3392–3402, Dec. 2012.

[35] Y. C. Kwon, S. Kim, and S. K. Sul, "Voltage feedback current control scheme for improved transient performance of permanent magnet synchronous machine drives," *IEEE Trans. Ind. Electron*., vol. 59, no. 9, pp. 3373–3382, Sep. 2012.

[36] X. Li, C. Liu, S. Wu, S. Chi, and P. C. Loh, "Sliding-Mode flux-weakening control with only single current regulator for permanent magnet synchronous motor," *IEEE Access*, vol. 7, pp. 131616–131626, Sep. 2019.

[37] Y. Zhang, L. Xu, M. K. Güven, S. Chi, and M. Illindala, "Experimental verification of deep field weakening operation of a 50-kW IPM machine by using single current regulator," *IEEE Trans. Ind. Appl*., vol. 47, no. 1, pp. 128–133, Jan./Feb. 2011.

[38] Z. Zhang, C. Wang, M. Zhou, and X. You, "Flux-Weakening in PMSM drives: analysis of voltage angle control and the single current controller design," *IEEE J. Emerg. Sel. Top. Power Electron*., vol. 7, no. 1, pp. 437–445, Mar. 2019.

[39] S. Bolognani, S. Calligaro, and R. Petrella, "Adaptive flux-weakening controller for interior permanent magnet synchronous motor drives," *IEEE J. Emerg. Sel. Top. Power Electron*., vol. 2, no. 2, pp. 236–248, Jun. 2014

[40] N. Bedetti, S. Calligaro, and R. Petrella, "Analytical design and autotuning of adaptive flux-weakening voltage regulation loop in IPMSM drives with accurate torque regulation," *IEEE Trans. Ind. Appl*., vol. 56, no. 1, pp. 301–313, Jan./Feb. 2020.

[41] C. Wang and Z. Q. Zhu, "Fuzzy logic speed control of permanent magnet synchronous machine and feedback voltage ripple reduction in flux-weakening operation region," *IEEE Trans. Ind. Appl*., vol. 56, no. 2, pp. 1505-1517, Mar./Apr. 2020.

[42] M. N. Uddin, T. S. Radwan, and M. A. Rahman, "Performance of interior permanent magnet motor drive over wide speed range," *IEEE Trans. Energy Convers*., vol. 17, no. 1, pp. 79–84, Mar. 2002.

[43] M. N. Uddin and M. M. I. Chy, "Online parameter-estimation-based speed control of PM AC motor drive in flux-weakening region," *IEEE Trans. Ind. Appl*., vol. 44, no. 5, pp. 1486–1494, Sep./ Oct. 2008.

[44] S. Wang, J. Kang, M. Degano, A. Galassini, and C. Gerada, "An accurate wide-speed range control method of IPMSM considering resistive voltage drop and magnetic saturation," *IEEE Trans. Ind. Electron*., vol. 67, no. 4, pp. 2630–2641, Apr. 2020.

[45] Z. Xia, S. Nalakath, R. Tarvirdilu-Asl, Y. Sun, J. Wiseman and A. Emadi, " Online optimal tracking method for interior permanent magnet machines with improved MTPA and MTPV in whole speed and torque ranges," *IEEE Trans. Power Electron*, vol. 35, no. 9, pp. 9755-9771, Sept. 2020

[46] J. Liu, W. Zhang, F. Xiao, C. Lian, and S. Gao, “Six-step mode control of ipmsm for railway vehicle traction eliminating the dc offset in input current,” *IEEE Trans. Power Electron*., vol. 34, no. 9, pp. 8981–8993, Sep. 2019.

[47] M. Tursini, E. Chiricozzi, and R. Petrella, “Feedforward flux-weakening control of surface-mounted permanent-magnet synchronous motors accounting for resistive voltage drop,” *IEEE Trans. Ind. Electron*., vol. 57, no. 1, pp. 440–448, Jan. 2010.

[48] H. Ge, B. Bilgin, and A. Emadi, "Global loss minimization control of PMSM considering cross-coupling and saturation," *in Proc. IEEE Energy Convers. Congr. and Expo., Montreal*, QC, 2015, pp. 6139-6144.

[49] I. Ralev, T. Lange, and R. W. De Doncker, “Wide speed range six-step mode operation of IPMSM drives with adjustable dc-link voltage,” *2014 17th Int. Conf. Electr. Mach. Syst*., Hangzhou, pp. 2987–2993, 2014.

[50] J. Holtz, W. Lotzkat, and A. M. Khambadkone, “On continuous control of PWM inverters in the overmodulation range including the six-step mode,” *IEEE Trans. Power Electron*., vol. 8, no. 4, pp. 546–553, Oct. 1993.

[51] Y. Miao, H. Ge, M. Preindl, J. Ye, B. Cheng, and A. Emadi, “MTPA fitting and torque estimation technique based on a new flux-linkage model for interior-

permanent-magnet synchronous machines," *IEEE Trans. Ind. Appl.*, vol. 53, no. 6, pp. 5451–5460, Nov./Dec. 2017.

[52] M. Preindl and S. Bolognani, "Model predictive direct torque control with finite control set for PMSM drive systems, part 1: maximum torque per ampere operation," *IEEE Trans. Ind. Informatics*, vol. 9, no. 4, pp. 1912–1921, Nov. 2013.

[53] Y. Li, B. Howey, J. Liang, E. Sayed, A. Qazalbash, M. Kasprzak, D. Al-Ani, A. Emadi, and B. Bilgin, "Dynamic Modeling of an Interior Permanent Magnet Machine with Space-Vector-Modulation-Based Voltage Source Inverter," *SAE Technical Paper* 2020-01-0469, 2020, doi:10.4271/2020-01-0469.

[54] Y. Li, Z. Xia, J. Liang, and A, Emadi, "Flux-Weakening Control of Interior Permanent Magnet Synchronous Motors with Extended DC-Link Voltage Utilization and Improved Tracking Performance," *in Proc. IEEE Transp. Electrif. Conf. Expo*, Michigan, MI, USA, Jun. 2020.

[55] H. Chaoui, O. Okoye, and M. Khayamy, "Current Sensorless MTPA for IPMSM Drives," *IEEE/ASME Trans. Mechatronics*, vol. 22, no. 4, pp. 1585–1593, 2017.

[56] M. Khayamy and H. Chaoui, "Current Sensorless MTPA Operation of Interior PMSM Drives for Vehicular Applications," *IEEE Trans. Veh. Technol.*, vol. 67, no. 8, pp. 6872–6881, 2018.

[57] A. D. Rajapakse, A. M. Gole, and P. L. Wilson, "Electromagnetic transients simulation models for accurate representation of switching losses and thermal performance in power electronic systems," *IEEE Trans. Power Deliv.*, vol. 20, no. 1, pp. 319–327, Jan. 2005.

[58] Y. Miao, "High-accuracy torque control and estimation for interior permanent magnet synchronous machine drives with loss minimization," Ph.D. dissertation, Dept. Elect. Eng., McMaster Univ., Hamilton, ON, Canada, 2018.